LA-5487-T

THESIS

Development of the OSO-6 High-Energy Neutron Detector and Correlation of Measured Solar Neutron Fluxes to Solar Flares

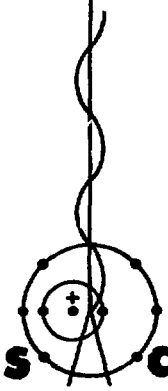

los alamos
scientific laboratory
of the University of California
LOS ALAMOS, NEW MEXICO 87544

UNITED STATES
ATOMIC ENERGY COMMISSION
CONTRACT W-7405-ENG. 36

This report is a printed version of a thesis submitted in partial fulfillment of the requirement for an advanced academic degree and as such represents the independent work of the author. It has not been edited by the Technical Information staff.

Printed in the United States of America. Available from
National Technical Information Service
U. S. Department of Commerce
5285 Port Royal Road
Springfield, Virginia 22151
Price: Printed Copy $7.60; Microfiche $1.45

LA-5487-T
Thesis
UC-34b
ISSUED: February 1974

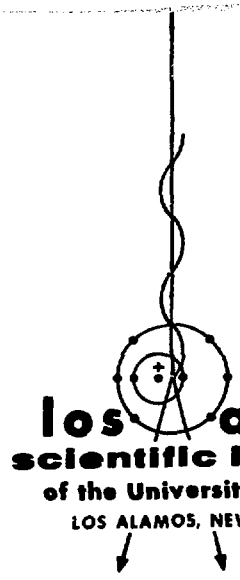

Development of the OSO-6 High-Energy Neutron Detector and Correlation of Measured Solar Neutron Fluxes to Solar Flares

by

Frederick Young

This report is derived from a dissertation submitted to the Department of Physics of The University of New Mexico in partial fulfillment of requirements for the Degree of Doctor of Philosophy.

CONTENTS

TABLES

FIGURES

FIGURES (cont)

FIGURES (cont)

ABSTRACT

Development of a directional high energy (20-160 MeV) neutron detector which was flown to satellite altitudes (500 km; circular equatorial orbit) in the NASA Orbiting Solar Observatory (OSO-6) in August 1969 is described.

Both the angle of incidence and the energy of the neutron are determined by a proton-recoil telescope (Pilot B scintillation plastic) which provides the source for proton-recoils and defines the dE/dX versus E method for particle identification and energy determination. The telescope is embedded in a scintillation plastic guard counter envelope which eliminates the unwanted charged particle background as well as recoil protons (electrons) whose energies and direction do not satisfy neutron (gamma-ray) detection requirements, respectively.

Results from a Monte Carlo calculation indicate that the overall average efficiency within an average angular acceptance of about 29^{o} (FWHM) is approximately $(2.25 \pm 0.113) \times 10^{-4}$. The in-flight calibration procedure, the main frame data bit error analysis, and the method for determining the orientation of the detector axis in the spacecraft spin plane is described.

Results indicate a discrepancy in the measured ($0.461 \times 10^{-2} \pm 0.254 \times 10^{-2}$ n/cm^{2}sec) and theoretical (2-70 n/cm^{2}sec) neutron fluxes which suggests a lack of basic understanding of mechanisms leading to high energy neutron production at the sun.

I. INTRODUCTION

A. Statement of the Problem

The discovery of the neutron is one of the most dramatic chapters in the history of modern physics. It started in Germany, in the last month of 1931, with the report by Bothe and Becker [1930] of a penetrating radiation resulting from the bombardment of certain light elements by polonium alpha-particles. They bombarded many substances, using a Geiger point-counter as a detector of the resulting radiation. Most of the elements investigated (Pb, Ag, Ca, N, C, O, Ne) yielded no detectable radiation; two (Mg, Al) showed a slight effect. Lithium, boron, and fluorine gave appreciable amounts of radiation capable of affecting the counter, and beryllium yielded a comparatively tremendous amount. Bothe and Becker concluded that the radiation consisted of gamma-rays, more penetrating than any that had been observed up to that time. Further study by I. Curie and F. Joliot [1932] gave the surprising result that this gamma radiation also had a component that was capable of impacting energies of several MeV to protons in a cloud chamber. At first Curie and Joliot interpreted the observed energy transfer as a Compton effect on protons. The correct explanation, however, was soon provided by Chadwick [1932, 1933], who showed that the recoil protons observed by Curie and Joliot had been hit by a neutral particle of approximately protonic mass, which he called the neutron. Chadwick was awarded the Nobel prize in 1935 for his discovery of the neutron. Chadwick bombarded with neutrons not only hydrogen but other light nuclei as well, and measured the range of the

recoil particles. From the conservation of energy and momentum and range-energy relations he was able to determine the mass of the new particle as very nearly the same as the mass of the proton.

The question on the detection of solar and terrestrial neutrons has been discussed fairly widely in the literature, Ro [1971]. Properly conducted measurements on the direction and energy of solar and terrestrial neutrons might provide some physical insight into terrestrial phenomena such as radiation belts and isotope production, into high energy processes that occur in the solar atmosphere, and into certain processes that occur in the interplanetary medium between the sun and the earth. Also, further information might be gained from a study of the correlation of the neutron measurement to solar activity. Since the lifetime of the neutron is only about 17 minutes, neutrons produced outside the solar system are probably not observed at the earth.

The University of New Mexico neutron experiment basically employs a recoil telescope configuration which uses pulse heights in all its counters for particle identification and energy determination. Here a thin counter (4 mm thickness) in which the ionization losses are $(dE/dx)x \ll E$, where x is the scintillator thickness in gm/cm^2, and a thick energy counter (10 cm thickness) in which the proton recoils are absorbed are used. Earlier studies, Sydor [1964] and Wolcott [1968], which were conducted at the University of New Mexico Physics Department have used this proton-recoil telescope technique. A more recent work, Ro [1971], has analyzed some of the OSO-6 solar neutron data (Aug. 1969 - Dec. 1969) with results that no significant solar neutron fluxes were observed during this period. In addition to the dE/dx and E

counters, two other scintillation counters are used to convert the neutron into a proton recoil. The set of four scintillation counters are embedded in a scintillation plastic guard counter envelope which eliminates the unwanted charged particle background as well as recoil protons or pair production electrons whose energies and directions do not satisfy neutral particle detection requirements.

Although most of the earlier measurements on earth albedo and solar neutrons have used omni-directional detectors, the present work makes use of a directional instrument. Although the efficiency is low for this type of instrument it was felt that a successful measurement of the neutron flux over a period of 6-12 months at satellite altitudes should provide sufficient data to give sufficient statistical accuracy. This instrument has operated successfully for a period of 28 months.

This experiment was flown primarily to determine the high energy spectrum and angular distribution of neutrons produced in the earth's atmosphere, and to measure the high energy spectrum of solar neutrons. These measurements would hopefully answer some of the basic questions on the physics of high energy processes that occur in the terrestrial and solar atmospheres and in the interplanetary medium. Some rel. ted areas of physical interest include the population of protons in the inner zone Van Allen radiation belt, Farley and Tomassian [1970], and the Southern Hemisphere anomalies, Smith-Rose [1966]. This work will attempt to analyze some solar neutron data as a function of solar flare activity.

B. The OSO-6 Spacecraft

The Orbiting Solar Observatory (OSO-6) spacecraft is shown in Figure 1 in its flight configuration. The spacecraft (Figure 2) has been described in detail in a NASA Experimenter's Manual, NASA [1966]. It was built by Ball Brothers Research Corporation of Boulder, Colorado, for the National Aeronautics and Space Administration (NASA). The spacecraft carried five experiments in the wheel and two experiments in the sail. The location of the University of New Mexico experiment is indicated in Figure 3. Referring to Figure 3 one can see that perhaps some neutrons with the proper energy and direction can be produced which would be incident on the neutron instrument as a result of cosmic ray protons or other charged particles bombarding the extended arm and its vessel. The vessels at the ends of each arm contain a gas supply for adjusting the rotation rate of the wheel. Furthermore, the extended arms serve to help with the stability of the spacecraft since the arms contribute to the total moment of inertia of the spacecraft.

The OSO-6 satellite was launched on August 9, 1969, from Cape Kennedy, Florida, at 3:00 a.m., into a near-circular orbit. A brief summary of the orbital conditions is presented in Table 1. The geocentric distances of perigee and apogee are about 1.076 and 1.085 earth radii. The orbital period is about 90 minutes while the spin period is about 2 seconds. Figure 4 illustrates some of the possible satellite orbits.

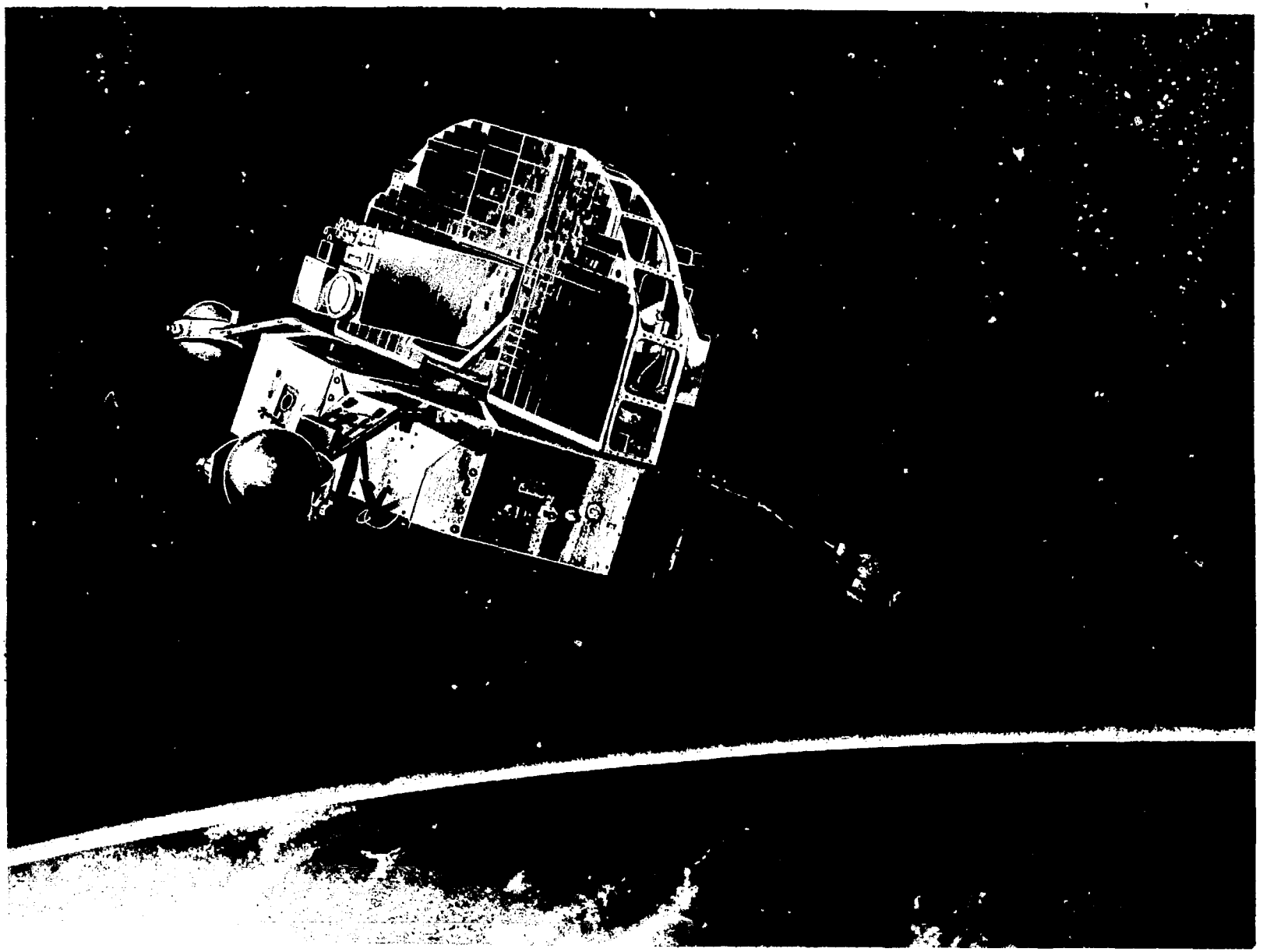

Fig. 1. The Orbiting Solar Observatory (OSO-6) Spacecraft in its Flight Configuration.

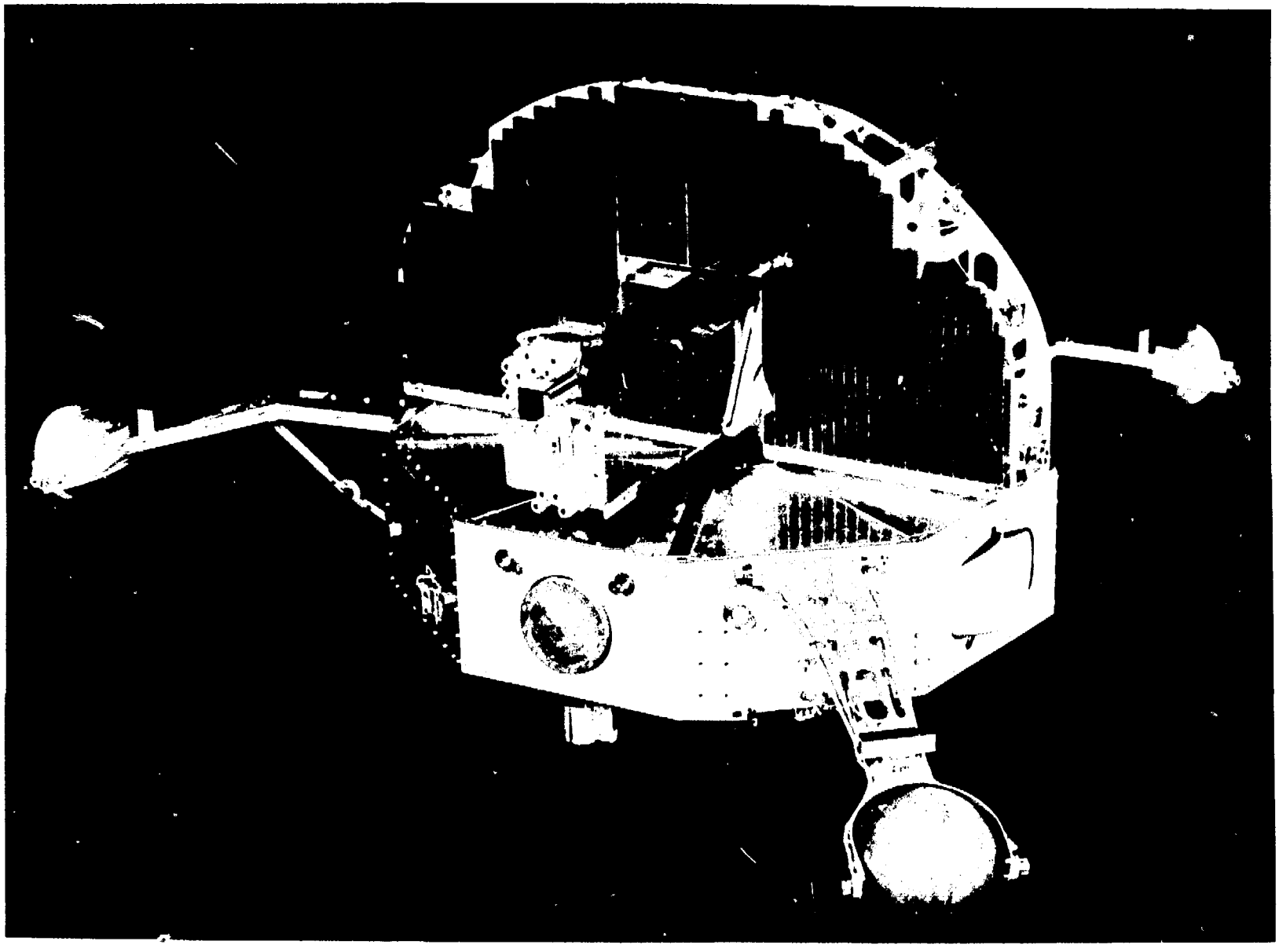

Fig. 2. The Orbiting Solar Observatory (OSO-6) Spacecraft with UNM Wheel Experiment Shown at Extreme Right.

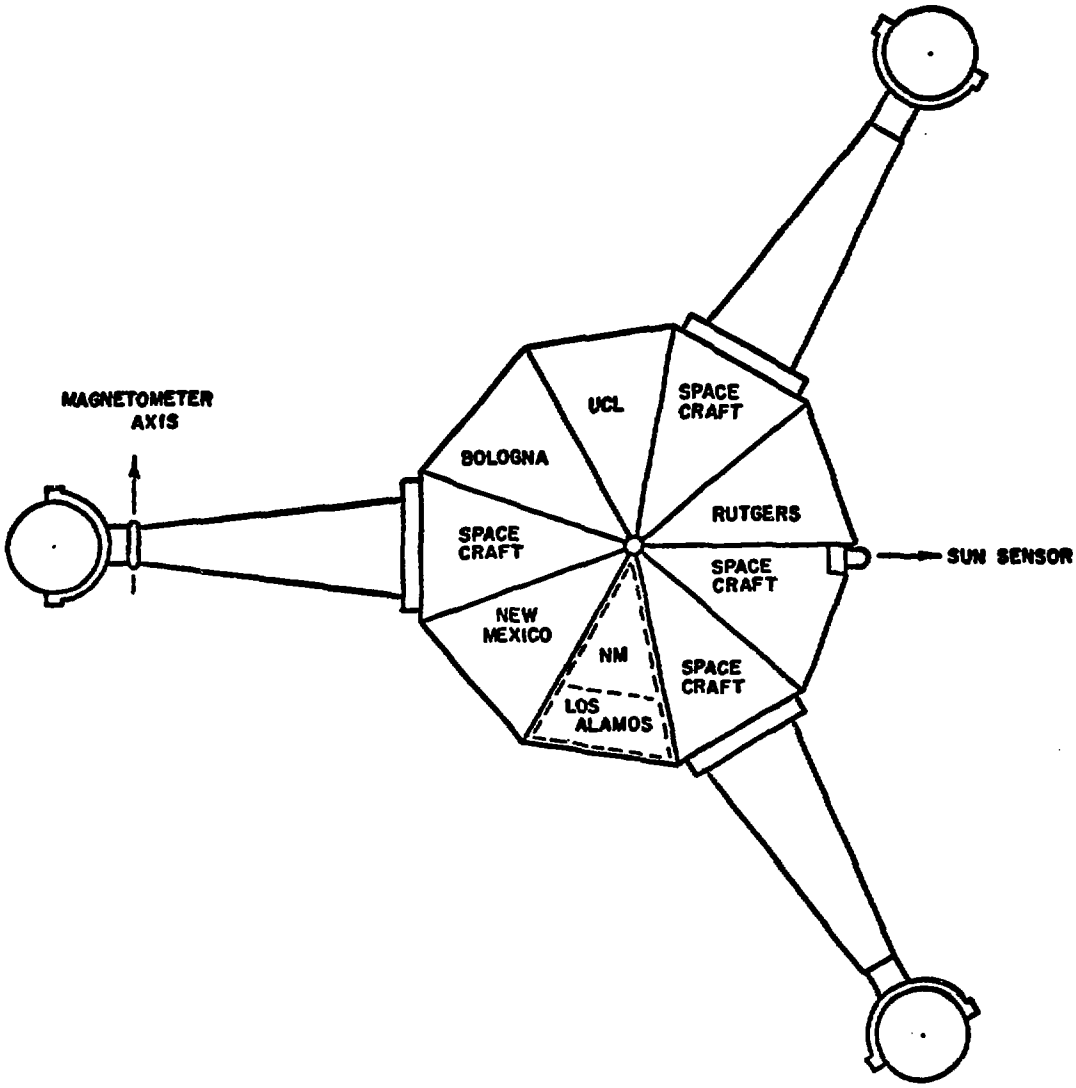

Fig. 3. Location of University of New Mexico High Energy Neutron Experiment in Wheel of Spacecraft.

Figure 4

NASA Space Tracking and Data Acquisition Network (Stadan).

Some Possible Satellite Orbits are Shown.

- Minitrack Tracking System.
- 85 ft. Parabolic Antenna System.
- 40 ft. Parabolic Antenna System.
- Mobile Telemetry & Command System.
- RR Range and Range RATF System.
- 136 MC Telemetry & Command Systems.

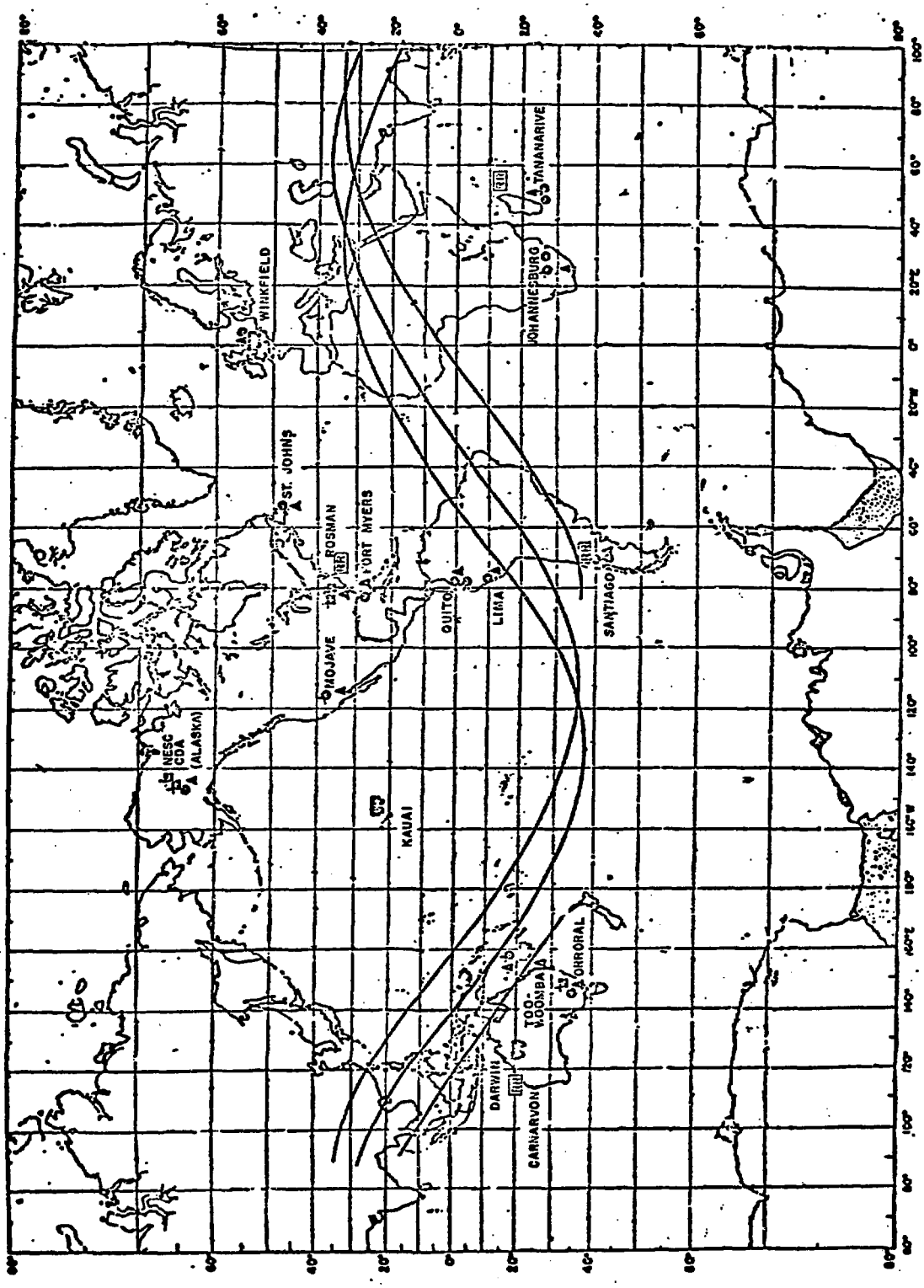
WINKFIELD
ST. JOHNS
ROSMAN
FORT MYERS
MOJAVE
NESC
COA
(ALASKA)
KAUAI
QUITO
LIMA
SANTIAGO
JOHANNESBURG
TANANARIVE
DARWIN
TOO-
WOOMBA
OHRORAL
CARNARVON

TABLE 1

SUMMARY OF ORBITAL CONDITIONS

Launch date	August 9, 1969
Height of perigee	482 km
Height of apogee	540 km
Inclination to equator	33°
Orbital period	90 minutes
Spin period	2 seconds
Mean temperature of instrument	13°C
Actual life time of instrument	28 months

C. Objectives of the OSO-6 Neutron Experiment

The principal objectives of the high energy neutron experiment aboard the OSO-6 satellite were to measure the energy spectrum and angular distribution of the high energy neutrons which are produced in the earth's atmosphere and to evaluate the energy spectrum of solar neutrons (quiet and flare associated). Such a measurement was expected to help understand physically some of the high energy processes that occur in the terrestrial and solar atmospheres and in the interplanetary medium. Perhaps one could verify the assumed neutron spectrum used in explaining the population of protons from neutron decay in the inner zone Van Allen radiation belt. Current research, Farley and Tomassian [1970], suggests that the measured and calculated inner zone proton intensities can be ascribed to both a neutron decay mechanism and an inward radial diffusion of the outer zone protons.

An attempt might be made to study the neutron data related to orbital passes through or near the Southern Atlantic anomalies. It is possible that these anomalies do indeed serve as a source of neutrons which upon decay populate the various zones of radiation belts with electrons and protons.

This work will be devoted to discussing the detector development and correlation between solar neutron measurement and solar flare activity.

II. DESCRIPTION OF THE OSO-6 NEUTRON EXPERIMENT

A. Requirements and Design Considerations

As stated earlier the primary objective of the University of New Mexico high energy neutron experiment aboard the OSO-6 satellite was to measure the energy spectrum and the angular distribution of neutrons which are produced in the earth's atmosphere, and to detect the high energy spectrum of solar neutrons and/or solar albedo neutrons. From the experimental results perhaps one can gain a better physical insight into the various high energy processes that occur in the terrestrial and solar atmospheres and in the interplanetary medium.

The energy interval (20-160 MeV) was chosen to avoid thermal and fast neutrons at the low energy end, and to avoid the absorptive processes for the recoil protons such as the meson production region at the high energy end. It was important that the upper proton recoil energy limit be chosen such that coulomb scattering and absorption effects were not too significant. Multiple coulomb scattering at proton recoil energies of 9.5 MeV (range 1 cm) and 150 MeV (range 15.41 cm) amount to 0.1479% and 0.1212%, respectively. The probability of inelastic nuclear interactions at these energies are 1.873% and 25.754%, respectively, Janni [1966]. Measday and Richard-Serre [1969] at CERN have pointed out that Janni's [1966] numbers are somewhat high for the probability of nuclear inelastic interactions. For example, Measday calculates at 150 MeV an interaction rate of 17.26% for a CH scintillator case where he used the reaction cross section less the excitation of the 4.43 MeV level in ^{12}C. Many experimental results

agree quite well with Measday's numbers. The upper recoil proton energy limit was also somewhat dictated by the size of the spacecraft compartment assigned to the UNM group.

An important reason for choosing the OSO-6 satellite for this particular experiment was that the satellite orbit was circular and below the inner Van Allen belt. These conditions markedly simplified the analysis of the neutron data since we were able to observe both primary solar neutron fluxes and earth albedo neutrons without a large charged particle background, except for passes near or through the South Atlantic anomaly where high charged particle fluxes do exist.

Although the choice of a telescopic arrangement of scintillation counters leads to low efficiencies, it was felt that with a possible 6-12 month instrument lifetime at satellite altitudes outside the earth's atmosphere sufficient data could be accumulated to satisfy the statistical requirements. The instrument has operated successfully for 28 months. Furthermore, the telescopic geometry provided adequate directional characteristics and energy resolution.

The instrument, Pearson and Waitz [1969], which is shown in Figures 5-11 consisted of five independent plastic scintillation counters. Let us designate the five counters as C1, C2, dE, E, and G as shown in Figure 8. C1 and C2 serve as a source for the proton recoils while the dE and E counters identify the proton recoil and determine the energy of the proton recoil. A scintillation counter was chosen for its hydrogen content since we wanted to employ the proton recoil process for detecting neutrons. However, since the atomic ratio of hydrogen to carbon for this particular plastic (Pilot B) is

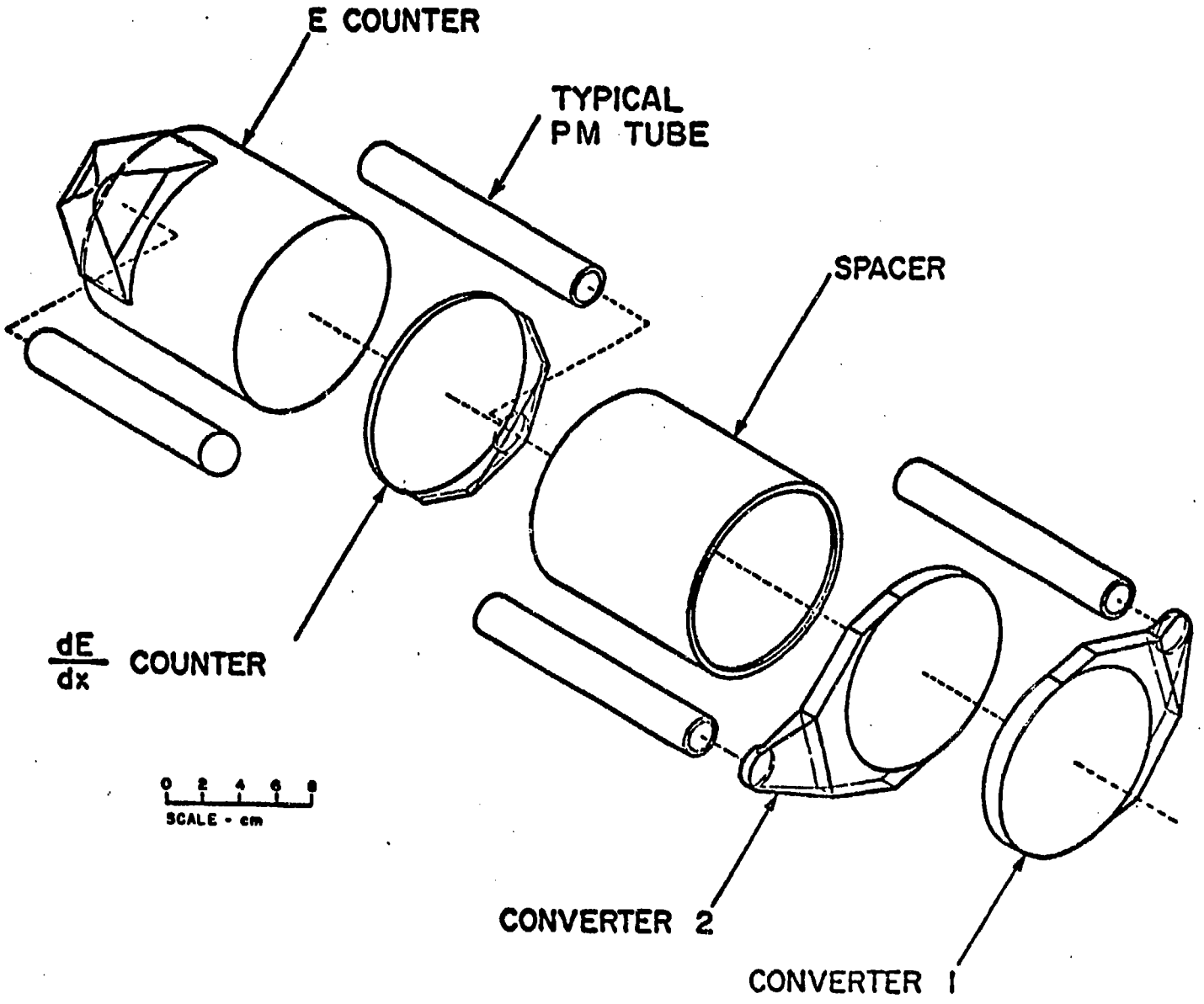

Fig. 5. Inner Stack of Counters; C1, C2, Spacer, dE, and E.

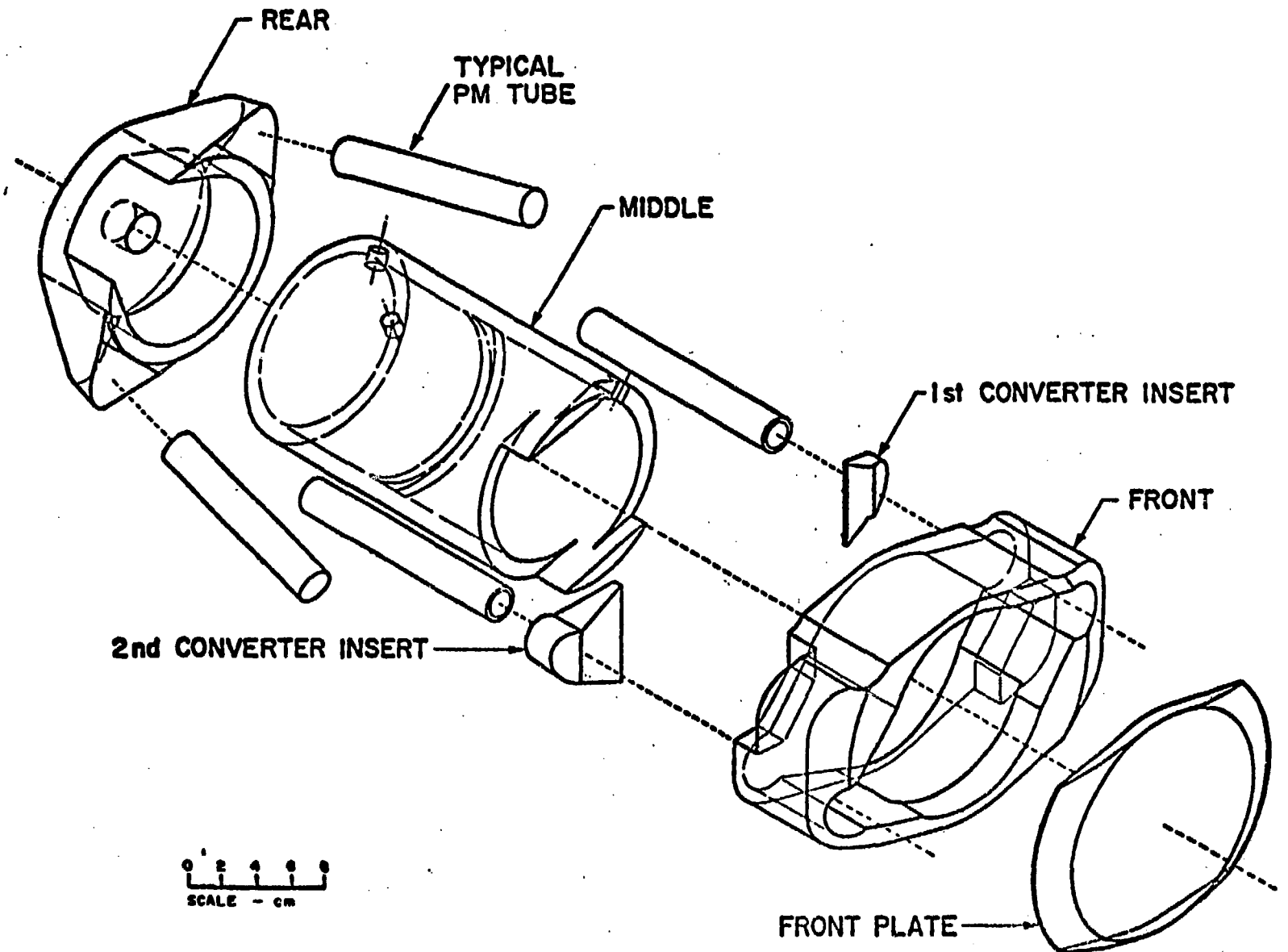

Fig. 6. Outer Stack of Counters; Guard.

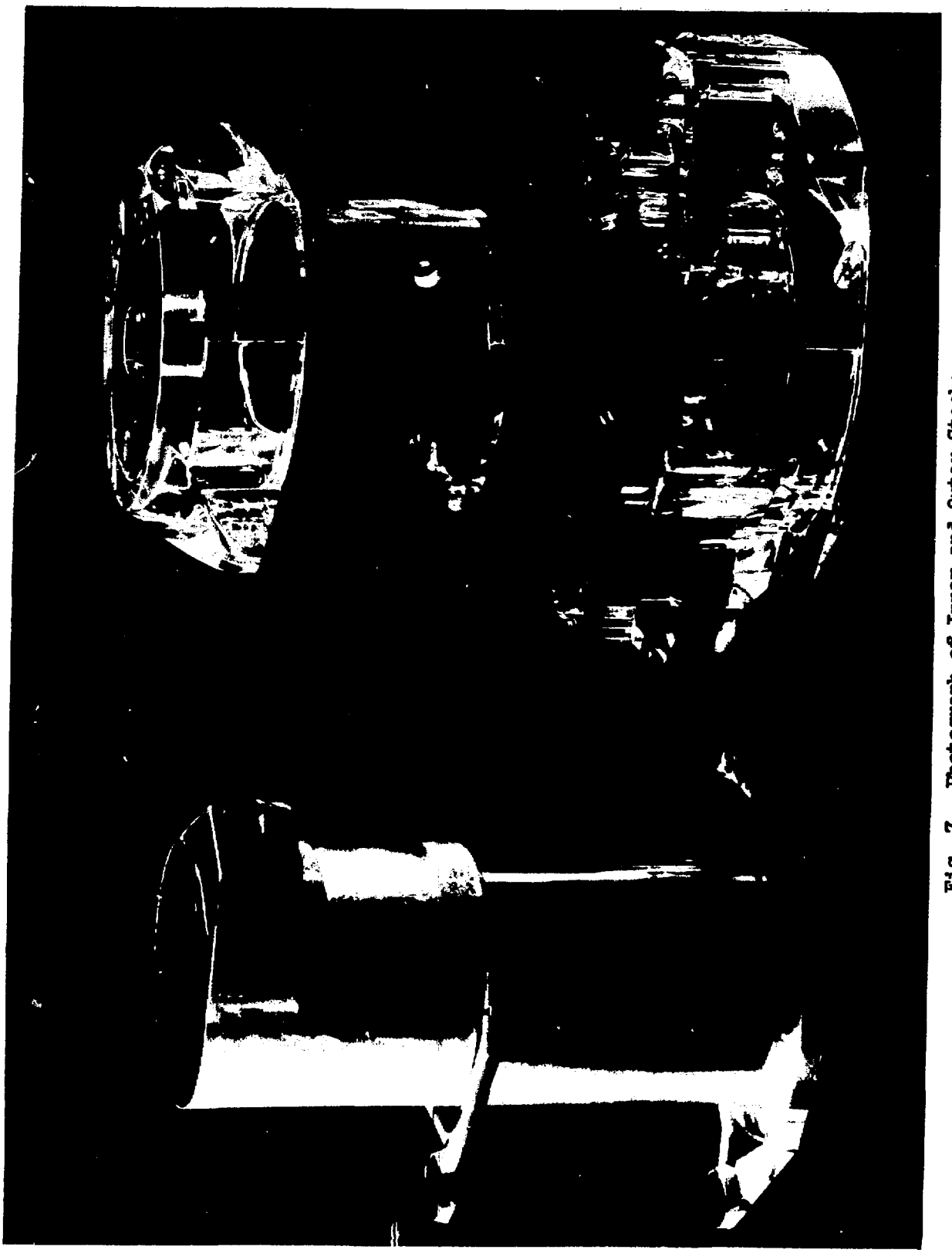

Fig. 7. Photograph of Inner and Outer Stacks.

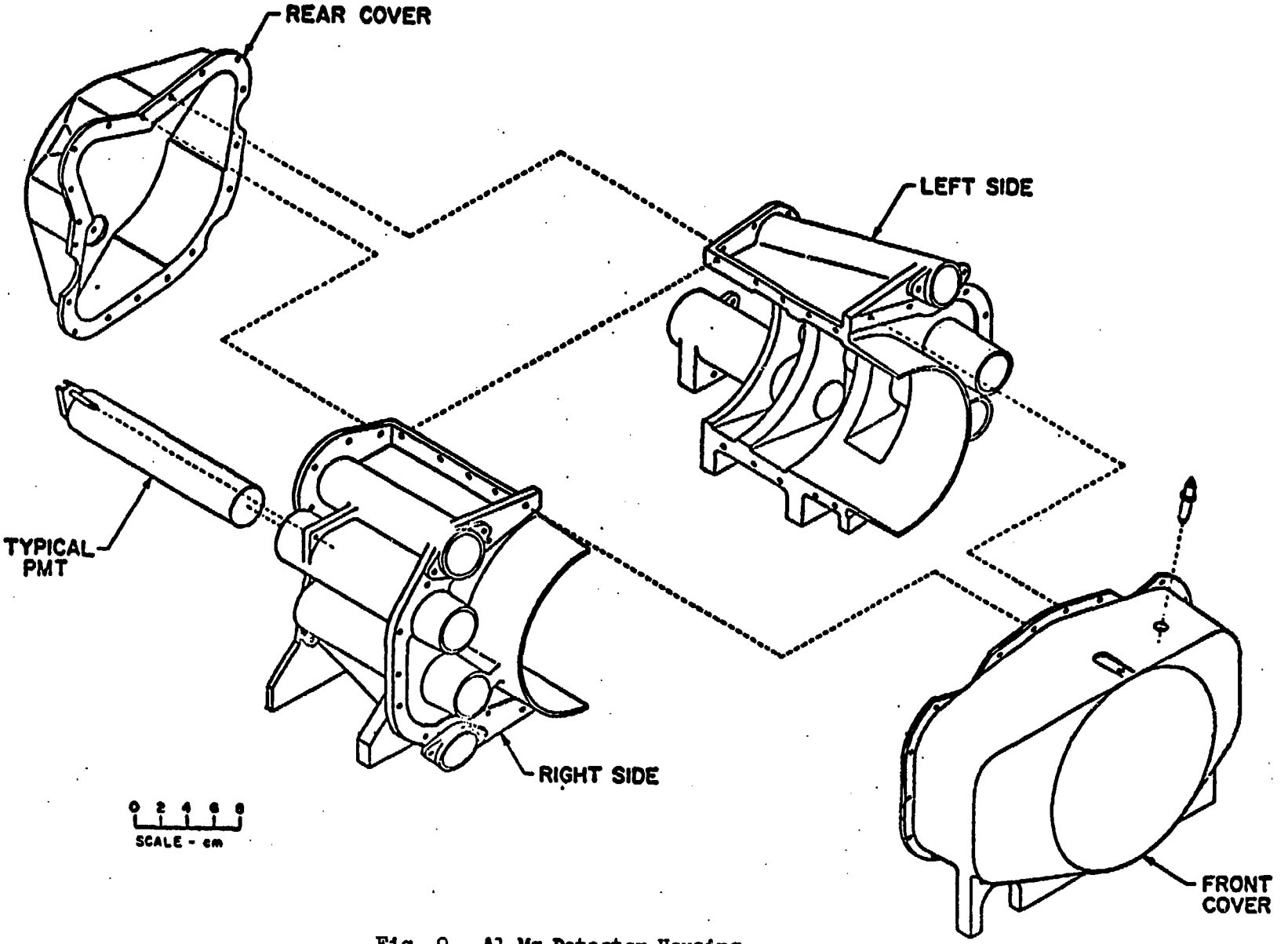

Fig. 9. Al-Mg Detector Housing.

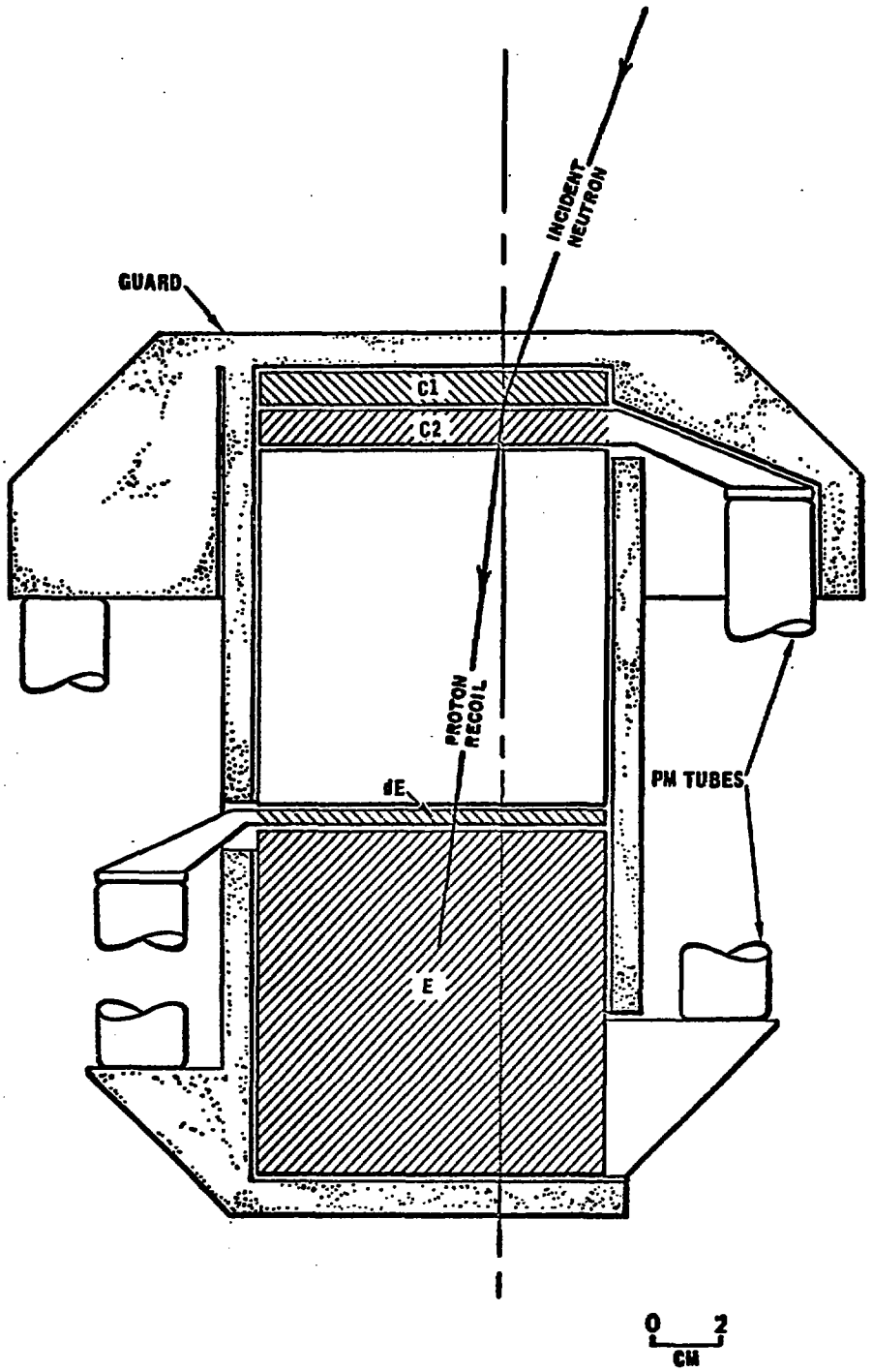

Fig. 8. Simplified Diagram of UNM High Energy Neutron Detector, and a Neutron Producing a Proton Recoil in C1.

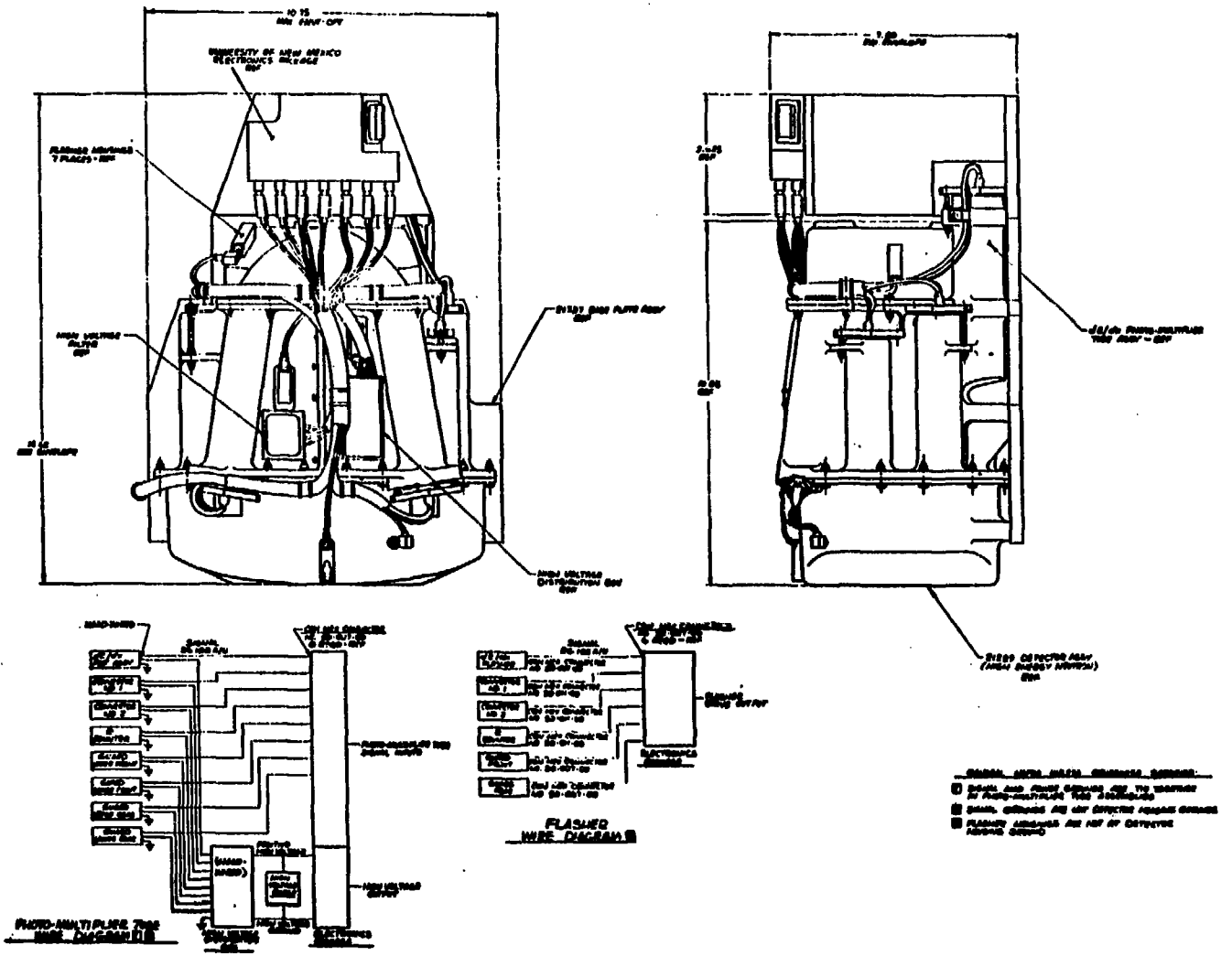

Fig. 10. Configuration Outline of UNM High Energy Neutron Experiment.

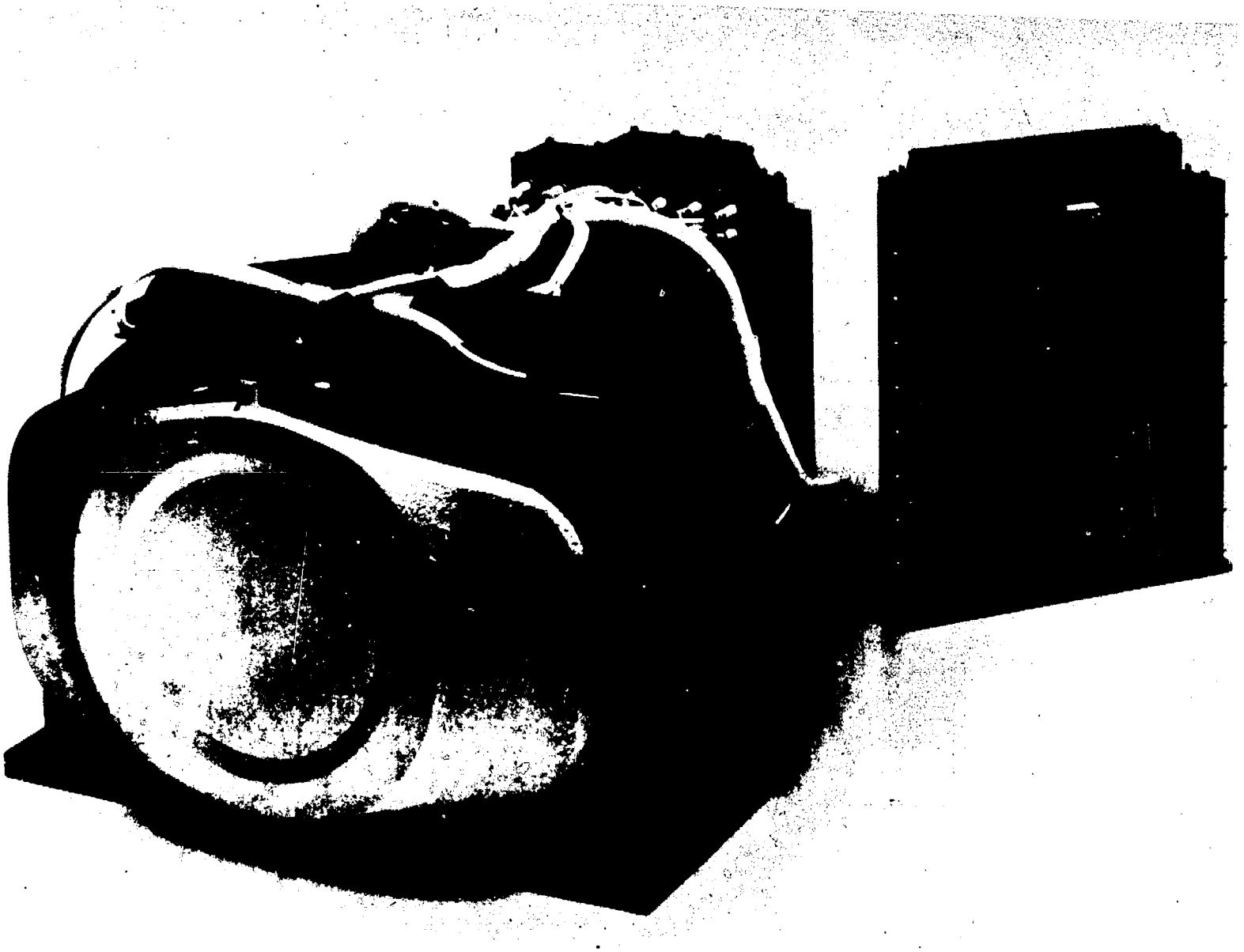

Fig. 11. Photograph of UNM High Energy Neutron Detector and Electronics.

H/C = 1.10 we do have to correct for events that result from the neutron-carbon quasi-elastic interaction. The Pilot B scintillating plastic was chosen for its pulse height and decay time characteristics. Chemically Pilot B contains p-terphenyl and p,p'-diphenylstilbene as scintillator and wavelength shifter, respectively.

Since the C1 and C2 counters are made of a scintillating material, the identification and energy determination of neutrons which are incident from the back side of the instrument and produce recoils which stop in these counters can be accomplished. The set of four counters C1, C2, dE, and E arranged symmetrically along a detector axis was embedded in a guard scintillation plastic jacket which we have designated as G. The purpose of the guard counter was to eliminate the unwanted charged particle background and to detect neutron and gamma-ray events which fail to satisfy energy and/or directional characteristics of the instrument.

The counters C1 and C2 were mechanically separated from the counters dE and E by an aluminum spacer (Figure 5). Considerable effort, Pearson and Waitz [1969], was spent in the design of this aluminum spacer which had to meet many of the thermal and mechanical specifications as outlined by NASA. Also, it was necessary to minimize the proton-recoil producing volume of this spacer.

Light pulses generated in the counters C1, C2, dE, and E which result from ionization losses of the incident proton recoils and other charged particles are transmitted to the photoelectric surface of the photomultiplier tubes through highly polished acrylic solid light pipes. Some study was devoted to the homogeniety of light collection in the counter-light pipe assembly. At UNM, tests of uniformity of

light collection using various designs of dummy lucite counters were conducted. The final design chosen was a compromise between uniformity of light collection and space requirements. Deviations from homogeniety were attributed primarily to the design of the light pipe, Pearson and Waitz [1969], Garwin [1952], Akimov [1965]. As pointed out by Garwin [1952],one can conduct essentially all the light traveling by total internal reflection along a light pipe of any cross-sectional shape into another light pipe of any other cross-sectional form, as long as the cross-sectional areas of the light pipes are equal. The only requirement on the transition section is that it be adiabatic, i.e., have small angles of taper and maintain constant area. Considerable effort, Pearson and Waitz [1969], was spent in finding suitable bonding materials for use at the scintillation plastic-light pipe interfaces which had to withstand the many pre-launch specifications. Furthermore, these bonds had to have an index of refraction which matched to within certain limits the indices of refraction of both the scintillation plastic and the acrylic light pipes.

A sophisticated method, Pearson and Waitz [1969], for mounting the eight photomultiplier tubes (EMI 9734NA) into the detector was devised. Each photomultiplier tube with its circuitry was spring loaded between the detector housing and light pipe-photocathode interface. A clear resilient dielectric gel was inserted at the light pipe-photocathode interface for light coupling. The above arrangement allowed enough elasticity between the photomultiplier tube and detector housing-light pipe interfaces to satisfactorily meet the many pre-launch vibration tests while maintaining optical contact.

A light-tight cast Al-magnesium alloy detector housing, Pearson and Waitz [1969] (Figure 9), was fabricated which supported and protected the guard counter C1, C2, dE, E, counter-photomultiplier tube assembly. This housing with its electronic package was mounted onto an aluminum base-plate which could be installed (Figure 2) into the assigned spacecraft compartment. Another UNM electronics package was mounted in an adjacent compartment as seen in Figure 3. The total UNM experimental package consisted of a scintillation detector assembly and two electronic packages which were mounted in two separate compartments. The amount of material (gm/cm^2) on the front side of the instrument was minimized to try to limit the local production of neutrons which would represent an undesirable background. The front side of the instrument which faces the space environment was painted silver to help control the mean temperature of the instrument and the spacecraft.

B. Construction of the Detector

Four detector units were constructed which were designated as pre-prototype, prototype, flight-type, and spare-flight-type. The pre-prototype unit was fabricated in-house at the University of New Mexico Physics Department, and was flown to balloon altitudes in October 1968.

Using the basic design of the pre-prototype three other detector units were constructed under a sub-contract with the Ball Brothers Research Corporation, Boulder, Colorado. A BBRC report, Pearson and Waitz [1969], discusses the results of this work which included the

fabrication, assembly, test and operation of the detector units.

Design, fabrication, thermal and vibration testing, and testing of the electronic packages and the photomultiplier tube circuit-photomultiplier tube assemblies were conducted in-house at the University of New Mexico Physics Department. Also, electrical and mechanical integration, and calibration was done in-house.

Considerations in terms of the physics of the problem and the size of the assigned spacecraft compartment dictated the resultant geometric design of the instrument.

Extreme care was exercised in the fabrication (machining, polishing, annealing) of the various shapes and types of plastic scintillators, and of the various shapes of acrylic light pipes. The Pilot B type scintillation plastic was used for the C1, C2, dE, and E counters while the Semi-Elements polyfluor was used for the guard counter assembly.

Although thin curled acrylic (thermally formed) light pipes offered better light transmitting efficiencies, Gibson [1964], over solid acrylic (machined, polished, annealed) light pipes, reproducibility production requirements for the thin curled acrylic light pipes were difficult to satisfy. Also, since the C1, C2, and E counters required light pipe thicknesses of 1 cm or greater, thermal forming of these light pipes proved to be an impossible task.

Much effort, Pearson and Waitz [1969], was devoted to the proper selection of optical coupling materials for the scintillation plastic-acrylic light pipe interface and for the acrylic light pipe-photomultiplier tube cathode interface. The assembly of scintillator-light pipe-photomultiplier tube with its optical coupling materials had to

operate properly before and after being subjected to the many mechanical, thermal, vacuum, and electrical pre-launch test specifications. Each scintillator with its light pipe was carefully wrapped with aluminum foil, and a coat of highly opaque paint was applied over the aluminum foil to ensure a light-tight configuration. Each of the five counters C1, C2, dE, E, and G was carefully tested individually for the existence of light leaks. Any light leak between any two counters would have seriously modified the proper performance of the instrument.

A detector housing (Al-Mg alloy, sand-cast) which was mounted to an aluminum baseplate (chromicote finish) supported and protected the assembly of counters and their photomultiplier tubes.

The inner stack (Figure 5) which consisted of C1, C2, an aluminum spacer, dE and E counters was spring-loaded symmetrically along the detector axis relative to the rear cover of the detector housing. The outer stack (Figure 6) which consisted of the anticoincidence guard assembly was spring-loaded in a similar fashion. The necessity of spring-loading these stacks relative to both the spring-loaded photomultiplier units and the rear cover of the detector housing resulted from observed relative motions among the various detector components during thermal and vibration tests. The above mentioned aluminum spacer which was positioned between C2 and dE was designed to meet certain mechanical requirements such as stress limits to prevent buckling and to minimize the amount of material (gm/cm^2) it represented. The number of protons originating in this material was thus minimized.

The C1, C2, dE, and E counters were each assigned a Type PEX 1303 P-N diffused gallium phosphide diode green light source (Texas Instruments, Inc.), and the guard was assigned two light diodes (Figures

12, 10, 15). When properly pulsed in the forward direction, the diode emits green light of relatively narrow spectral width. Testing of these diodes in the prototype instrument indicated adequate stability in the electrical, thermal, mechanical, and spectral characteristics for use in the flight-type instrument. The light from these diodes serves to simulate a scintillation event upon command from a ground station. This technique allows the calibration and diagnosis of instrument response characteristics under flight conditions. Although the light diode emits radiation which does not match the S-11 spectral response of the photomultiplier tube and is therefore somewhat inefficient, suitable pulsed electrical drive on the diode provided adequate response at the anode of the photomultiplier tube. See Figure 13 for an example of in-flight calibration cycle from the quick-look data. Table 2 gives the digital data format and Table 3 gives the analog data format.

It will be noted in Figure 13 that the events immediately following the initiation of the read-out cycle appear to be random in character. This is because the calibration pulser generates a sequence of monotonically increasing pulses at the rate of one pulse per read-out frame. The first few pulses are below the threshold of the coincidence circuits and so do not appear. Eventually a sequence of pulses identified as neutral (ID=2) occur with increasing pulse heights evident. Although the guard counter has pulsers, the levels are still not above guard threshold. When the pulses rise above guard threshold a sequence of simulated charged events (ID=1) occurs. Thus the performance of the guard counter can be monitored as well as all the other counters. In

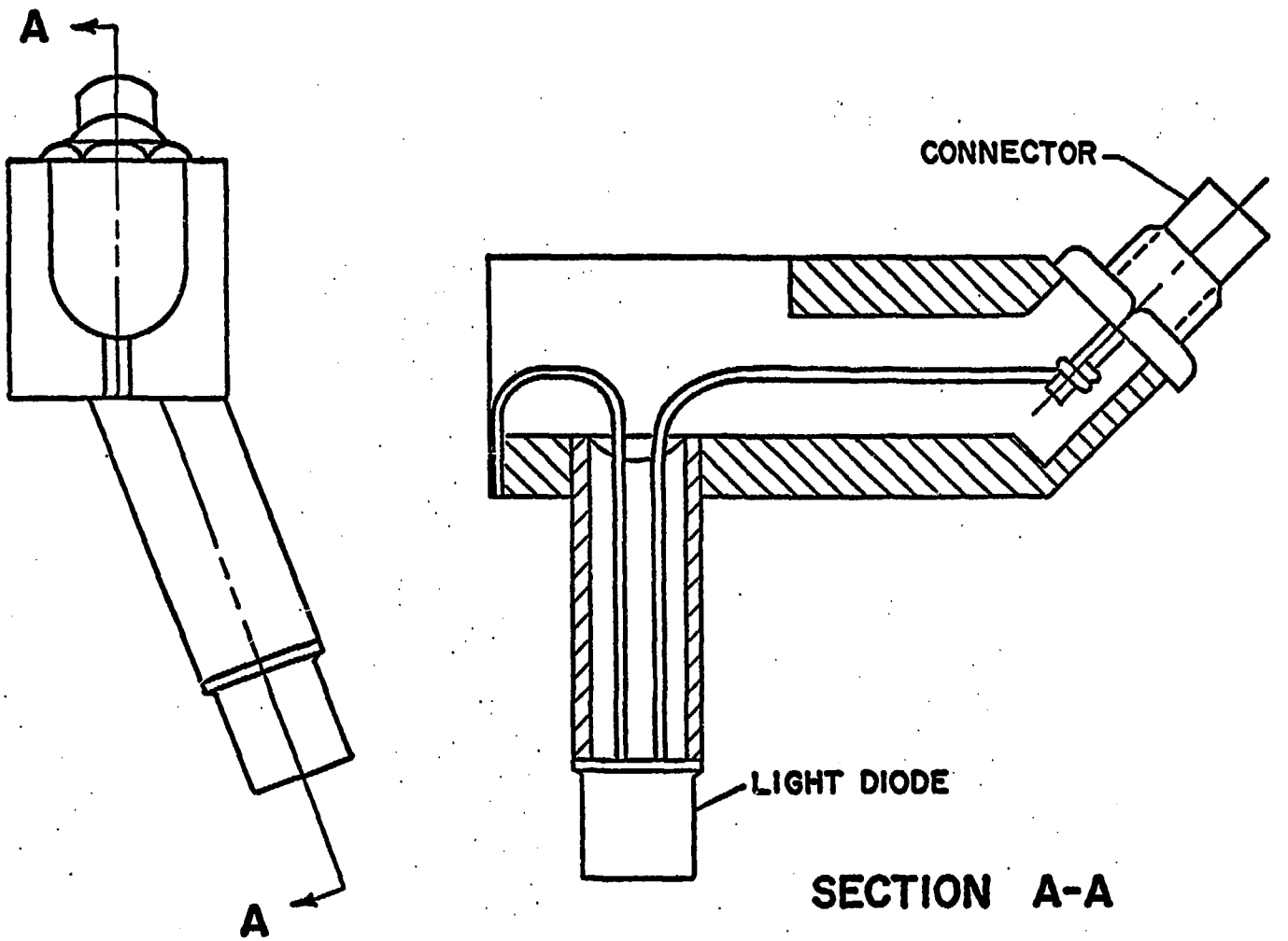

Fig. 12. Housing and Connector Assembly for Light Diode Used in Calibration Cycle.

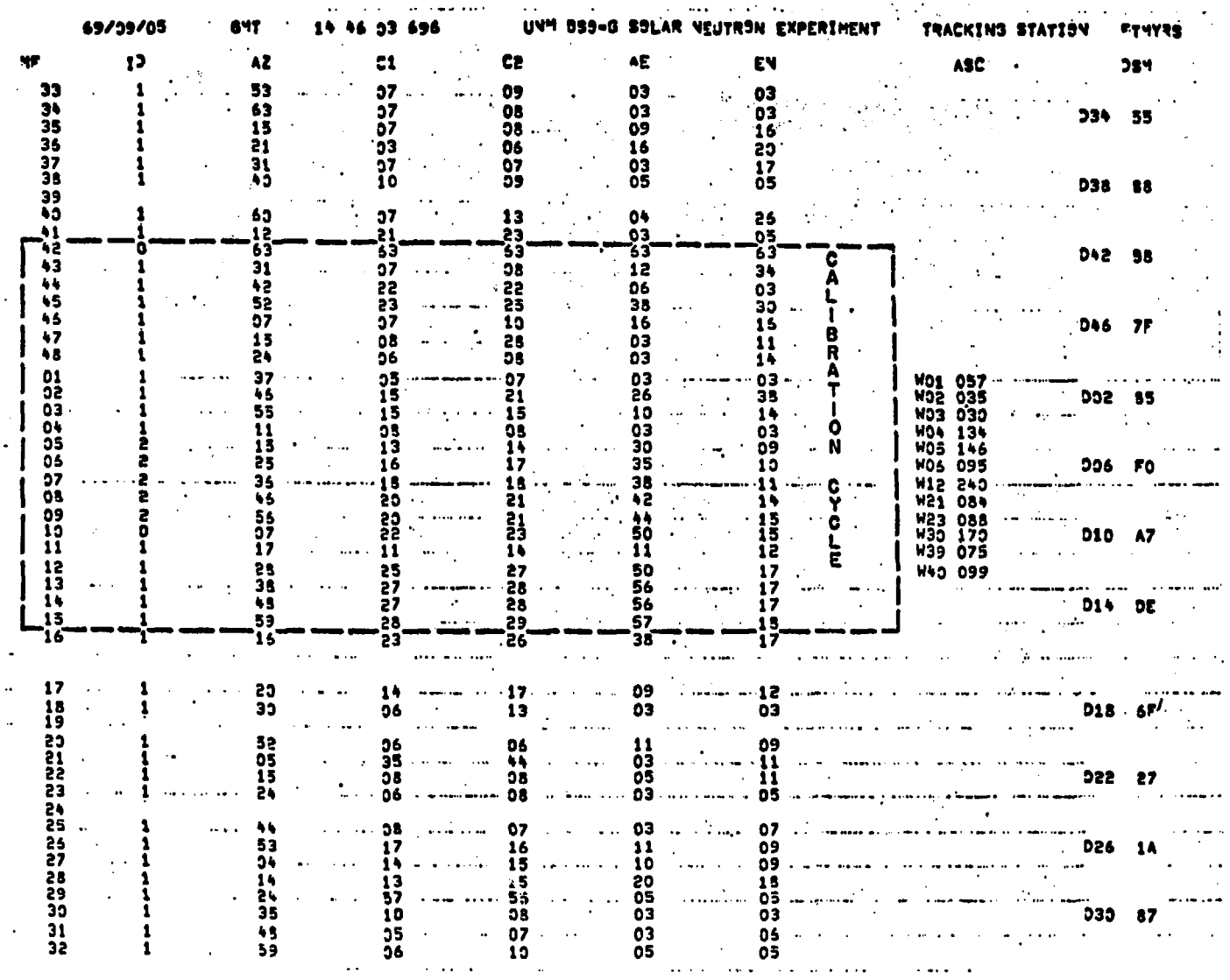

Fig. 13. Example of Quick-Look Data Showing Some Proton Data, a Calibration Cycle, and Some Housekeeping Data.

TABLE 2

DIGITAL DATA FORMAT

MAIN FRAME DATA

|←MF 14→|←MF 15→|←MF 16→|←MF 17→|

2^7 ← 2^0 2^7 ← 2^0 2^7 ← 2^0 2^7 ← 2^0

X X X X X X X X X X X X X X X X X X X X X X X X X X X X

A B|←C→|←D→|←E→|←F→|←G→|

2^5 ← 2^0 2^5 ← 2^0 2^5 ← 2^0 2^5 ← 2^0 2^5 ← 2^0

A = 1	B = 1	No Event
A = 1	B = 0	Neutron Event
A = 0	B = 1	Proton Event
A = 0	B = 0	First Readout of Calibrate Sequence

C = 4 to 63	0 to 60 Angular Incremenets from Sun (6 deg)
D = 0 to 63	C1 Scintillator Pulse Amplitude
E = 0 to 63	C2 Scintillator Pulse Amplitude
F = 0 to 63	dE Scintillator Pulse Amplitude
G = 0 to 63	E Scintillator Pulse Amplitude

DSM DATA

|←18→|←22→|←26→|←30→|

Check Work for Main Frames 1-16

|←34→|←38→|←42→|←46→|

Check Work for Main Frames 17-32

|←2→|←6→|←10→|←14→|

Check Word for Main Frames 33-48

X X X X X X X X X X X X X X X X X X X X X X X X X X X X

2^7 ← 2^0 2^7 ← 2^0 2^7 ← 2^0 2^7 ← 2^0

LSB

TABLE 3

ANALOG DATA FORMAT

	ASC Frame			
ASC Word	1	2	3	4
1	Guard CR 000-255	Guard CR 000-255	Guard CR 000-255	Guard CR 000-255
2	C1 CR 000-255	DE CR 000-255	C2-DE CR 000-255	Neut CR 000-255
3	C2 CR 000-255	E CR 000-255	C2-DE-E CR 000-255	Prot CR 000-255
4	+6v Mon. 130±20	+3v Mon. 130±20	Hi Volt Mon. 230±20	Clock Rate 127±25
5	-6v Mon. 150±20	-3v Mon. 150±20	Temp 1 190±25	Temp 2 127±25
6	ID1 026-060	ID2 061-111	ID3 112-156	ID4 156-230

Mon. - monitor

CR - count rate

addition the solar clock can be checked as the spacing between calibration pulses is fixed.

A mechanical method for mounting the scintillator-light pipe-photomultiplier tube assemblies with their optical coupling materials was devised to withstand certain sinusoidal and random vibration tests. Figure 14 shows a typical photomultiplier mounting. Photomultiplier tubes which were mounted some distance from the surface of the vibration table experienced higher vibration levels because of the transmissibility effect, and consequently, a sound mechanical design had to be formulated in the construction of the photomultiplier tubes.

In the selection of the photomultiplier tubes for this experiment the following requirements were essential: reasonably fast rise-time and transit time, mechanical ruggedness, low noise, high gain at low voltage to insure low power consumption, small size, good stability. To avoid or minimize electrostatic, magnetostatic and electromagnetic influences on the proper operation of the photomultiplier tube a foil made of a special high permeability alloy (Conetic AA) which is not affected by vibration and shock was wrapped around each tube.

C. Operation and Methods of Data Collection

The general arrangement of the detector-electronics system is shown in Figure 15. A stable, very efficient power supply which was designed and fabricated in-house at the University of New Mexico Physics Department provided the necessary high d.c. voltages to the eight photomultiplier tubes and the various low d.c. voltages to the electronic system.

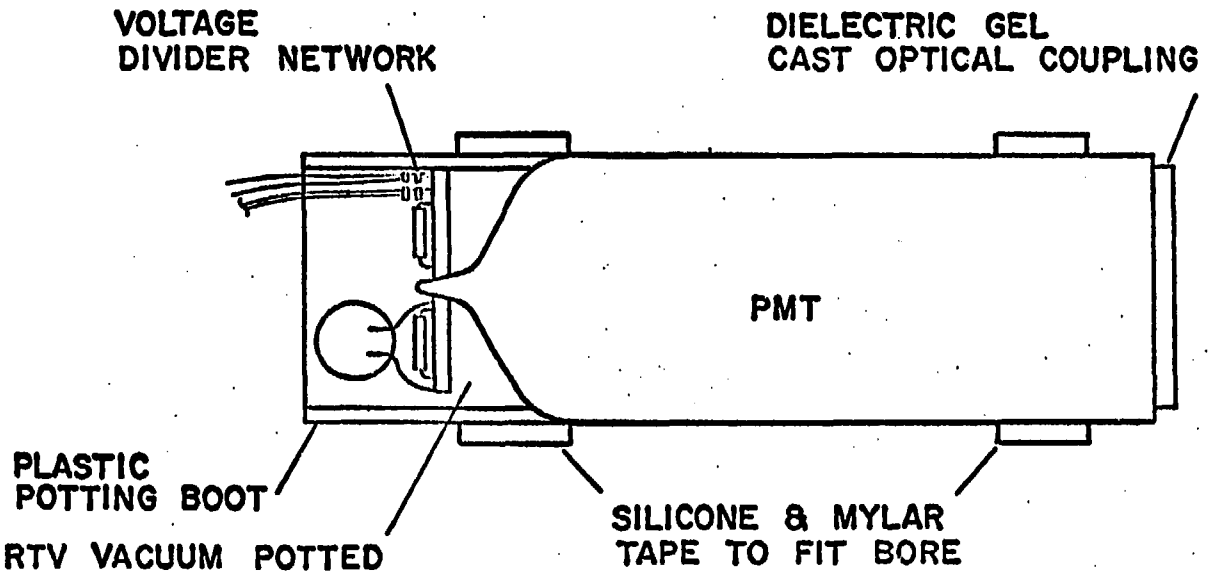

Fig. 14. Photomultiplier Mounting.

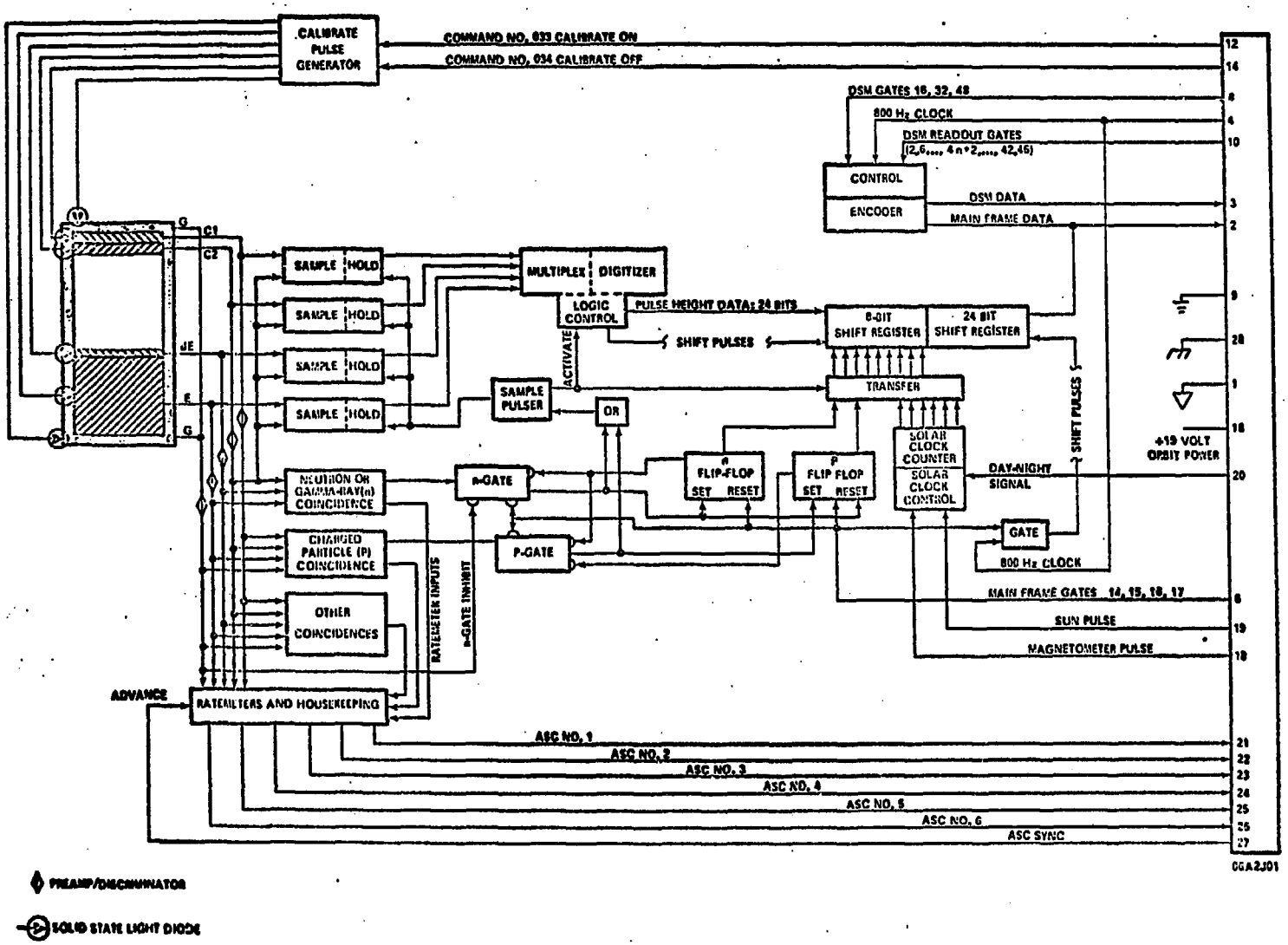

Fig. 15. General Arrangement of Detector - Electronics System.

Since the detector system employs the scintillation technique, it is sensitive to any charged particle that suffers an energy loss greater than some threshold that characterizes each of the five counters: C1, C2, dE, E, and G. This threshold is primarily determined by a discriminator circuit in the front end of the electronics system and the light collection efficiency of each counter. The charged particles that trigger any of the counters are due to the charged and uncharged solar, cosmic ray, and earth albedo fluxes. The neutral flux such as neutrons, gamma rays, and x rays can produce charged particles within the sensitive volume of the detector through the various physical mechanisms such as neutron-proton scattering, Compton scattering and pair production. An important consideration in the design of a neutron detector is the employment of an anti-coincidence counter which can eliminate with high efficiency the unwanted background of charged particles and undesirable neutron and gamma-ray events. This was accomplished by surrounding the C1, C2, dE, and E counters with a scintillation guard counter jacket of adequate thickness. Four properly located photomultiplier tubes were coupled to the guard counter to maximize the anti-coincidence efficiency. Although certain small unguarded regions existed, their geometry requires a high energy charged particle (proton) to experience scattering angles (proton-proton interaction) from approximately 90° to 135° in the lab frame. However, $\sigma_{pp}(>90°) \equiv 0$.

If a charged particle traverses the counters G, C1, C2, dE, and E, or if a neutron produces a proton recoil that traverses any part of the guard counter, then a fourfold coincidence circuit and a charged

particle identifier circuit are triggered which initiates processing of C1, C2, dE, and E pulse heights for the spacecraft telemetry system. On the other hand, if a neutron (gamma-ray) undergoes conversion in C1 or C2 and if the recoil proton (electron) stops in the E counter after passing through dE, respectively, then a threefold (C2, dE, E) coincidence circuit and a neutron particle identifier circuit are activated.

The resulting pulse amplitude from the E counter is directly related to the energy of the proton recoil which in turn reflects the neutron energy through the nonrelativistic expression $E_p = E_n \cos^2\psi$, or through the relativistic expression $E_p = E_n \cos^2\psi/(1+E_n \sin^2\psi/2m_nc^2)$ where ψ is the scattering angle.

Furthermore, a neutron (gamma ray) that converts anywhere in the sensitive volume of the E counter (energy deposited greater than threshold) must produce a proton (electron) recoil, respectively, with the proper energy and direction such that it stops in C1 or C2. C1, C2, dE, and E pulse heights for these neutral events are also processed for the spacecraft telemetry system. Using the energy-range relationship and energy cutoffs in the C1, C2, dE, and E counters one can identify the events which result from neutrons which are incident either from the front or the rear side of the instrument. Also, one should be able to analyze charged particle events that stop in the front or the rear sensitive volumes of the guard counter. These events in part could represent those neutrons whose energies and directions lie near the inherent energy and direction limits of the detector.

If either of the coincidence conditions, G-C1-C2-E or $\bar{G}$-C2-dE-E are satisfied, then the C1, C2, dE, and E counter outputs which are first

fed into pulse discriminators and preamplifiers are examined by a 64-channel pulse height analyzer and processed into the spacecraft telemetry system. If both a neutral and a charged event occur within the same readout period (0.32 sec), then the neutron takes precedence in being processed. It should be pointed out that this instrument is sensitive to low energy gamma rays. However, these events can be identified and separated from the neutron data, and this will be discussed further in Section III.

The following single and coincidence counting rates were measured to provide consistency checks on the observed data: C1, C2, dE, E, C2-dE, C2-dE-E, $\bar{G}$-C2-dE-E, and G-C1-C2-E. The notation G-C1-C2-E defines a four-fold coincidence among the G, C1, C2, and E counters. Other housekeeping measurements (Figure 13) which were made to monitor the performance of the instrument included low and high voltages, temperature, and the solar clock rate. Table 3 gives analog data format.

In order to provide a determination of the spacecraft orientation in the spin plane a solar clock was incorporated into the electronic system. Each time the spacecraft solar eye viewed the sun a solar pulse was electronically produced and the period between two consecutive solar pulses thus represented one revolution of the detector in the spin plane. This period was divided by circuits in the UNM experiment into 60 equal increments, and whenever an event occurred it was tagged with a spin orientation number to an accuracy of $\pm 6^{\circ}$. However, during satellite night this solar clock was converted into a magnetometer clock which used the satellite magnetometer data. It should be expected that during the onset of geomagnetic storms the satellite magnetometer data could give erroneous orientation information.

Since it was desirable to monitor the response of the detector/electronics system under flight conditions, an in-flight calibration method was devised which employed light emitting solid-state diodes. A monotonically increasing pulsed current source which was activated at regular intervals by command from a ground station drove the six light diodes in coincidence. Assuming that the current source and the characteristics of the light diode were stable this technique proved to provide an adequate in-flight calibration method.

The main frame data 32-bit word (Figure 16 shows an example of some neutron events) is read out every 320 msec, and since the read-out gate is 40 msec wide the readin time available is 280 msec. Table 4 explains the format for the neutron data. The spin angle binary 6-bit word represented an angle from 0°-360° in units of 6°. Each of the C1, C2, dE, and E binary 6-bit words represented pulse heights from 50 mv-2000 mv. In addition to the main frame data word, this experiment employed six analog subcommutated channels which were sub-subcommutated to provide 17 housekeeping (count rates, low and high voltages, temperatures, solar clock rates) data channels which were read out every 61.44 msec.

With any satellite/telemetry system there exist many independent electronic systems that can generate a variety of random electrical pick up and noise that could modify the data. In an attempt to process the UNM data under possible adverse electrical conditions a system was added to the electronics system that would detect, locate and correct main frame data bit errors to a limited extent. The encoder from the bit error correction system operates electronically on a block of 16 main frame data 32-bit words, and generates a 32-bit

TYPE	CODE	DAY	TIME	D/N	ENERGY	LAT	LON	SZA	SPA	ZAP	ZASA	GRD	ID	AZ	C1	C2	DE	E	ORBIT
2	0	21	16.487	DA	103.70	28.94	262.39	54.31	132.10	78.18	82.55	59	2	46	3	30	21	12	7066
1	0	21	16.498	DA	39.90	29.67	265.20	53.67	17.91	71.43	85.21	59	2	21	3	17	23	3	7066
2	0	21	16.567	DA	109.05	32.62	283.38	51.78	60.10	15.30	101.65	71	2	34	22	24	17	11	7067
1	0	90	9.214	DA	59.58	-32.52	137.90	96.44	59.91	75.82	157.41	61	2	14	3	19	17	8	3552
1	0	90	9.230	DA	30.42	-32.10	141.82	99.95	138.10	96.34	156.49	65	2	47	3	3	24	3	3552
1	0	90	9.250	DA	48.36	-31.37	146.73	104.41	149.90	67.35	154.70	60	2	59	3	3	24	7	3552
1	0	90	9.273	DA	40.27	-30.25	152.39	109.65	6.01	108.63	151.85	52	2	23	3	3	26	5	3552
1	0	90	9.295	NI	40.51	-28.94	157.63	114.64	19.32	120.64	148.60	54	2	4	3	16	22	4	3552
1	0	90	9.403	NI	63.30	-19.48	181.40	139.34	52.22	127.30	128.48	31	2	12	3	4	19	10	3552
2	0	90	9.871	NI	101.85	30.63	273.20	112.98	80.16	116.12	33.04	63	2	12	3	26	25	13	3553
1	0	90	9.933	DA	67.63	32.73	288.65	99.00	155.90	90.91	24.64	69	2	58	16	24	20	6	3553
4	0	90	9.934	DA	102.70	32.74	288.80	98.86	108.10	64.87	24.58	69	2	42	19	22	19	12	3553
(1)	0	90	9.942	DA	118.57	32.85	290.84	97.06	1.17	95.95	23.87	73	2	24	3	16	11	17	3553
2	0	90	9.952	DA	121.38	32.94	293.48	94.72	48.11	75.66	23.11	67	2	32	3	24	23	16	3553
1	0	90	9.991	DA	35.12	32.72	303.29	86.06	150.10	82.77	22.23	63	2	49	3	10	28	3	3553
2	0	90	10.100	DA	63.74	27.65	329.88	61.38	114.10	86.26	34.23	41	2	43	11	28	21	5	3553
3	0	90	10.111	DA	46.14	26.89	332.19	59.08	71.91	94.90	35.97	38	2	12	3	21	25	4	3553
1	0	90	10.190	DA	33.54	19.72	348.86	41.41	119.90	121.10	50.81	30	2	4	3	9	26	3	3553
1	0	90	10.348	DA	29.99	1.46	17.74	8.50	125.90	121.50	83.12	34	2	63	3	3	23	3	3553
1	0	90	10.486	DA	60.46	-15.10	42.47	26.66	107.90	91.66	111.97	32	2	6	3	19	20	8	3553
(1)	0	90	10.598	DA	59.14	-26.11	65.26	51.55	24.13	66.03	134.50	54	2	28	16	24	21	4	3553
3	0	90	10.659	DA	38.11	-30.25	79.29	65.21	6.21	68.96	145.59	61	2	25	3	15	28	3	3553
3	0	90	10.684	DA	39.48	-31.43	85.29	70.77	23.93	63.68	149.56	65	2	20	3	16	29	3	3553
(1)	0	90	10.714	DA	44.33	-32.45	92.99	77.72	6.01	76.48	153.77	67	2	23	3	5	24	6	3553
2	0	90	10.718	DA	43.35	-32.52	93.80	78.44	101.90	70.42	154.14	75	2	7	3	18	32	3	3553
4	0	90	10.778	DA	62.65	-32.83	109.19	92.05	95.91	68.44	157.86	67	2	8	3	29	20	6	3553
2	0	90	10.924	NI	103.44	-25.24	144.54	125.31	79.81	82.55	140.57	46	2	48	14	27	20	12	3553
4	0	90	10.998	NI	58.18	-17.97	160.02	142.11	77.33	108.71	126.08	36	2	16	3	34	24	3	3553
1	0	90	11.271	NI	38.14	14.81	209.92	154.06	94.66	70.49	68.77	23	2	36	3	3	21	5	3553
2	0	90	11.361	NI	37.16	24.05	227.97	134.03	78.99	117.70	50.41	36	2	10	3	8	32	3	3553
5	0	90	11.363	NI	62.80	24.30	228.58	133.40	25.41	139.25	49.85	36	2	19	3	28	24	6	3553
3	0	90	11.380	NI	50.82	25.72	232.17	129.69	75.60	119.89	46.61	41	2	11	3	27	29	3	3553
4	0	90	11.393	NI	65.51	26.82	235.22	126.61	83.24	115.29	43.97	37	2	10	3	28	19	7	3553
2	0	90	11.444	NI	55.57	30.17	246.91	115.28	74.03	74.57	34.81	47	2	37	15	26	20	3	3553
2	0	90	11.450	NI	80.93	30.52	248.52	113.78	19.60	103.48	33.69	58	2	28	10	30	24	8	3553
1	0	90	11.468	DA	32.62	31.36	252.88	109.75	137.90	90.60	30.82	61	2	61	3	8	25	3	3553
2	0	90	11.582	DA	107.68	32.52	281.70	84.13	95.91	111.41	22.42	75	2	8	21	24	20	12	3554
5	0	90	11.660	DA	59.76	29.08	300.85	66.50	108.10	80.27	30.49	55	2	42	3	31	27	4	3554
3	0	90	11.684	DA	52.88	27.48	306.24	61.24	35.92	75.98	34.24	50	2	18	3	26	27	4	3554
3	0	90	11.936	DA	42.61	0.50	354.92	7.94	48.11	53.09	84.29	37	2	32	3	21	27	3	3554
3	0	90	11.936	DA	38.83	0.45	354.98	7.90	143.90	138.61	84.37	29	2	60	3	16	28	3	3554
3	0	90	11.985	DA	50.82	-5.42	3.36	9.73	48.11	57.23	94.39	32	2	32	3	27	29	3	3554

Fig. 16. Example of Neutron Data.

TABLE 4

NEUTRON RECORD AS PRODUCED BY THE NEUTRON SECOND PHASE PROCESSOR

AZ	ID	C1	C2	DE	E	ENERGY	TYPE	ZENITH ANGLE	RASN LOOK	DECL LOOK	LAT	LON	LPA	LZA	DAY NITE	SZA	SPA	ORBIT	DAY	TIME
← I*2 →						←REAL→		←ZAP	REAL →						←A4→	←REAL →		← I*4 →		←REAL

ZASP GUARD FRAME
→ ← I*2 →

NEUTRON TYPE DEFINITION:
0 - Anomalous Event
1 - Forward Neutron
2 - Backward Neutron
3 - Ambiguous
4 - Carbon Event
5 - Ambiguous Carbon

Error indicator shows how good the data is.
0 - No errors in data
4 - Corrected error in data
8 - Uncorrectable error in data; event may not be valid

Variable contents and units	
ORBIT - orbit number - integer	DECL - declination of the look axis in degrees - real
DAY - Julian day of year - integer	LAT - latitude of the satellite subpoint in degrees - real
FRAME - frame number in record - integer halfword	LON - longitude of the satellite subpoint in degrees - real
GUARD - guard - integer halfword	LPA - angle from experiment look-axis to the moon - real
TIME - time in hours of day of the event frame - real	LZA - angle from local vertical to the moon - real
AZ→E - original data from main frame - integer halfwords	DAY/NITE - satellite day/night indicator; contains the word 'DAY' or 'NITE'
ENERGY - energy of event in MeV - real	SZA - angle from spacecraft vertical to the sun - real
ZASP - angle of spacecraft spin axis from vertical in degrees - real	SPA - angle from experiment look-axis to the sun - real
ZAP - angle of look from vertical in degrees (0° is straight up) - real	
RASN - right ascension of the look axis in degrees - real	

check word which is transmitted on four 8-bit digital submultiplexer words. Consequently, this "super" data 544-bit word would consist of 16 main frame data 32-bit words and four digital submultiplexer 8-bit words. The decoding process can detect and correct any error up to 11 bits in length within each "super" data word.

D. Principal Difficulties Encountered

The principal difficulties encountered in the construction of the experimental package were:

1. Development of "crazed" surfaces on the scintillation counters.

2. Loss of optical coupling at scintillator-scintillator, scintillator-acrylic light-pipe, and at light-pipe-phototube interfaces.

3. Damage to photomultiplier tubes during vibration tests.

4. Difficulty in soldering the p.m. tube circuit to the p.m. tube dynode leads.

5. Existence of air pockets in RTV compound which was used to encapsulate the p.m. tube circuit.

6. Damage to scintillation plastic components during thermal and vibration tests because of relative motion between the plastic assembly and the Al-Mg housing.

The first problem was solved, Pearson and Waitz [1969], by employing proper procedures in machining, annealing, and polishing of the scintillation and acrylic plastic. Much effort, Pearson and Waitz [1969] was devoted (problem 2) to the selection of the proper primer

and bonding material for the various interfaces. The G.E. 4044 primer was used on all interfaces except the light pipe p.m. tube interface. The G.E. RTV-602 compound was used at the C1-light pipe, C2-light pipe, E-light pipe, and the various guard counter interfaces. The guard unit consisted of seven separate pieces. The Dow Corning XR6-3488 compound was used to bond the dE counter to its light pipes which were both coated first with the G.E. RTV-118 compound. The optical coupling compound used between the p.m. tube cathode window-light pipe and p.m. tube cathode window-guard counter interfaces was the Dow Corning Dielectric Gel Sylgard 51.

Failure of the EMI p.m. tubes during vibration tests (3rd problem) resulted from poor workmanship in glass-blowing and resistance welding. After some discussion with the people at the EMI factory this problem was solved.

The fourth problem was solved by formulating the following chemical solution, Table 5, Rosebury [1965], which was used to remove the chromium oxide (Cr_2O_3) layer on the chrome iron dynode leads. Once this oxide layer was removed application of solder to the leads became a simple task.

TABLE 5

BRIGHT DIP FOR CHROME IRON

Acetic acid	75 cc
Nitric acid	25 cc
Hydrochloric acid	10 cc

The fifth problem was solved by devising an encapsulation jig which used vacuum to help move the G.E. RTV-11 compound into regions containing the p.m. tube circuitry. Since the circuit components were tightly packed the sole effect of gravity was insufficient to fill certain regions of the circuit volume with the RTV compound. Also, it was important that a uniform coating of primer be applied to all surfaces which were to be encapsulated. Furthermore, the Centralab high voltage capacitors which were used in the p.m. circuit had to be ordered without the wax impregnation since the RTV compound did not bond to the waxy surface.

Much effort, Pearson and Waitz [1969], was devoted to the sixth problem by the research people at Ball Brothers Research Corp., Boulder, Colorado. An inner stack consisting of the C1, C2, dE, and E counters, and an outer stack consisting of the guard assembly were defined. The inner and outer stacks of counters were separately spring-loaded relative to the rear cover of the detector. Also, the p.m. tubes were spring-loaded relative to the detector housing. The adjustment for the spring loading of the entire detector system was dictated by the need for defining sufficient thermal and mechanical elasticity experimentally compatible with conditions in environmental testing.

E. Calibration

Since we were unable to calibrate the instrument with an artificial neutron beam, four independent calibration methods A, B, C, D were devised. For any given neutron run six distributions were plotted through the use of a computer.

1. dE versus E for neutral events
2. dE versus C2 for neutral events
3. C2 versus C1 for neutral events
4. dE versus E for charged particles
5. dE versus C2 for charged particles
6. C2 versus C1 for charged particles

In method A we used the proton curves 4, 5, 6 to identify the approximate location of the minimum ionizing peak for a charged particle that traversed the entire sensitive volume of the instrument on or near the detector axis. A fourfold coincidence Guard-C1-C2-E was required to define this type of an event. An example of neutron (proton) run is shown in Figure 17 (18), respectively. From the neutron curves 1, 2, 3 (method B) we were able to define regions for allowed forward and backward neutrons as is shown in Figure 19 for C1 = 0 or C1 ≠ 0. These regions identified energy cutoffs for each counter. In the dE versus E distribution in Figure 17 one can note the separation of the neutron events from the low energy gamma-ray events. The computer program that analyzes the data also classifies each neutron event as is noted in Table 4.

Since each of the counters had its own light diode we were able to generate calibration curves (method C) for each counter by driving the light diodes in coincidence with a monotonically increasing current source. These calibration curves also showed the non-linear responses of the photomultiplier tubes. A quick and crude test (method D) consisted of measuring the response of the various counters by using a ^{60}Co radioactive source on an oscilloscope or with a pulse height analyzer. Since the ^{60}Co source can produce two 1 MeV gamma

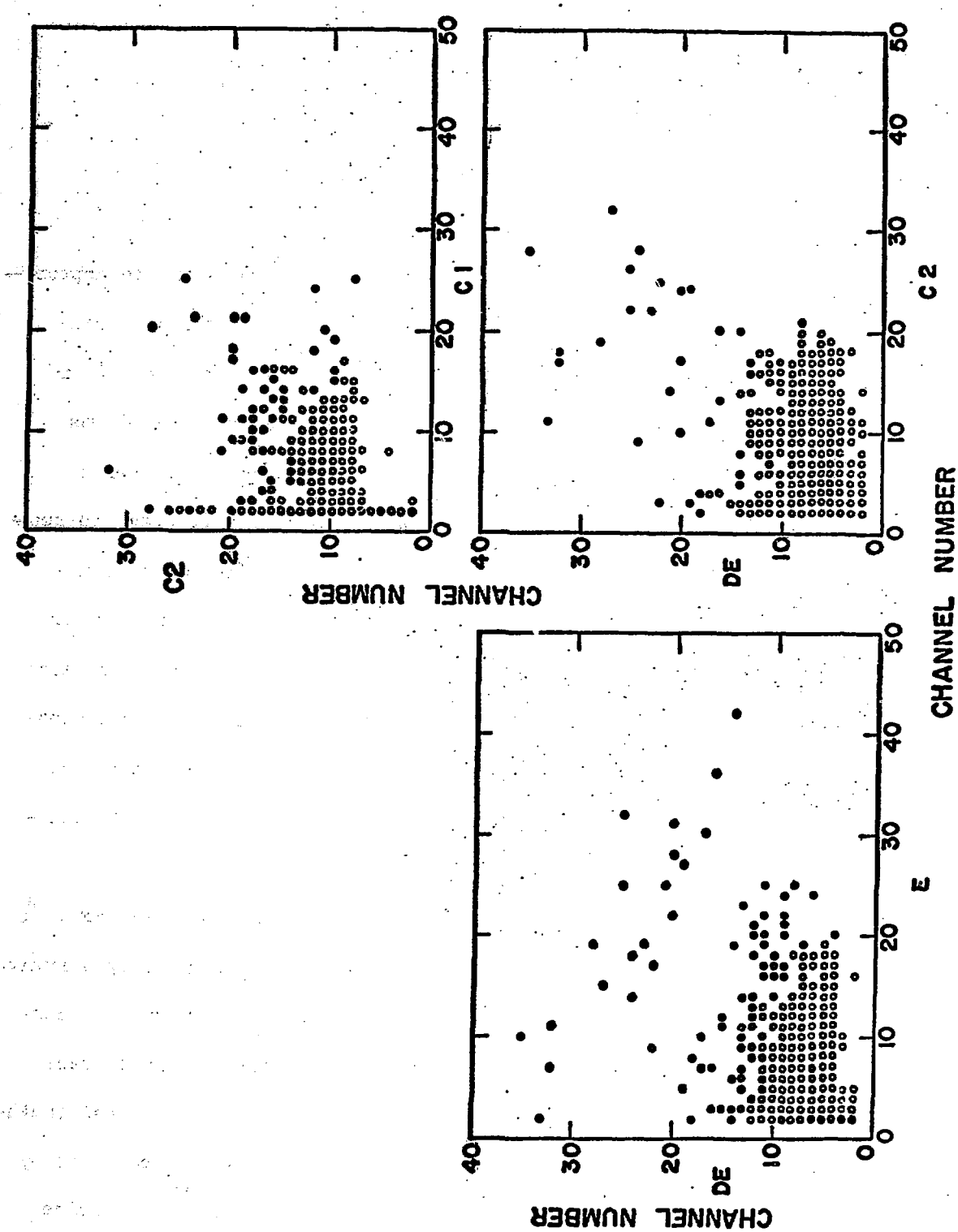

Fig. 17. Example of a Neutron Run at Albuquerque, New Mexico.

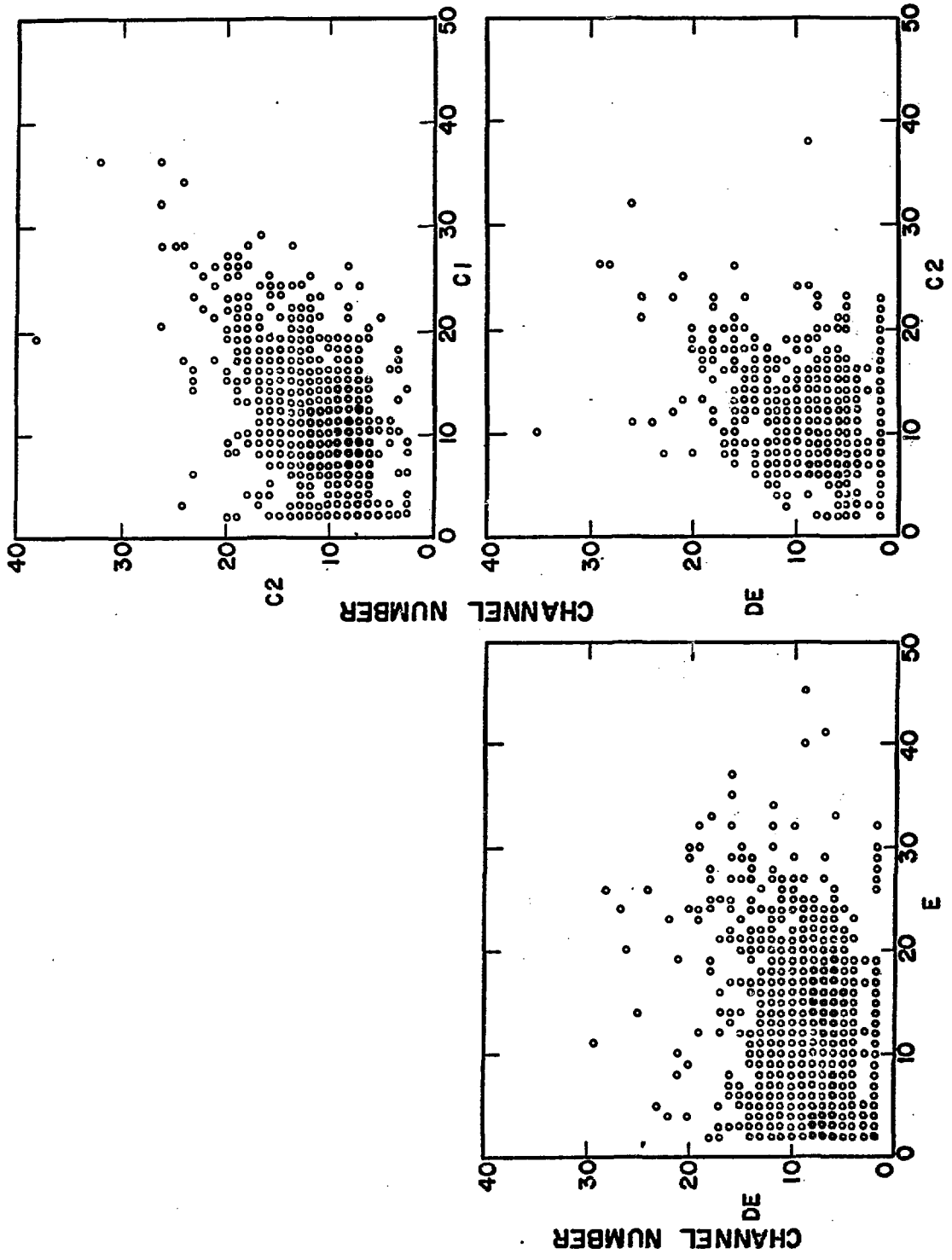

Fig. 18. Example of a Charged Particle Run at Albuquerque, New Mexico.

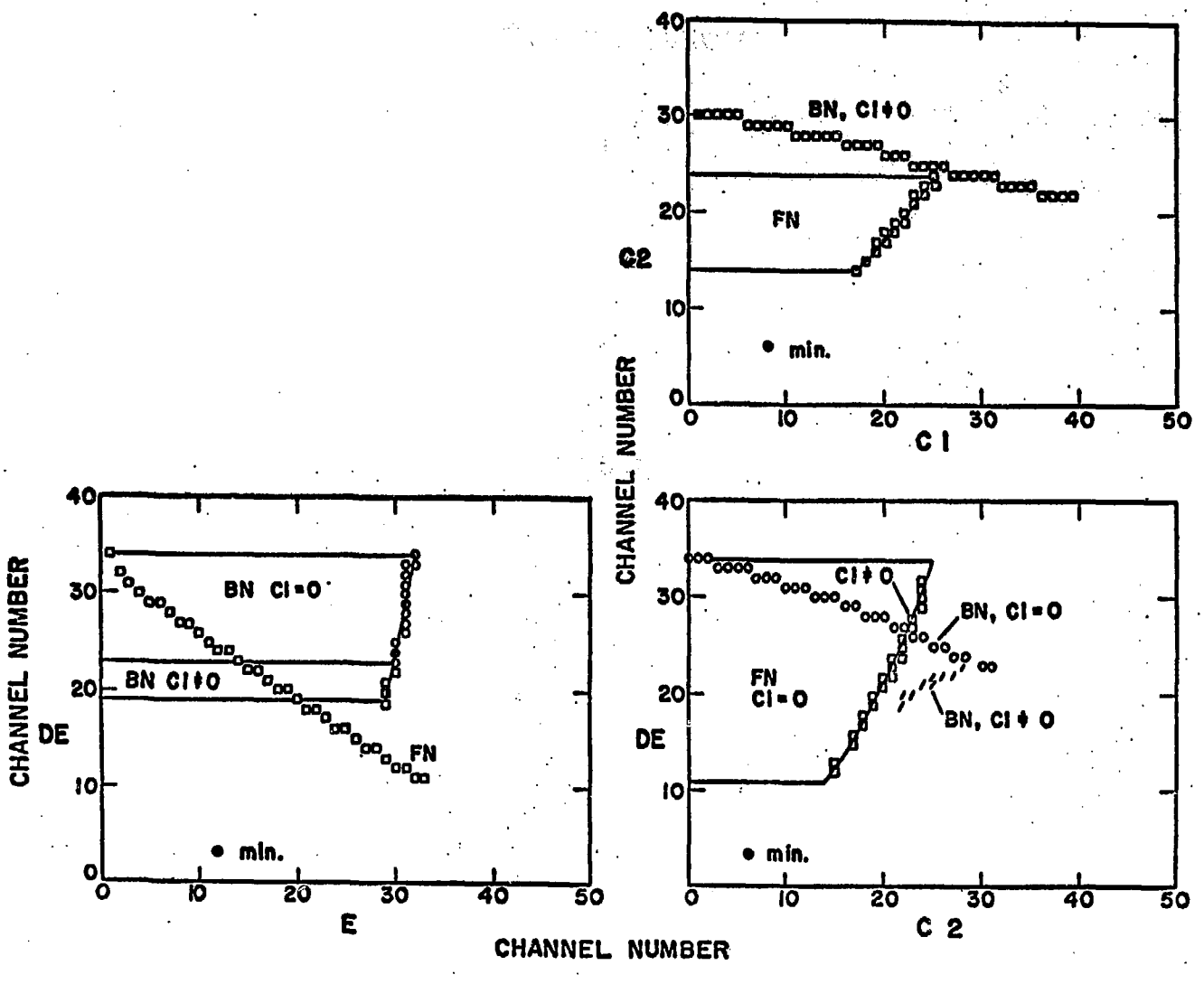

Fig. 19. Allowed Forward (FN) and Backward (BN) Neutron Pulse Height Regions for C1, C2, dE, and E Counters, and for Cases C1 = 0 or C1 ≠ 0.

rays in virtual coincidence, one could see certain detector coincidence rates (e.g., C1-C2 rate) increase depending on the angular correlation of the two gamma rays.

Energy resolution curves from cosmic-ray mesons (method E) for C1, C2, dE, and E were generated by the following procedure (Figure 20). Two inches of lead was used to select μ-mesons of energy $\geq$ 100 MeV. A μ-meson had to traverse μ1-G-C1-C2-dE-E-Pb-μ2 to define a twofold coincidence between μ1 and μ2. With the definition of this coincidence each of the internal counters was studied. Each counter was tested in this manner until enough events are recorded to satisfy statistical requirements. Graphs of typical mu resolution runs are shown in Figure 21. For the thin counters, C1, C2, dE, the mu resolution curves do exhibit the Landau fluctuation effect, Rossi [1965]. The testing methods A-E were conducted in the laboratory periodically to evaluate detector performance and to note any significant changes such as p.m. tube gain variation and other effects that would influence the proper operation of the instrument. Under satellite condition methods A-C have proved quite important in evaluating detector performance.

F. Reliability Tests

In order to insure reliable operation of the OSO-6 neutron experiment, the detector/electronics system was subjected to several reliability and performance tests. These tests, NASA [1966], were based on the requirements established by the OSO Project Office at the Goddard Space Flight Center (GSFC), Greenbelt, Maryland. They represented environmental variations under which the experiment was

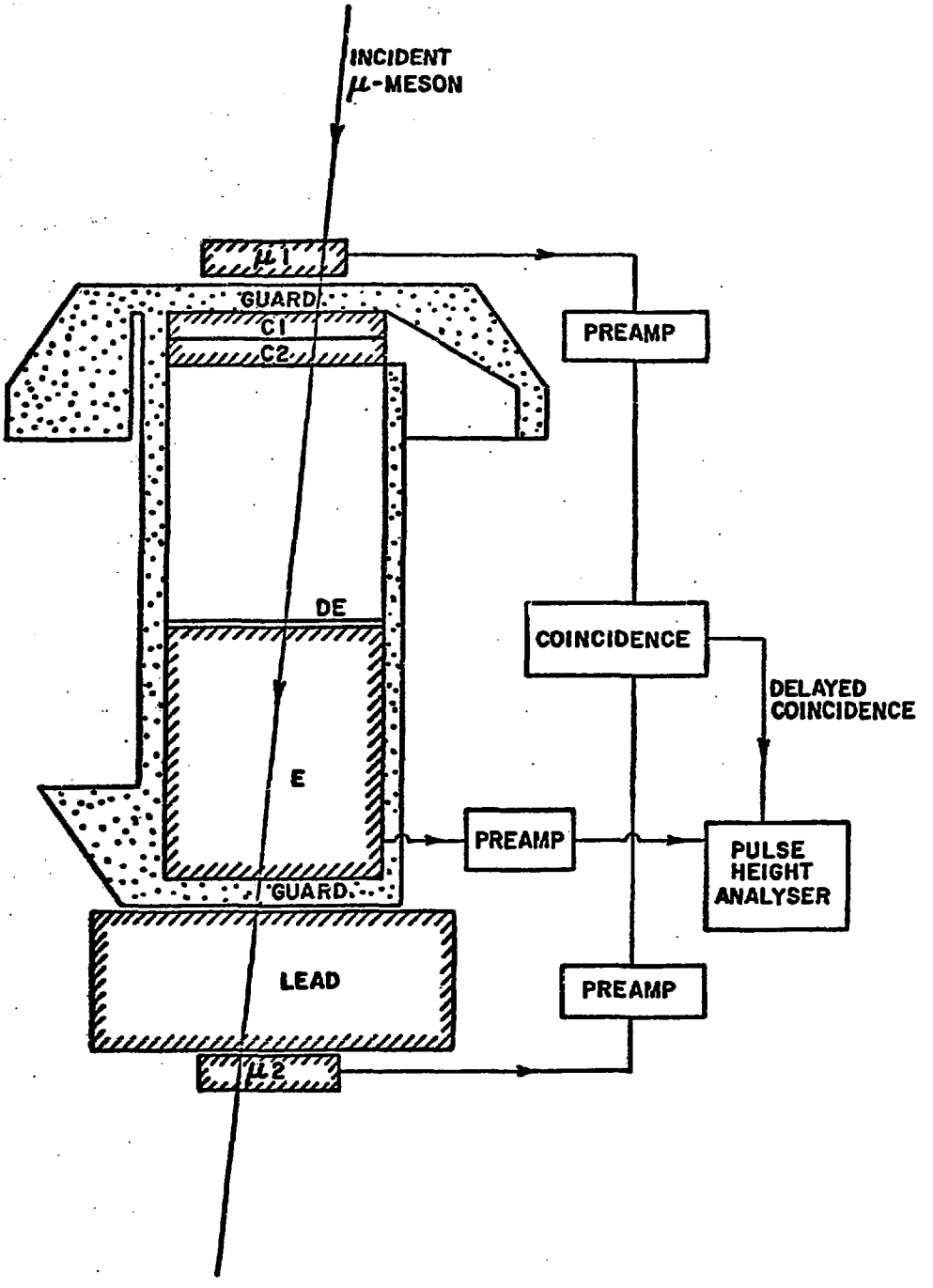

Fig. 20. Experimental Arrangement for Measurement of Cosmic Ray μ-Meson Energy Resolution Curves at Albuquerque, New Mexico.

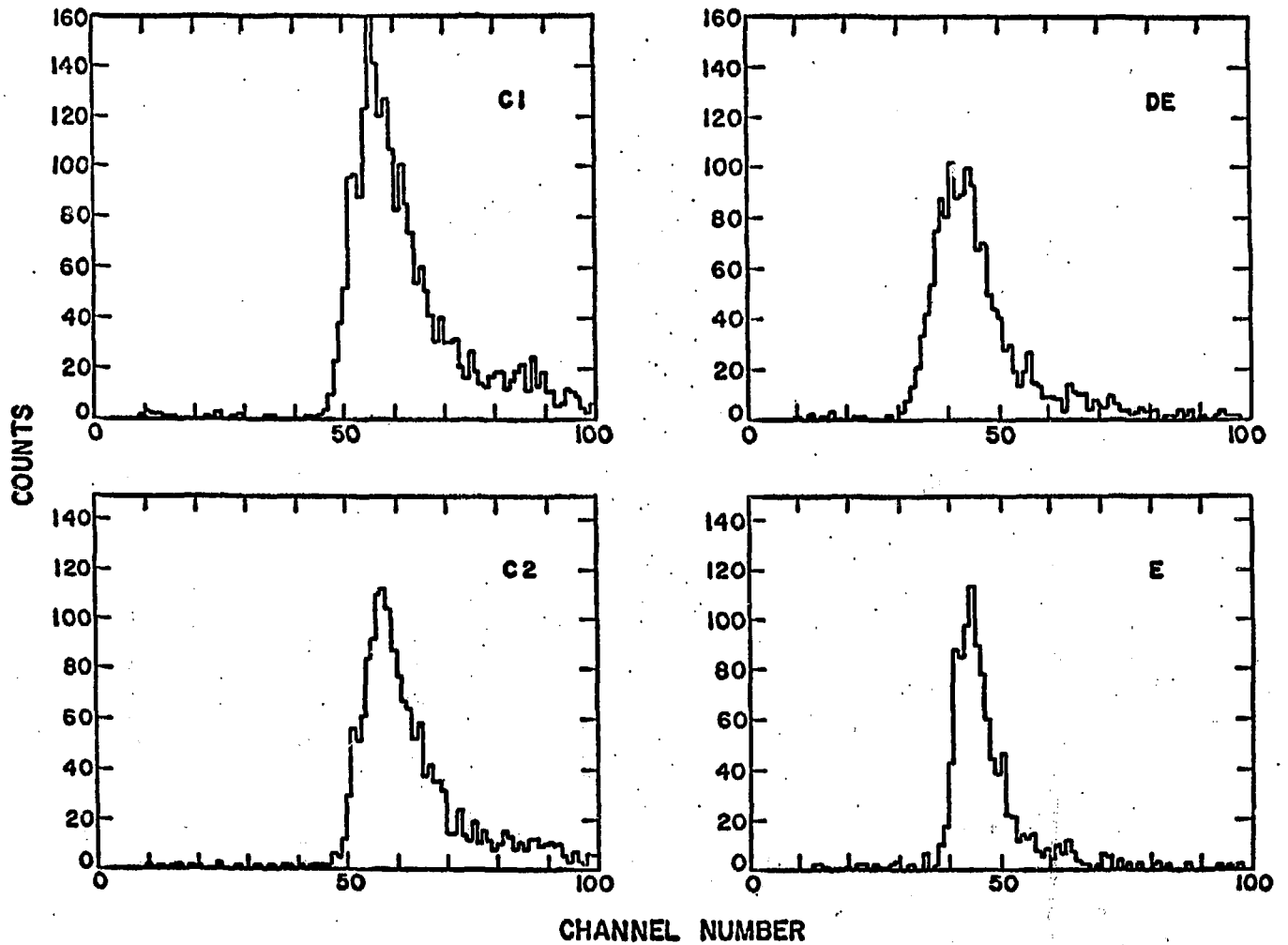

Fig. 21. Typical μ-Meson Energy Resolution Runs for the Flight Model Taken at Albuquerque, New Mexico.

expected to operate during the actual flight of the spacecraft. The principle tests were:

1. Interface.
2. Vibration.
3. Thermal Vacuum.
4. Interference.

In each of these tests the neutron instrument was electrically connected to a "spacecraft simulator" and, also, the experiment was operated using the cosmic ray neutron flux as observed at Boulder, Colorado.

The interface test was made to determine if the electrical interface between the main spacecraft and the experiment was satisfactory. During the test the various electrical parameters available from the spacecraft (for example, magnitude of the supply voltage) were varied to determine their effect on the performance of the instrument.

In the vibration test the experimental package was mounted on a "vibration-table" and was subjected to sinusoidal (10-2000 cps) and random vibrations inducing accelerations up to a peak value of 18 g in the thrust axis. The experiment was checked for normal operation using the calibrate cycle before and after each test.

In the thermal-vacuum test the experiment was placed inside a thermal-vacuum chamber. The latter was evacuated to a pressure of $\approx 10^{-6}$ mm of Hg and the chamber temperature was varied from 0°C to 40°C. Under these conditions the experiment was tested for normal operation. Higher pulse heights were observed at the lower temperature as expected since the conversion efficiency for the scintillator increases with decrease of temperature. Since temperature sensors

were included in the instrument, correction for this effect could easily be accomplished after launch.

The interference test was designed to determine if the presence or operation of other experiments on the spacecraft or the operation of the spacecraft system itself affected the performance of the neutron experiment. The experiment was operated continuously while the other experiments or the spacecraft systems were turned on and off one by one and the neutron experimental data was examined for possible interference. This also gave us some experience on the use of the error correction system. See NASA [1966] for a complete listing of the various tests required to space qualify the neutron instrument. The above tests were conducted at BBRC facilities of Boulder, Colorado, and were considered as "flight acceptance tests." Appendix I gives some of the environmental conditions for qualification and acceptance testing.

Further effort should have been made in devising a method for adjusting the gains of the various photomultiplier tubes in a satellite environment. A factor of two reduction in the gain of the energy counter photomultiplier tube did occur after launch. A set of possible reasons which could have caused this condition are:

1. Gain change in the photomultiplier tube.
2. Loss of optical coupling at the p.m. tube/light-pipe interface.
3. Damage to energy counter (crazing, cracks, etc.).
4. Electronic problems in the "E" channel.

Since the energy light diode was positioned near the energy light pipe-photomultiplier tube interface, the calibration data could

only reveal gain changes in the light pipe-p.m. tube-electronics system.

Because of the location of the light diode it was impossible to test for problems in the E counter or at the light pipe-E counter interface. The light diode was previously positioned at a location in the E counter such that a test of the E counter, the light pipe-E counter interface, the light pipe and the light pipe-p.m. tube interface seemed possible; however, the light which entered the E counter so dispersed that the intensity at the photo-cathode was too small to conduct a proper test. From previous experience the factor of two in reduction of gain does suggest loss of optical coupling, probably at the E counter-light pipe interface.

III. RESPONSE CHARACTERISTICS

A. Dynamic Range and Linearity of Response

Although the principal objective of the OSO-6 neutron experiment was to measure high energy neutrons, it was recognized that the anticipated low neutral event rate would waste much of the available telemetry readout time. Therefore a method was devised for recording charged particle events. It would have been desirable to have been able to measure neutron fluxes in such high radiation environments as in the South Atlantic anomaly.

To test the dynamic range and linearity of the OSO neutron electronics experiment, artificial coincident pulses were fed from a five output pulser with variable delay. The linearity of the p.m. tubes and light collection efficiency of the various scintillation counters were measured by pulsing in coincidence the light diodes which were embedded in or near each of the counters. Light from the solid-state diodes passed through the scintillator volume, the light-pipe, and into the p.m. tube cathode except for the E counter. Assuming that the spectral distribution of the light diode was constant and that the diode was stable, this test revealed changes in optical characteristics (absorption, loss of optical coupling, crazing, cracks) of the scintillator/light pipe configuration and changes in the performance of the p.m. tube. Since it was not possible to provide an output from the light pulsers that was as fast as the normal scintillator pulses, nonlinearity effects, which depend on the instantaneous

photomultiplier anode current, could not be faithfully simulated. The dynamic range of the scintillation counter system was tested by using cosmic ray neutrons since an artificial neutron beam was not available. A computer program was written to evaluate and classify neutron, gamma ray, and charged particle data. Much of the program consisted in the classification of the neutron data; that is, whether an event was due to a neutron that was incident from the front or rear side of the detector or other neutron classifications which are listed in Table 4.

B. Factors Contributing to Uniform Response and Accuracy

A scintillation counter is defined to have a uniform response if the electric charge collected at the p.m. tube anode is proportional to the light emitted in scintillation and independent of the position at which the emission took place.

Factors which influence the uniformity are:

1. Type of wall (diffusing, transparent, reflecting), shape of counter and position in which the p.m. tubes are placed.
2. Absorption of walls and the scintillator.
3. Non-uniformity of photo sensitive surfaces.

In a transparent-walled counter, one part of the light emitted in scintillation remains entrapped and another part escapes. In order to get uniform collection, and leaving out for the moment the question of absorption, it is necessary for the percentage of entrapped light to be independent of the position at which scintillation takes place. Now, spherically, Schrcliff and Jones [1948], and cylindrically, Brini et al. [1954], shaped counters do not satisfy such a condition. The one

geometrical shape which realizes uniform entrapping is that of a parallelepiped, Schrcliff and Jones [1948], Gillette [1950]. Results from Schrcliff and Jones [1948] are shown in Figure 22 where the trapping fraction F versus the index of refraction n is plotted for different scintillator geometries. Total light collection is due to the following contributions:

1. Fraction of light which arrives at the p.m. tube directly from the point of scintillation.
2. Fraction of light which is trapped in the counter by total reflection, and which partly reaches the p.m. tube.

Results (Table 6) of a calculation for the second contribution done by Brini et al. [1954] indicate that the percentage of trapped light for different distances in a cylindrical scintillator is an increasing function of the distance d where d is scintillation site relative to the center of the disc and r = radius of disc.

TABLE 6

PERCENTAGE OF TRAPPED LIGHT AS A FUNCTION OF SCINTILLATOR GEOMETRY

k=d/r	0	0.33	0.66	0.834
0/0	7.9	12	28	38

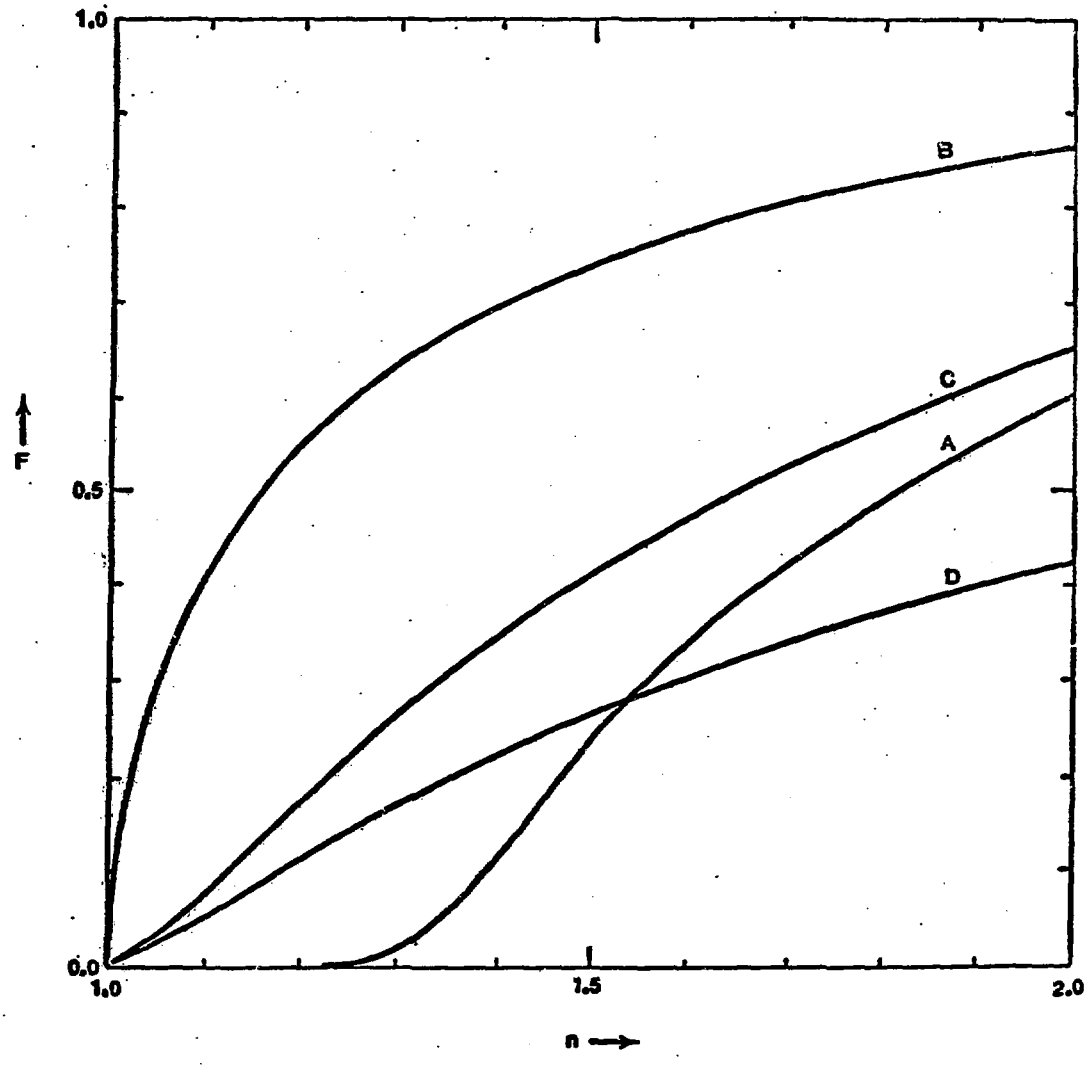

Fig. 22. The Trapping Fraction F Versus the Index of Refraction n for (A) Rectangular Parallelepiped, (B) Infinite Plane Parallel Slab, (C) Sphere with Homogeneous Production of Light, (D) Sphere with Inhomogeneous Production of Light.

C. Response to Neutrons

A common method of detecting and measuring neutron fluxes involves the observation of proton recoils from neutron-proton elastic scattering. The energy of the proton recoil is related to incident neutron energy through the nonrelativistic expression $E_p = E_n \cos^2\psi$ or through the relativistic expression $E_p = E_n \cos^2\psi/(1+E_n \sin^2\psi/2m_nc^2)$ where ψ is the scattering angle. Typically an experiment configuration, Siegel [1958], may consist of a hydrogenous radiator (polyethylene) and a scintillation or proportional counter telescope, or one may construct a detector (radiator-counter) in which the hydrogenous substance (e.g., Pilot B) where the recoil protons are produced is part of the sensitive volume itself, instead of being physically separated from it as in the recoil telescope detector. Qualitatively, one may state that the recoil telescope is characterized by good energy resolution and poor efficiency, while the radiator-counter has poor energy resolution and good efficiency.

A mechanism that is considered when discussing nucleon-nucleon scattering at high energies is the process of charge exchange. Figure 23 indicates that for a neutron energy of 14 Mev the differential cross-section is practically a constant. At higher energies the differential cross-sectior exhibits a minimum around 90°. This minimum becomes more and more pronounced as the neutron energy increases. The experimental points lie on curves that do not appear to be perfectly symmetric with respect to $\theta^* = \pi/2$. The asymmetries, however, are not outside of the experimental errors. With regard to these errors one should note that the measurements become more and more

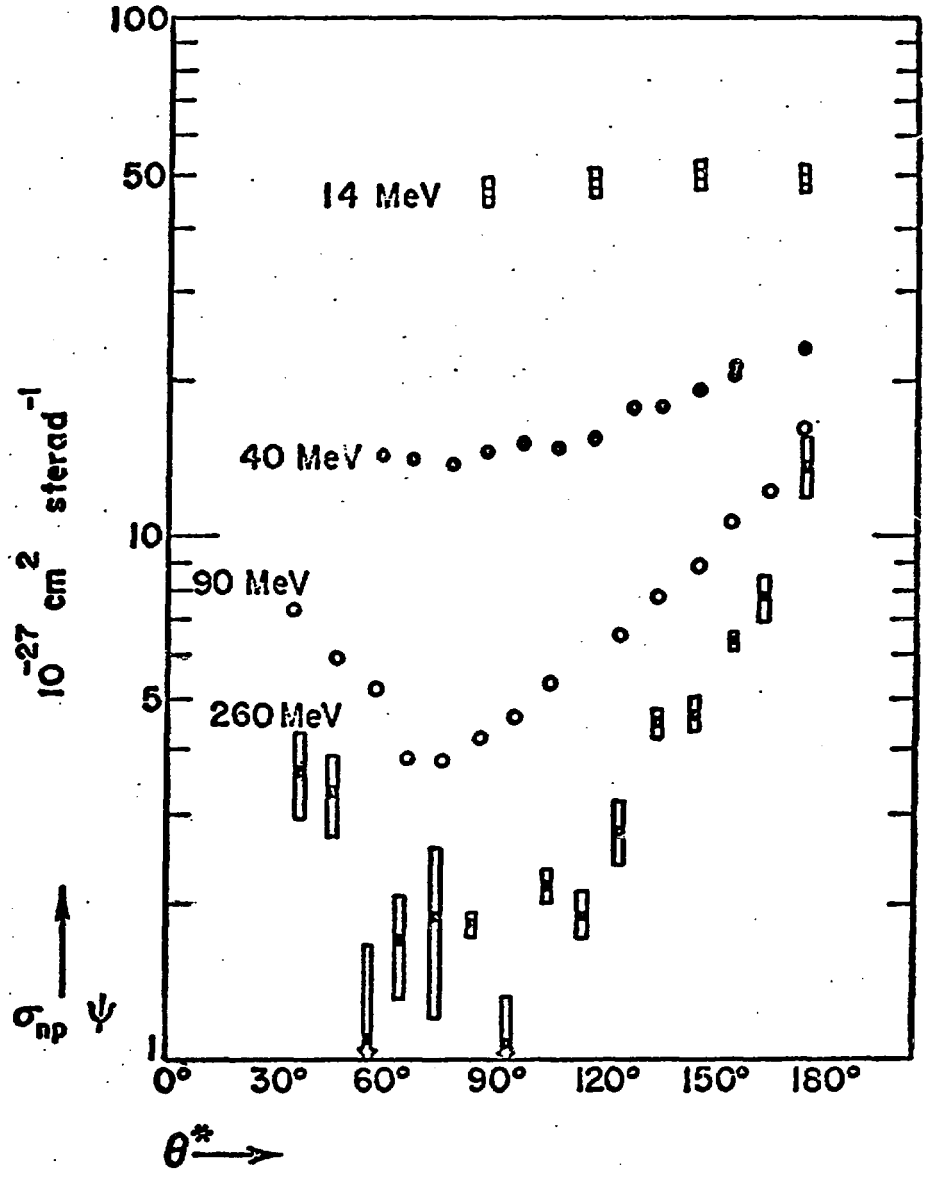

Fig. 23. The Differential Cross Section for n-p Scattering $\sigma_{np}\ \chi(\theta^*)$, in the Center-of-Mass System at Various Neutron Energies. See Rossi [1965].

difficult as the angle θ^* decreases. The reason is that as θ^* approaches zero (i.e., as θ_p approaches $\pi/2$) the energy of the recoil proton approaches zero.

The peak of the differential cross-section at $\theta^* = \pi$ signifies, physically, that there is a large probability for collisions in which protons are ejected in approximately the same direction and with approximately the same energy as the incident neutrons. Intuitively, one may describe this phenomenon as a charge exchange between a neutron in flight and a proton at rest. Indeed the fact that the cross-section is greater at $\theta^* = \pi$ than at $\theta^* = \pi/2$ is considered strong evidence for the existence of the so-called exchange forces between protons and neutrons. When the center of mass angular distribution, with a minimum at 90°, is transformed to the laboratory frame of reference, the result is an angular distribution peaked in the forward direction somewhat more strongly than a $\cos\theta$ dependence, with a secondary "hump" at large angles due to the backward recoils. Although the importance of the exchange phenomenon varies with energy, the overall effect is to sharpen the intrinsic directionality of the recoil process. The efficiency curves in Figure 26 were calculated with the use of the experimental cross sections at each energy.

D. Response to Gamma Rays

The detector is sensitive to high energy gamma rays. In the field of an atomic nucleus but also to some degree in the field of an atomic electron, a gamma ray may be totally absorbed and a positron-negatron pair emitted. A minimum incident gamma-ray energy of

$h\nu = 2m_o c^2 = 1.02$ MeV is required for pair production in the field of a nucleus, and a minimum of $h\nu = 4m_o c^2 = 2.04$ MeV in the field of an atomic electron.

The atomic cross section for nuclear pair production increases with Z^2 (reduced somewhat at very large gamma-ray energies by electron screening of the nuclear field) and with the gamma-ray energy $h\nu$. The kinetic energies of the positron and the negatron pair electrons are continuously distributed, each from a minimum of zero up to a maximum of $h\nu - 2m_o c^2$.

Using the cross-section table of Storm and Israel [1970], the probability of interaction for 100 meV gamma ray in 2 gm/cm^2 (10 gm/cm^2) of Pilot B is 1.46% (7.1%), respectively. Since the data due to gamma-ray events tend to have low values of energy and dE/dx, separation of gamma-ray and neutron data is possible (see Figure 17).

E. Response to Proton Recoils and Charged Particles

This detector which uses scintillating plastic does not directly measure the energy of the incident neutron. Assuming neutron total cross sections of Bowen et al. [1949], the probability of interaction in 2 gm/cm^2 (10 gm/cm^2) of Pilot B (C1 + C2), (E), is around 5% (23%), respectively.

A recoil proton must first be produced as a result of the n-p scattering process. It is the interaction of this charged recoil proton with the scintillating matter that allows us to measure neutron fluxes. The recoil proton in moving through matter will lose energy as a consequence of collisions with atomic electrons. The greatest part of the energy loss occurs in these collisions as compared to

nuclear collisions. The deflection of the particle from its incident direction results from essentially elastic collisions with atomic nuclei. The scattering is confined to rather small angles so that the proton keeps a more or less straight-line path while losing energy until it nears the end of its range. Near the end of its range large scattering can occur. Since the energy lost by a particle in passing through matter is the result of a large number of independent events, the ionization process is a statistical phenomenon, i.e., no unique value for the energy loss obtains. It has been shown that the resultant energy-loss distribution is negatively skewed—the high energy-loss tail being due to those collisions in which a large amount of energy is transferred to the target electron in a single collision. Thus it is important to recognize the difference between the mean energy loss and the most-probable energy loss. The mean energy loss is related to the case of close collisions where one can treat the atomic electrons as free particles if the limiting electron energy is sufficiently large and the corresponding impact parameter sufficiently small. On the other hand, the most-probable energy loss is related to distant collisions where the particle velocity is relativistic so that the density effect obtains. The close and distant collisions refer to impact parameter distances.

An energetic heavy charged particle such as a proton, in its passage through matter, produces the ionization contributing to its energy loss in two different ways. In the primary collision with the electrons in an atom, the most probable of the ionizing collisions are those in which a relatively slow secondary electron is ejected with kinetic energy smaller than the ionization potential. A small fraction

of the ionizing collisions, however, produce secondary electrons of relatively high energy, the maximum energy being 4 (m/M)E corresponding to a maximum velocity of twice the velocity of the incident heavy particle where M (m) is the incident particle (electron) mass, respectively.

The secondary high energy electrons (delta rays) can go on to produce further ionization in the atoms of the stopping material, leading to a secondary ionization. The total ionization that we measure with a scintillator is the sum of the primary and secondary ionizations. In using thin absorbers a single collision can possibly result in an appreciable transfer of energy with the formation of delta rays, which can leave the counter, and this will result in higher fluctuations. The range of a proton is the mean depth of penetration measured along a straight line from the point at which the protons enter an absorbing medium to the point where the proton has stopped. Because of the statistical fluctuations in energy losses protons with the same incident energy do not have exactly the same range in matter. This phenomenon (straggling) can be represented by a range distribution where one can discuss for example an average and a most-probable range.

The scintillator characteristics, its emission spectrum, efficiency, and decay time, are determined by the molecular properties of its components, and by the complex sequence of events that form the scintillation process. A scintillator usually consists of one solvent component, and one or more solute components. The incident ionizing proton dissipates its energy in producing ionized and excited molecules of the solvent component and free electrons. Direct ionization and

excitation of the solute is negligible. The ionized molecules of the solvent component may (1) recombine with free electrons, producing further excited molecules of the solvent, or (2) be permanently damaged, or form metastable radicals which subsequently recombine with other molecules or radicals to produce new molecular species, e.g., dimers. These damaged or impurity molecules can act as quenching agents, so that the scintillation efficiency deteriorates on prolonged irradiation. On the other hand, the free electrons or delta rays may (3) produce further ionization and excitation, (4) recombine with ionized molecules or radicals, or (5) be trapped at an impurity or lattice defect.

Fluorescence of the solvent followed by radiative transfer to the solute is a significant process, but the major fraction of the energy, in the more efficient systems, is transferred from the solvent to the solute by a non-radiative process. The entire scintillation process involves some 29 principal events or transition probabilities. The conversion efficiency of any organic scintillator is usually estimated by comparing its light yield with that of anthracene or stilbene. The average value of $N_{anthracene} = 0.04$ corresponds to the expenditure of approximately 70 eV for the formation of one photon with $\lambda = 4000$ Å - 4100 Å (wavelength near the maximum for a photomultiplier tube with S-11 spectral response).

The decrease in the conversion efficiency with the increase in specific ionization dE/dx leads to a breakdown of the proportionality between the light scintillation and the energy lost by the particle during passage through the scintillator. The experimental dependence

of the light yield dE_s/dx on dE/dx is adequately described by the Birks [1967] formula,

$$\frac{dE_s}{dx} = \frac{A\ dE/dx}{1 + kB\ dE/dx}\ , \tag{8}$$

where A, k, and B are constant parameters. This dependence turns out to be approximately identical for all charged particles except for particles with $Z > 1$ in the region where dE/dx equals 50-100 MeV/gm cm^2. Greater light yields obtain because of the $dE/dx \approx Z^2$ effect. The same value of dE/dx can be reached by both protons and, for example, alpha particles by allowing the α rays to travel at a higher velocity than the protons. Using the "exciton theory" introduced by Bowen et al. [1949], let us examine the physical significance of formula (8). On this theory of the energy transfer processes in organic systems, the electronic energy excited by the incident radiation is transferred from molecule to molecule within the scintillator, until it is captured by a single molecule, which then either fluoresces or quenches the "exciton," depending on the nature of the molecule.

The passage of the ionizing particle through the scintillator produces a local concentration of damaged or ionized molecules along its path. These damaged molecules act as quenching agents for the "excitons" produced by the ionizing particle. The number of "excitons" produced per unit path length is proportional to the specific energy loss, say A dE/dx. The local concentration of damaged molecules at any point on the particle track is also proportioned to the specific energy loss, say B dE/dr molecules per undamaged molecule. Hence, if the "exciton" capture probability of a damaged molecule, relative to

an undamaged molecule, is k, the specific fluorescence obtains

$$\frac{dE_s}{dx} = \frac{A\ dE/dx}{1 + kB\ dE/dx} \cdot \tag{9}$$

At low values of dE/dx, (9) becomes $dE_s/dx = AdE/dx$, and at high values of dE/dx, (9) becomes $dE_s/dx = A/kB$ = constant, in agreement with the observed behavior.

Figure 24 shows the calculated light output for NE 102 plastic scintillator as a function of particle energy. The response to a 160 MeV electron on this scale is 1.16, Gooding and Pugh [1960]. Wright [1953] attributing the light output of organic scintillators to a different mechanism obtains

$$\frac{dL}{dx} \propto \text{LOG}\ (1 + a\ \frac{dE}{dx}) \ , \tag{10}$$

where a is a constant. For computational convenience Gooding and Pugh have chosen Wright's formula, although both Birk's and Wright's formulas agree with experimental data.

Another consideration in scintillation work resides in the fact that fluctuations in ionization losses can occur when observing relativistic charged particles or when using "thin" counters. An approximate expression for this effect goes as β/x where β is the particle velocity and x is the counter thickness in gm/cm^2 (Figure 25). Since β in our case is approximately 0.55 (186 MeV), we will not have to consider the density effect.

The reason we observe fluctuations in energy loss when using "thin" absorbers is that there exists a small probability of proton-electron collisions which result in relatively large random statistical

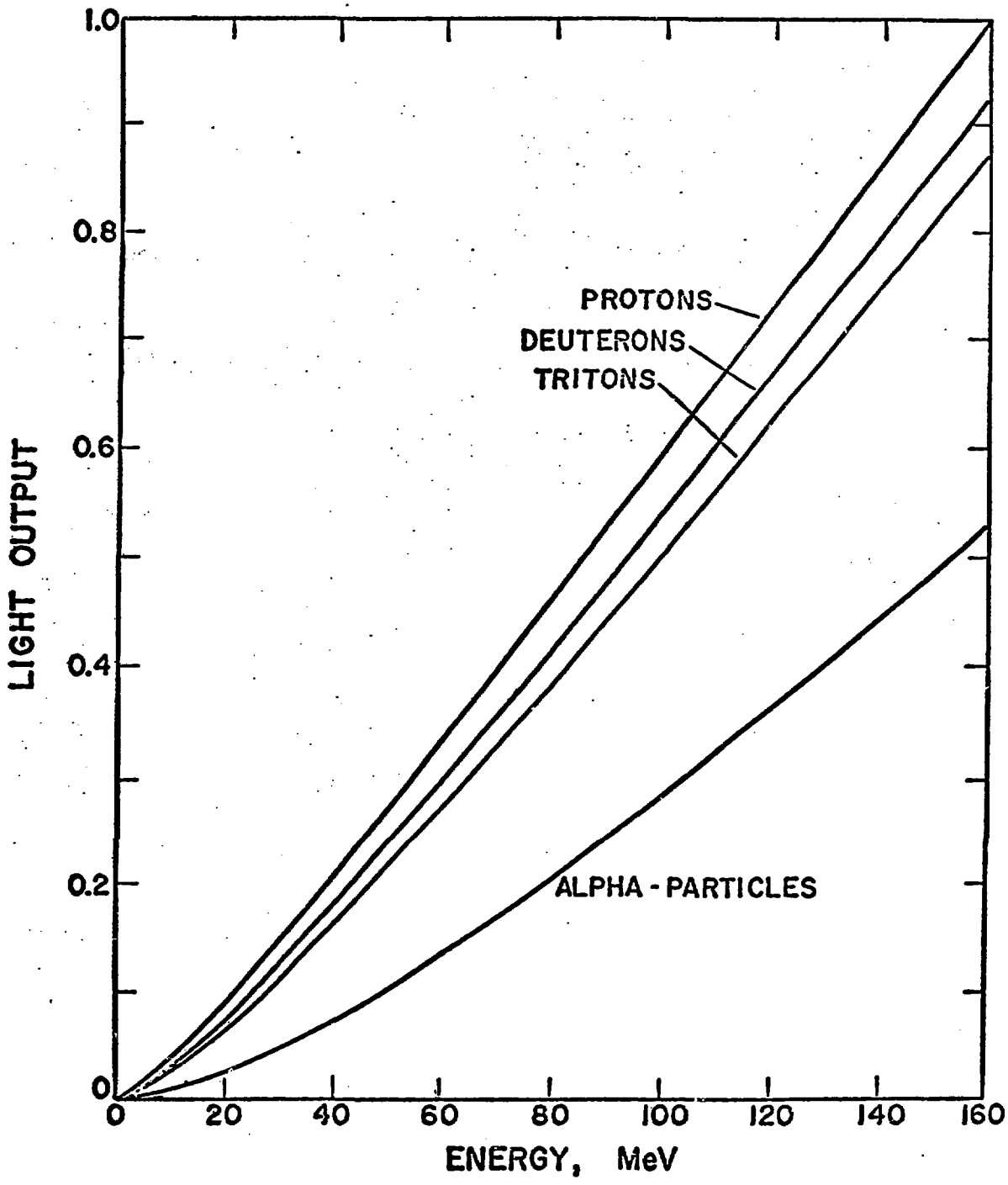

Fig. 24. The Calculated Response of NE 102 to Protons, Deuterons, Tritons, and Alpha Particles. The Response to a 160 MeV Electron on this Scale would be 1.16.

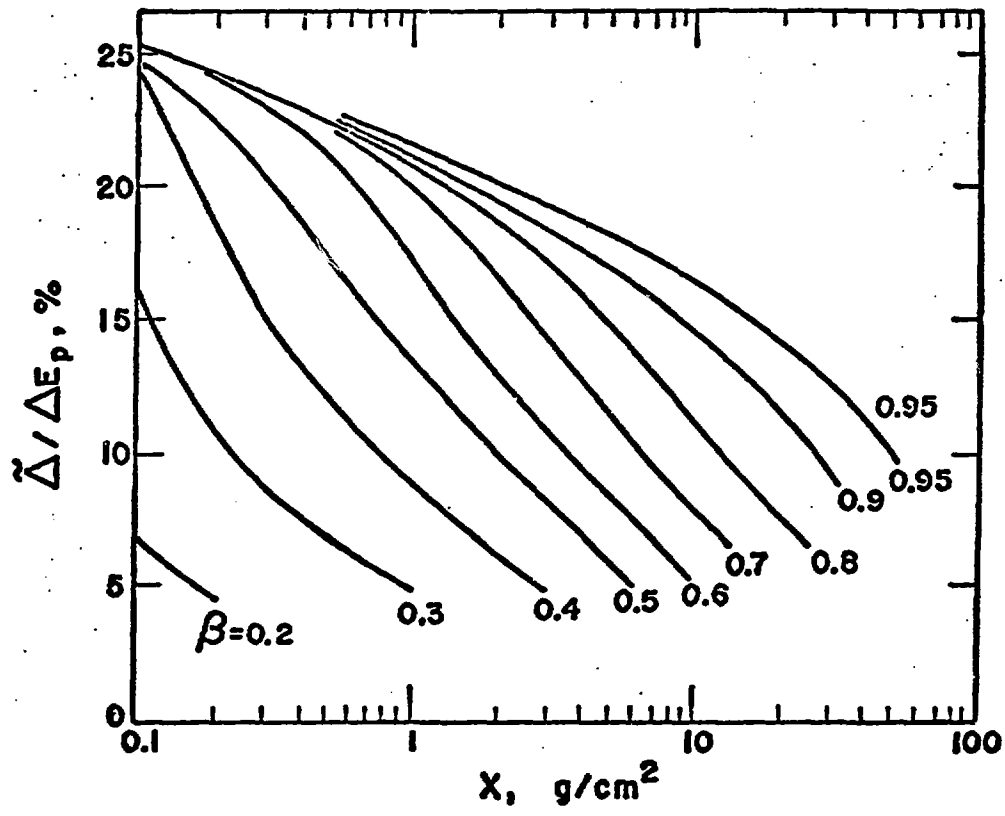

Fig. 25. Half-Width of the Spectral Ionization Loss as a Function of Thickness for Organic Scintillators and for Various Velocities of a Singly Charged Particle.

variation in their collisions. Since an exhaustive review on the theory of energy-loss fluctuations has been presented elsewhere, Fano [1963], I will only examine some of the main features of the theory.

The most-probable energy loss, which corresponds to the peak of the measured experimental distribution, can be calculated from the theory of Landau [1944]. Parameters of the resultant characteristic energy-loss distribution which are of interest are (a) its shape, (b) the average energy loss E_a, (c) the most-probable energy loss E_p, and (d) the full width at half maximum of the distribution, Δ_{fw}.

The most significant observation is that the parameters β and K uniquely define a spectrum for a given particle type and energy, and for a given material. The parameter K is defined by

$$K = \xi/\epsilon_{max} \ , \tag{11}$$

where

$$\xi = \frac{2\pi e^4 z^2 N x}{mv^2} \frac{Z}{A} \ , \tag{12}$$

where z is the charge of the incident particle, and N the number of atoms per cubic centimeter of the absorber material. The quantity ϵ_{max} is the maximum possible energy transfer in a heavy particle-electron collision which is given approximately by

$$\epsilon_{max} = 2mv^2/(1-\beta^2) \ , \tag{13}$$

when

$$Mc^2/(1-\beta^2) \ll M^2c^2/m \ , \tag{14}$$

where M is the heavy-particle mass. Substituting (12) and (13) into (11) we get

$$K = Ax/\beta^2\varepsilon_{max} \ , \tag{15}$$

where $A = 0.30058\ z^2 \frac{Z}{A_o}\ mc^2$. Here K may be thought of as a measure of the ratio of the total energy loss to the maximum possible energy loss in a single collision, i.e., an estimate of the number of large energy-loss collisions suffered by the particle in passage through the medium.

There are three basis cases to be considered.

(a) $K > 1$: Here the number of collisions in each energy-loss interval is large and the effect of fluctuations negligible. The distribution is Gaussian with a width or variance, Bohr [1915], Seltzer and Berger [1965],

$$\sigma^2 = \xi\ \varepsilon_{max}\ (1 - \frac{\beta^2}{2}) \ , \tag{16}$$

and a half width of 1.177σ. To get the percent fluctuation one has to solve for the most-probable energy loss Δ_p, Seltzer and Berger [1965],

$$\Delta_p = \bar{\Delta} + (t_p - a^2)\eta \ , \tag{17}$$

where the mean energy loss in a short path length x (gm/cm^2) is given by

$$\bar{\Delta} = 0.30058\ \frac{mc^2}{\beta^2}\ \frac{Z}{A}\ x \left[\text{Log}\ \frac{2mc^2\beta^2\varepsilon_{max}}{I^2(1-\beta^2)} - 2\beta^2 - \frac{2C}{Z} - \delta \right] , \tag{18}$$

where Z, A, and I are, respectively, the atomic number, atomic weight, and mean excitation energy of the medium, 2C/Z is a shell correction, and δ is the density effect correction. Other parameters in the Δ_p equation are

$$t_p: \text{ value of t for which } \frac{dv(t)}{dt}/v(t) = -a \ , \tag{19}$$

$$v(t) = \frac{1}{\sqrt{\pi}} \int_0^\infty \cos(ut + \frac{u^3}{3}) du \text{ (Airey's function)} \ , \tag{20}$$

$$a = (1 - \frac{\beta^2}{2}) \left[\frac{2K}{(1 - 2/3\beta^2)^2} \right]^{1/3} \ , \tag{21}$$

$$\eta = \xi \left[\frac{(2K)^2}{(1 - 2/3\beta^2)} \right]^{1/3} \ , \tag{22}$$

and

$$K = (0.30058 \frac{mc^2}{\beta^2} \frac{Z}{A} x)/\epsilon_{max} \ . \tag{23}$$

(b) $K \leqslant 0.01$: This is the opposite case where the number of collisions in each energy-loss interval is small. This problem has been solved by Landau [1944]. The resulting distribution is asymmetric with a long high-energy tail and a broad peak. The value of full width at half maximum is about 30% of Δ_p or 3.98 ξ, where $\xi = 0.30058 \frac{mc^2}{\beta^2} \frac{Z}{A} x$. Δ_p is significantly less than $\bar{\Delta}$.

(c) $0.01 < K < 1.0$: This intermediate region was first investigated by Symon [1948] who obtained a more general expression than Landau's for the probability distribution which he solved under the consitions,

$$M \gg m, \quad Mc^2 \leqslant T \leqslant 10\ Mc^2 \ , \tag{24}$$

where T is the kinetic energy of the incident particle. Thus he was able to link approximately the Gaussian and Landau regions. However, as pointed out by Skyrme [1967], the application of Symon's solution

to specific cases needs considerable manipulation and extrapolation of his published results.

The transport equation describing the energy-loss distribution has been more rigorously solved by Vavilov [1957]. His precise calculation uses integrals which have been tabulated by Seltzer and Berger [1965].

Energy-loss distribution of 37-MeV protons, in plastic scintillators and in argon-filled proportional counters, have been measured by Gooding and Eisberg [1957]. Symon and Vavilov distributions are in good agreement which predict the experimental results quite well.

If one solves for K in our case for 100 MeV protons and the 4 mm dE/dx counter in Pilot B, we get K = 0.788 which implies that case (c) should apply for the dE/dx counter. For C1 and C2 at 100 MeV, K = 1.97 implies use of case (a). However, for a 500-MeV muon in dE, K = 0.0028, case (b) applies and we would have to solve for the degree of skewness in the energy-loss distribution. As shown in the mu resolution runs, Figure 21, the skewness in the energy-loss distribution is indicated. Since a 500-MeV muon loses 0.158 MeV/gm/cm^2 and K = 0.0028, a 5-BeV proton would lose the same MeV/gm/cm^2. This would imply use of the Gaussian case (a) for C1 and C2 where half width $1.177\sigma = 1.177 \times 0.30058 \times \frac{Mc^2}{\beta^2} \frac{Z}{A} \times \varepsilon_{max} (1 - \frac{\beta^2}{2})$ can be calculated.

It would appear in principle that in analyzing the charged particle data one could plot dE/dx versus E as a function of particle type such as muon, proton, alpha components. Also, there exists a group of events which are proton recoils that have energies just outside the limits defined by the instrument. In an attempt to understand the energy resolution characteristics of C1, C2, dE, and E, the

following resolution curves depicted in Figure 21 were derived from cosmic-ray muons at Albuquerque, New Mexico. These resolution numbers which include effects from the counter, p.m. tube, and the electronics are 25.5%, 21.3%, 34.8%, and 20% for C1, C2, dE, and E, respectively. The E counter has a K = 19.7 at 100 MeV and here case (a) would be used. For C1 and C2 (E) FWHM = $2.35\sigma = 2.35\sqrt{\xi\, \varepsilon_{max}(1 - \frac{\beta^2}{2})} = .73(2.3)$ Mev respectively, for 100-MeV proton recoil. For dE/dx one could use the approach as outlined in Seltzer and Berger (1965). To test these theoretical numbers a proton beam would be required to generate experimental numbers. The above numbers relate only to fluctuations in ionization losses. Other experimental effects do contribute to the total energy resolution.

When a proton passes through the material (e.g., "E" counter) it can undergo nuclear interactions. The energy deposited in the counter will be less than that for protons which do not interact. Thus in stopping counters the proton can be considered as lost from the full energy peak if it undergoes a nuclear inelastic interaction. A consideration in the analysis of the neutron data might be to examine neutron events in the tail near the energy peak using similar calculated values for C1, C2, and dE. In other words, we may be losing neutron events in the analysis program due to nuclear inelastic interactions. We are currently processing neutron events which do not undergo this inelastic interaction. It would be interesting to look at neutron events in the tail of the energy spectrum.

F. Efficiency

Analytic calculations for the efficiency of a proton recoil telescopic detector are difficult to make in principle. The Monte Carlo method allows one to perform an approximate calculation of the efficiency which should shed some light on some design parameters for a detector. A Monte Carlo program, "Neutrex," was devised to calculate the efficiency of the detector for both forward and backward neutrons of different energies and directions. Let us suppose a neutron is incident on the sensitive area of the detector. The energy and the initial direction of the neutron is given. The point of entry, the point of possible collision with a proton, and the resultant trajectory of the proton recoil are selected at random. Numerous tests are applied to each proton recoil trajectory to define whether the proton stopped in the E counter (C1 or C2) for the forward (backward) case, respectively, or not. The latter condition has four classifications:

1. The proton recoil left the detector in forward (backward) direction for the forward (backward) case, respectively.
2. The proton recoil left the detector through the side.
3. The proton recoil passed completely through the total detector volume.
4. The proton recoil had an energy which was too low to produce enough light in the stopping counter to satisfy electronic threshold conditions.

The program also tabulates for the forward case the total number of collisions that occurred in C1 and C2. A typical number of trials necessary to produce proton recoil events which stop in the E counter

is around 40,000. Figures 26-28 and Table 7 give results of a calculation done by Conklin [1968]. The average absolute efficiency within angular acceptance angle of 29° (FWHM) is about (2.25±0.1135) $x10^{-4}$. The efficiency distributions tend to show large values for intermediate neutron energies and small incident angles. At higher incident energies low n-p total cross sections coupled with leakage of proton recoils from absorption volume (E counter) give low efficiency values.

G. Corrections

Since the Pilot B scintillation plastic has a hydrogen-to-carbon ratio of 1:1 we must consider inelastic, elastic, and quasi-elastic incident neutron interactions with the carbon nuclei. We can identify most of the inelastic interactions except for those events that have pulse height coordinates in C1, C2, dE, and E similar to the event resulting from a neutron incident from the rear side of the instrument. Events satisfying the latter condition are tagged as ambiguous backward.

The pulse height coordinates for the quasi-elastic case are indistinguishable from those of proton recoils from hydrogen. The above condition requires that an estimate be made in classifying proton recoils from the $^{12}C(n,p)^{12}B$ reaction and hydrogen. Very little experimental data seems to exist on the quasi-elastic $^{12}C(n,p)^{12}B$ reaction. Perhaps some n-p quasi-elastic work could be conducted at the LAMPF facility at Los Alamos, New Mexico. Their neutron beam has better energy resolution (0.1 peak energy spread) and intensity (100 times) than beams from comparable synchrocyclotrons. Furthermore, since Chalmers [1971]

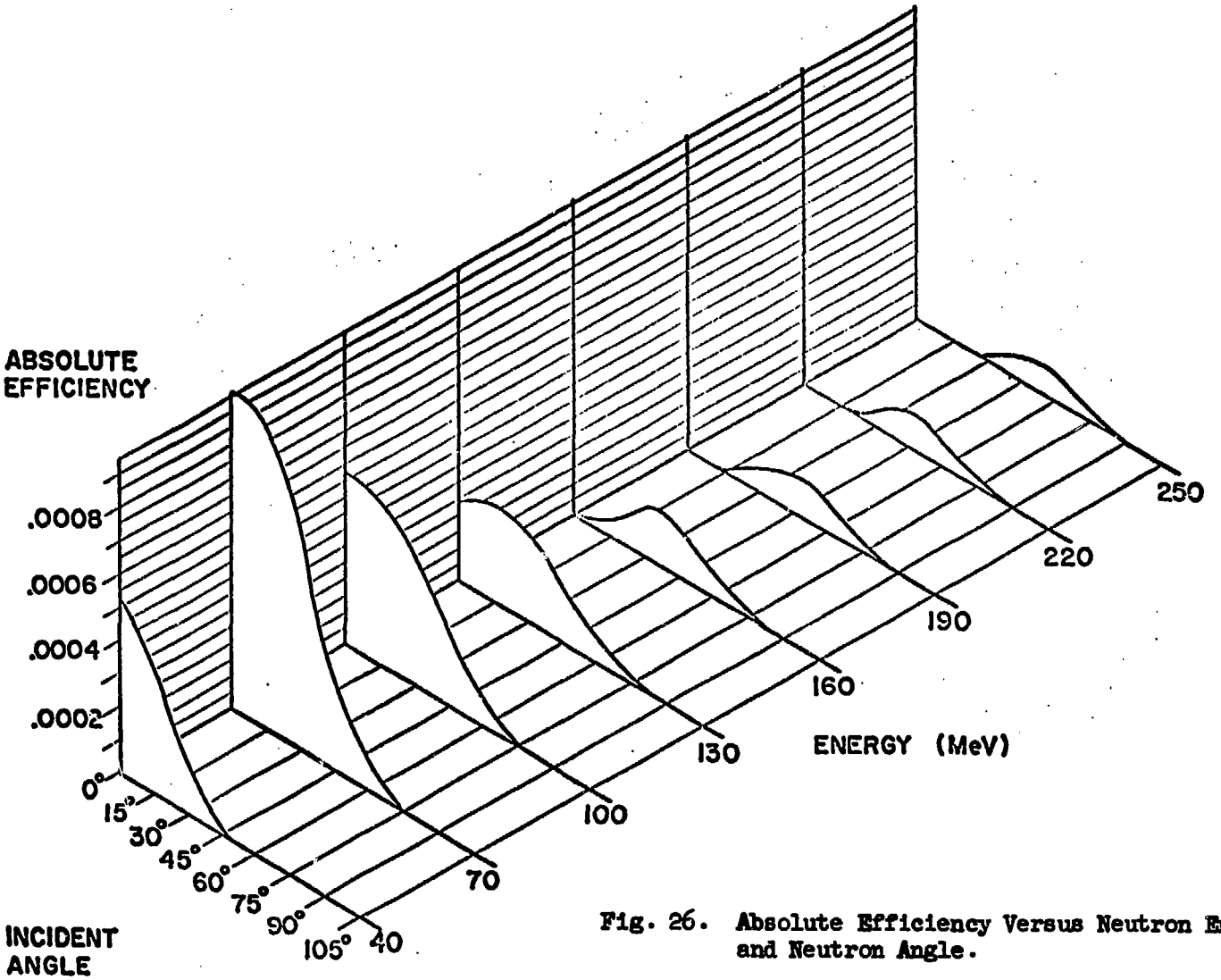

Fig. 26. Absolute Efficiency Versus Neutron Energy and Neutron Angle.

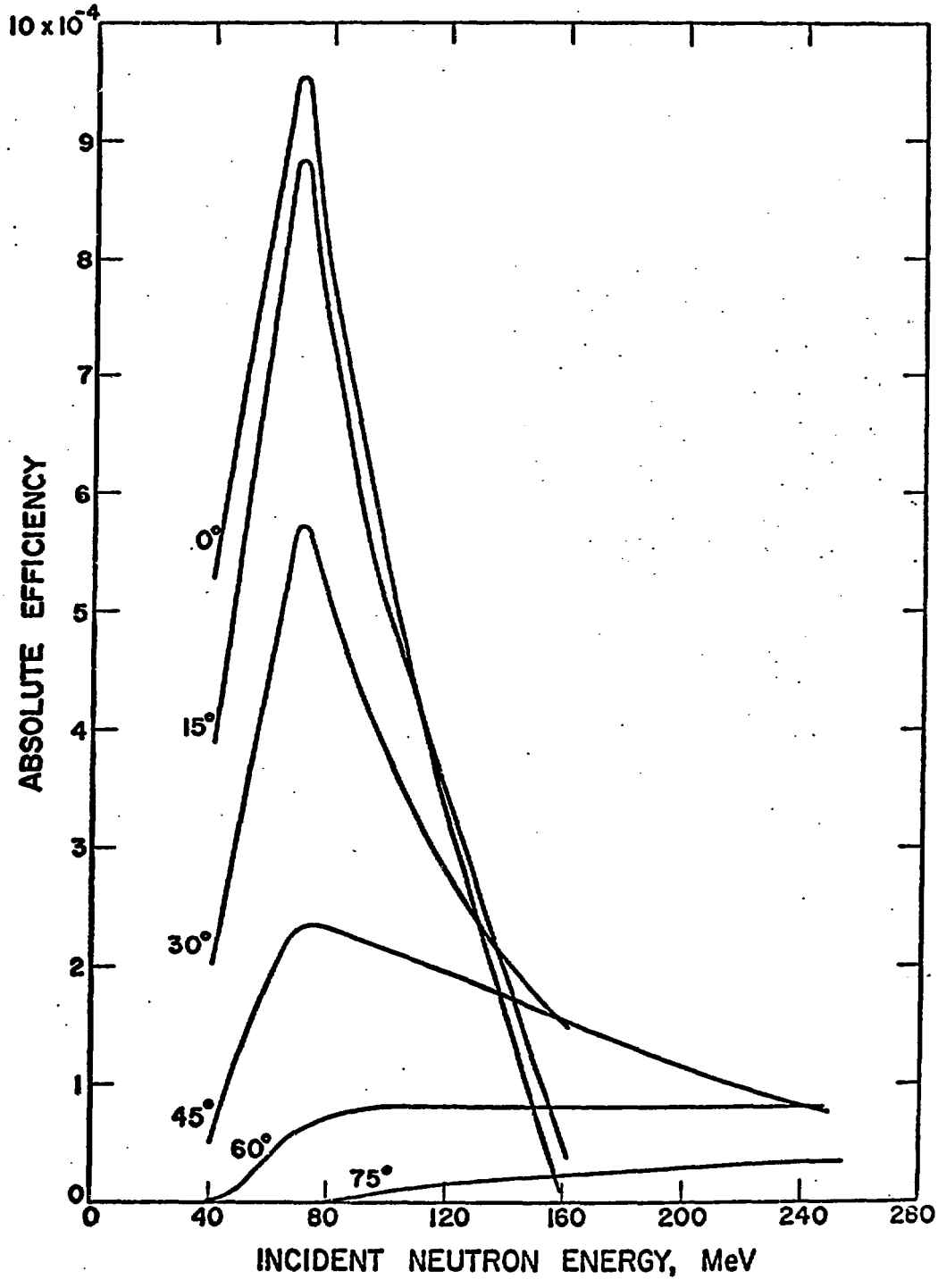

Fig. 27. Absolute Efficiency Versus Neutron Energy.

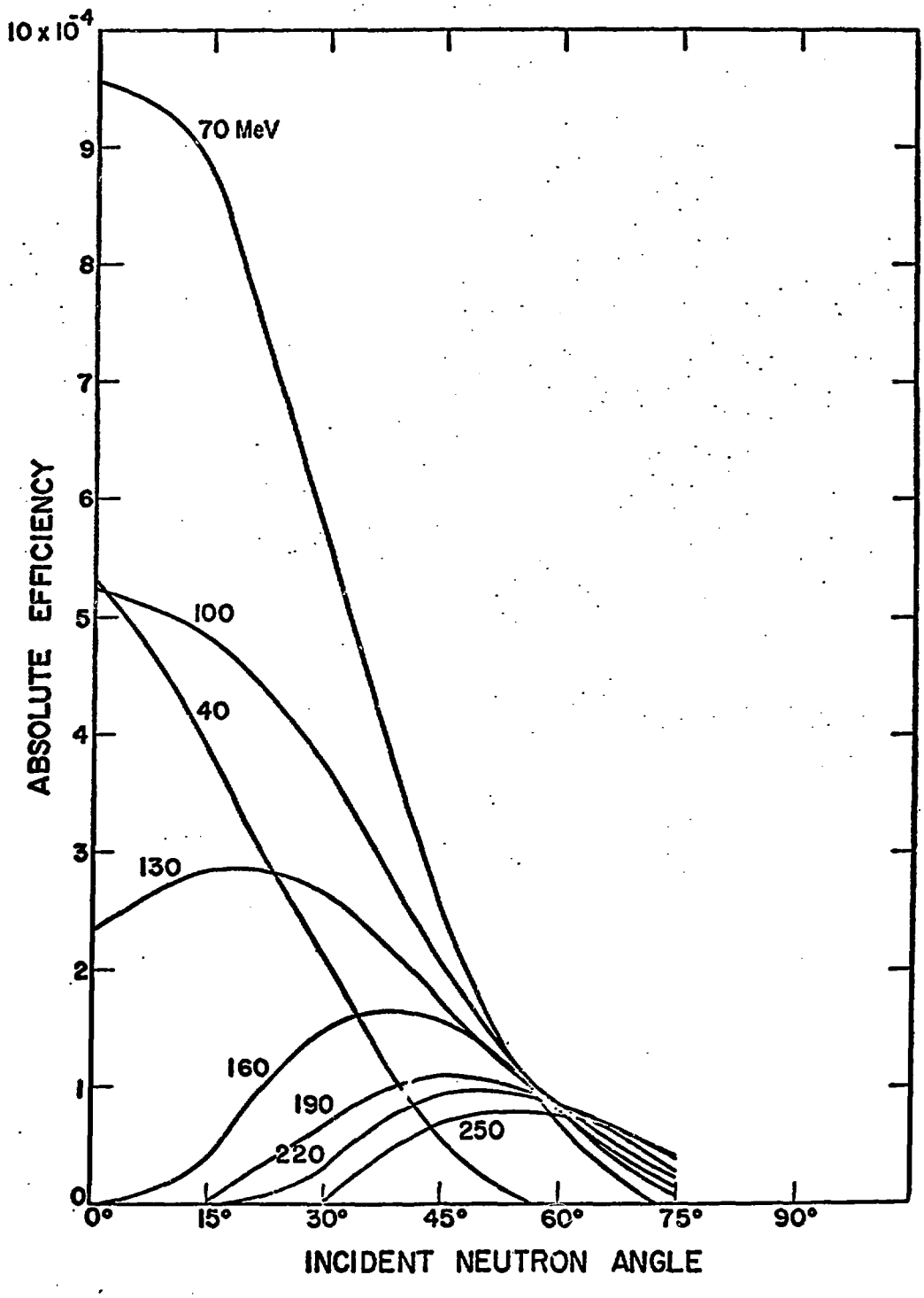

Fig. 28. Absolute Efficiency Versus Incident Neutron Angle.

TABLE 7

ABSOLUTE EFFICIENCY*

Energy in MeV \ Angle	0°	15°	30°	45°	60°	75°	90°
40	5.330	3.917	2.095	0.552	0.0687	0.0000	0.0000
70	9.525	8.842	5.7060	2.387	0.653	0.0663	0.0000
100	5.294	4.847	3.777	2.146	0.838	0.1418	0.0000
130	2.356	2.881	2.680	1.721	0.821	0.1817	0.0105
160	0.009	0.444	1.549	1.646	0.902	0.2851	0.0314
190	0.0000	0.004	0.708	1.243	0.888	0.3006	0.0515
220	0.0000	0.0000	0.351	0.952	0.827	0.3375	0.059
250	0.0000	0.0000	0.0186	0.729	0.799	0.3583	0.071

*All numbers times 10^{-4}.

had to use elastic data from Van Zyl et al. [1956], perhaps some LAMPF work could be devoted to the elastic reaction.

IV. THEORETICAL MODELS FOR NEUTRON PRODUCTION

An interesting phenomenon associated with solar activity is the solar flare; see Zirin [1966], Tanberg-Hansen [1966], de Jager [1965], Xanthakis [1967], Smith and Smith [1963], and Ortner and Maseland [1965]. Although these great eruptions produce effects throughout the entire solar system, some of which, such as the auroral borealis, may be observed even without instruments on the earth, they are essentially invisible to the unaided eye. This is because solar flares occur in the chromosphere and corona where the density is low, and they are usually transparent in white light. It is when they are viewed in certain isolated wavelengths of spectral lines that one can see the flare clearly. Solar flares normally occur in the neighborhood of sunspots and very often in pre-existing plages. To be observed in the H_α line, the temperature of the flare must not exceed 50,000°K, otherwise the atoms will be completely ionized. If the flare is observed on the limb of the sun where coronal radiation can also be observed, one finds that the flare is accompanied by a large increase in the density and temperature of the corona. The strong soft x-ray radiation in the region between 1 to 20 Å indicates that there is a large amount of extremely hot material directly above the chromospheric flare. Since the typical energy of the particles in the hot coronal region above the flare is several hundred eV, the predominant radiation is in the very short wavelength region (1-20 Å).

There is lacking at present a reasonable theory for predicting the appearance of solar flares. Normally a very large sunspot group, particularly a young one with a complex magnetic structure, will tend to be associated with flares. Furthermore, a region that has had many flares

will probably have many more develop. Finally, there is some evidence that one can find an increase in the density of the corona above a sunspot immediately preceding the flare. Solar flares are associated with magnetic phenomena. Only the magnetic field has high enough an energy density, $H^2/8\pi$, to produce the highly localized flares. It is interesting that on many occasions a region will have several isomorphic flares occurring in the same region, with the same configuration. Later in the discussion I will explore some of the details of a flare model, Wild [1962].

The detection at the earth of high energy solar flare particles suggested the possibility that detectable secondary particle and radiation fluxes might also be produced by nuclear interactions of these particles in the solar atmosphere. In particular, such interactions might occur both during the acceleration of flare particles and during the slowing down of those particles which do not escape from the magnetic fields of the flare region. Since the solar flare particles observed at the earth consist mainly of protons and alpha particles, the most probably directly detectable secondary products would be neutrons, positrons, gamma rays, and the light isotopes, deuterium, tritium, and helium-3. The detection of neutrons will be discussed in this work.

Hess [1963] has suggested there are probably five different solar neutron sources from the following processes. First there are the solar albedo neutrons produced by galactic cosmic ray protons interacting with helium and hydrogen. Since the number density of helium is small, this provides a weak source of solar neutrons, and since the threshold for the reaction $^1H(p,n\pi^+)^1H$ is 287 MeV, the cross

section (Figure 29) for this reaction is quite small, even at energies greater than threshold.

Another source of neutrons on the sun is thermonuclear reactions in the corona. The corona has a temperature of about 10^6°K, or particle energies are about 100 eV. There is a suggestion that a ratio of about 5×10^{-15} of D/H atoms exists, Severnyi [1956], and we might expect some reactions of the type

$$D+D \rightarrow n+{}^3He \ . \qquad (25)$$

This fusion reaction is a binary one, i.e., two-body collisions are involved. Suppose a group of ions with kinetic temperature T are mutally colliding. The probability that two ions will react in passing close to each other is describable in terms of a mutual reaction cross section σ, which is a function of the relative velocity between the ions, v_{12}. The probability per unit time that a given ion of type 1 will react with another type 2 will be given by the product of the reaction cross section, σ, the relative velocity, v_{12}, and the particle density of atoms of type 2, n_2 ions/cm^3. Since there will exist a distribution of relative velocities the product σv_{12} must be averaged over the distribution appropriate to the kinetic temperature of the corona. Thus the reaction rate per particle of type 1 is

$$R_1 = n_2 \langle \sigma v_{12} \rangle_{av} \ . \qquad (26)$$

The total reaction rate per unit volume is then found by multiplying R_1 by the particle density of ions of type 1,

$$R_{12} = n_1 R_1 = n_1 n_2 \langle \sigma v_{12} \rangle_{av} \text{ reactions/sec/cm}^3 \ . \qquad (27)$$

For DD reactions,

$$R_{DD} = \frac{1}{2} n^2 \langle \sigma v_{DD} \rangle_{av} \ . \qquad (28)$$

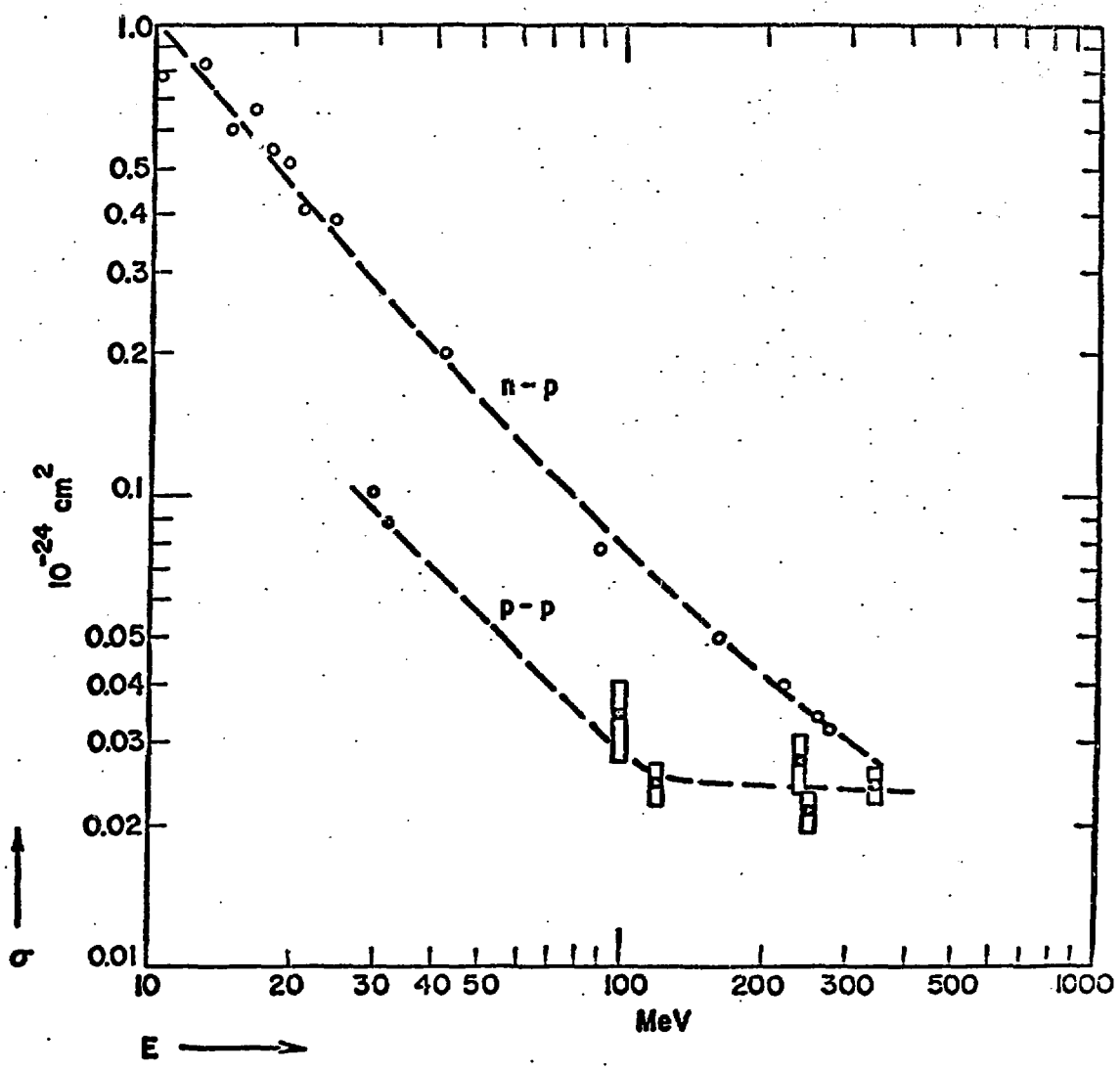

Fig. 29. The Total Cross Sections for n-p Scattering, σ_{np}, and p-p Scattering, σ_{pp}, at Various Energies.

It has been shown, by Arnold et al. [1954], that reaction cross sections at low energies can be fitted accurately by a Gamow barrier penetration expression. For the total DD reaction the expression is (energies in KeV, cross sections in barns),

$$\sigma_{DD} = 288 \frac{1}{W} \exp(-45.8\ W^{-1/2}) \ . \tag{29}$$

The value of $\langle \sigma v_{DD} \rangle_{av}$ can be obtained by integrating the product of the above equation and the particle velocity distribution over all possible relative velocities. For a Maxwellian distribution with a temperature T in kilovolts, the result obtained is, Gamow and Teller [1938],

$$\langle \sigma v_{DD} \rangle_{av} = 260 \times 10^{-16}\ T^{-2/3} \exp(-18.76\ T^{-1/3}) \ , \tag{30}$$

for T<50 KeV. At $T = 10^{6}$°K,

$$\langle \sigma v_{DD} \rangle_{av} = 0.4 \times 10^{-30}\ \text{cm}^3/\text{sec}. \tag{31}$$

The reaction rate for this process is given by

$$R_{DD} = n^2 \frac{1}{2} \langle \sigma v_{DD} \rangle \ . \tag{32}$$

If $n = n_0 (R/R_\odot)^{-m}$, we can write the total production N of neutrons in the corona as

$$N = \int R dV = \int k\, n_0^2 \frac{1}{2} (R/R_\odot)^{-2m} \langle \sigma v_{DD} \rangle\ 4\pi R^2\ dR \text{ neutrons/sec}, \tag{33}$$

where k is the neutron yield per DD reaction. The value of k is about 1/2 because the probabilities of the two possible reactions,

$$D+D \rightarrow n+{}^3He \tag{34}$$

and

$$D+D \rightarrow p+{}^3H \ , \tag{35}$$

are essentially equal.

From van de Hulst [1953], $n_0 = 2 \times 10^8$ and m = 7.5 for the known

electron densities in the corona, we get for the neutron flux at the earth,

$$\Phi = N/A = (kn_0^2 \langle \sigma v_{DD} \rangle 2\pi R_\odot^2)/[4\pi R_e^2(2m-3)] \quad ,$$

$$= 5 \times 10^{-10} \text{ neutrons/sec/cm}^2 \quad , \tag{36}$$

where R_e is the earth-sun distance.

However when a large flare occurs there may exist an important number of thermonuclear neutrons in the region of the corona above the flare. There are occasions when the corona temperature climbs to 3×10^6°K, or factors of ten higher locally, Friedman [1961]. The D/H ratio can increase to 1/10, Goldberg et al. [1958]. Consequently,

$$\frac{[(D/H)T^{-2/3} \exp(-18.76\ T^{-1/3})]_{\text{flare}}}{[(D/H)T^{-2/3} \exp(-18.76\ T^{-1/3})]_{\text{nonflare}}} = 1.1 \times 10^{12} \quad . \tag{37}$$

Assuming the flare covers an area 10^{-4} of earth-sun distance, an additional neutron flux at the earth may be

$$\Phi = (5 \times 10^{-10})(1.1 \times 10^{-12})\ 10^{-4} \quad ,$$

or

$$\Phi = 6 \times 10^{-2} \text{ neutrons/sec/cm}^2 \quad . \tag{38}$$

There does exist some evidence for the occurrence of thermonuclear reactions in the solar atmosphere during solar flares, Fireman et al. [1961]. Tritium was measured in samples of a lead sheet one-quarter inch thick, and in samples of a stainless steel battery case from the Discoverer XVII satellite. The tritium content was too large by a factor of more than one hundred to be explained by nuclear interactions

induced by incident protons or alpha particles. The tritium may have resulted from a flux of incident tritons that stopped in the material.

Although a huge flux of neutrons is produced inside the core of the sun, absorption effects severely decrease the fraction of neutrons that leak out of the sun to $\sim 10^{-87}$.

The last neutron source is associated with the existence of solar proton flares. Assuming that the proton flare is generated in the chromosphere and that one-half of these protons interact with the constituents of the photosphere, a rough estimate for the neutron flux at the earth yields around 26 neutrons/cm^2/sec, Hess [1963].

An attempt will be made to discuss the correlation of solar neutron production with proton and optical flares. The energy released by a solar flare is an important quantity, since we have not observed the magnetic fields in which the energy is stored until such time as it is triggered off to produce the flare. It is possible, Ellison [1963], to derive the energy radiated by, for example, a 4B flare at optical wavelengths from (a) the profiles of emission lines, or (b) the white light continuum integrated over the volume and lifetime of a flare ($\simeq$2 hrs for large flares).

The total radiation in emission lines plus continuum from (a) and (b) was estimated to be $\sim 10^{32}$ ergs. This is a lower limit since the emission lines lying outside the visible have been neglected. The value of $\sim 10^{32}$ ergs is in good agreement with the estimate of Parker [1957] for the flare of 23 February 1956, and it represents about one-thirtieth of the energy radiated by the whole sun in one second. The total optical emission of a 4B flare is greater than the total energy content of the normal solar atmosphere above the photosphere. If the

volume of a 4B flare is $\sim 10^{29}$ cm^3 (an extreme upper limit for such flares), then the average energy density released in the flare volume is at least 10^3 ergs/cm^3, which is about a hundred to a thousand times greater than the energy density of an equivalent nonflare region of the chromosphere.

The essential problems of the flare mechanism are to discover in what form this energy is stored and how its release is triggered. It seems that the most probable form of storage is in the local magnetic field, and if this is so, then $H^2/8\pi \sim 10^3$ ergs/cm^3, and we require the destruction of an average field of approximately 150 gauss over the entire flare volume. It should be noted that such a catastrophic annihilation of the field has never been observed.

In Severny's [1958] theory the essential feature is the instability of the plasma in an active region when the magnetic energy ($H^2/8\pi$) greatly exceeds the thermal energy density (NkT). A pinch effect develops near a neutral point, and compression and contraction of the plasma takes place in a matter of seconds. Temperatures of the order of 5-10 million degrees may then develop in a thin layer, perhaps only 10 km thick. The compression is eventually stopped by the development of a shock wave, and expansion then follows in the region behind the shock wave. The fine structure of "moustaches" in the early stage spectra are attributed to these turbulent regions, and in observational support of Severny's "pinch" mechanism, Severny's magnetic plots have shown that flares begin at or near neutral points, that there are high magnetic field gradients in the region, and that the flare produces a large reduction and redistribution of the isogauss pattern. The reasons

for triggering off the reaction when $H^2/8\pi >> NkT$ are not at all clear. Whether the behavior of the magnetic fields actually conforms to Severny's model is subject to debate since there is not agreement on the interpretation of the observations.

It does seem that more extensive observations of the various aspects of flares and a more thorough understanding of plasma physics are still required before a more accurate theory of the flare mechanism can be propounded. The theory must account for all the characteristic observational features, including (1) the slow buildup of energy densities, some hundred times the normal thermal values, within a limited volume; (2) the catastrophic release of energy during the flash phase; (3) the location of the bright flare filaments in relation to the sunspots, and their restriction to the chromosphere; (4) the emission of x-rays and the generation of the various types of radio noise emission in their correct sequence; (5) the acceleration of protons and electrons to high energies.

A physical model for the coronal (radio) flare process has been suggested by Wild [1962] in which he attempts to explain qualitatively the various physical phenomena that follow the above-mentioned plasma discharge. Wild assumes that the flare is initiated in a neutral plane between two spot groups, as envisaged in several electromagnetic theories of flares. The plasma instability triggers off a Fermi mechanism causing the immediate ejection of a shower of relativistic electrons; these generate the Type III and Type V radio bursts above the disturbance, the microwave early burst, and the hard x-rays below and around the flash region. At the same time a magnetohydrodynamic shock conveying

ions and electrons passes upward from the center at a speed of 1000 km/sec. This shock front is identified with the source of the Type II burst in this model.

The interaction of the shock front and the various particles accelerated by the magnetic perturbations within the ejected cloud traveling behind it leads to the Type IV radiation and to the acceleration of the high-energy protons, whose secondary emissions are detectable at ground level on the earth. Under some conditions the model suggests that the efflux of the plasma will be of sufficient energy to carry the magnetic field of the region away from the sun to yield the Type IV-B component of radio emission, which is the "classical" type discovered by Boischot [1958], who investigated its properties.

The initial acceleration of electrons during the flash phase of the flare leads to the production of x-rays. From a statistical analysis of events recorded during the first six months of the IGY, Hackenberg and Kruger [1959] concluded that SID's (sudden ionospheric distrubances) occur only when centimeter radiation (3.2 cm) is detected. This appears to indicate that Bremsstrahlung x-rays (1-10 Å) are generated at the same level as the centimeter radiation. They suggest this is 2000-6000 km above the photosphere, but Kundu [1962], who reaches similar conclusions, suggests a height in the range 15,000-30,000 km which seems more probable. This would be in agreement with the findings of Warwick [1955] that limb flares below 15,000 km do not generate SID's. Fokker [1962] also formed a close association between bursts of ionizing x-rays and centimeter radiation in his studies of geomagnetic solar flare effects (crochets) and the microwave bursts.

Type III and Type V bursts occur simultaneously with some x-ray emissions where the Type III bursts are characterized by a "fast" drift in the frequency of maximum intensity from high to low frequencies at a rate of approximately 20 MC/sec/sec (these appear to indicate $0.2 \leqslant v \leqslant 0.8c$). These events usually occur in groups near the start of flares and subflares, and they may have a 10 minute duration. Their polarization is either random or partially circular or elliptical. The Type V emission is a short continuum burst (possibly synchrotron radiation) lasting a few minutes after the Type III. The Type II events which are characterized by a "slow" drift in the frequency of maximum intensity from high to low frequencies at a rate of approximately 0.25 Mc/sec/sec occur in the post-maximum phase of certain important flares, last for about ten minutes, and generally have random polarization.

Uchida [1962] has suggested that the Type II and Type III bursts, though having a common radiation mechanism, may have distinctly different excitors such that the Type III being produced by the free streaming motion of individual high-velocity electrons, while the Type II bursts could be due to plasma oscillations caused by a hydromagnetic shock, perhaps through charge separation at the shock front. Maxwell and Thompson [1962] find, whatever the generating mechanism, that the regions of origin of individual plasma frequencies are at much greater heights in the solar atmosphere than would be expected from conventional models of electron density. Their data suggest that the initiating disturbances are being propagated outward along coronal streamers, which may be aligned along lines of force extending outward from the flare.

After the Type II slow drift bursts, a broad-banded continuum emission, which may last from several minutes to days and whose dynamic

spectrum is featureless, may be observed. This is the Type IV continuum emission. It begins during or after the flash phase of the flare, as observed optically in H_α light, and reaches a maximum intensity some 20-30 minutes later. Radio astronomers now consider that at least three phases of Type IV radiation can be distinguished; these have been summarized by Kundu and Smerd [1962] as shown in Table 8.

Type IV-B is the "classical" Type IV radiation discovered by Boichot, and which Boischot and Pick [1962] suggest is produced by synchrotron radiation from a source of relativistic electrons ejected by the flare and spiraling in a magnetic field.

Type IV-A emission is an extension of the Type IV bursts at decimenter and microwave (centimeter) bands. Takakura and Kai [1961] consider the decimeter emission, not as a high-frequency component of the meter wave emission, but as a separate radiation. Hackenberg and Kruger [1959] interpret the centimeter continuum radiation as a quasi-thermal one generated by free-free transitions. They consider that its occurrence indicates the presence of a cloud of superthermal electrons in the flare plasma.

Something about the behavior of the magnetic fields of an active region can be deduced from a study of the particle emissions from flares. These can be divided in three classes of different energies: (a) the high energy (>1 BeV) protons which produce secondary cosmic-ray events at ground level (GLE); (b) protons of lower energy (10-400 MeV) which are responsible for the ionospheric polar cap absorption effects (PCA); (c) clouds of particles with low energies (<1 MeV) which generate geomagnetic storms and auroral displays.

TABLE 8

THREE PHASES OF TYPE IV RADIATION

	IV-A	IV-B	IV-C
Spectral range	10,000 to ~ 250 Mc/sec	~ 250 to 25 Mc/sec	~ 1000 to 25 Mc/sec (the upper frequency limit is uncertain)
Beginning	At or near flare start	Usually within minutes of a Type II burst; after flare maximum.	Following a IV-B
Duration	Several tens of minutes	Several tens of minutes	Hours (possibly days)
Polarization	Partially circular	Partially circular	Strongly circular
Location	In bright region, near flame	Well away (up to several solar radii) from the flare after initial movement.	Closer to flare (a fraction of a solar radius) than IV-B.
Movement	Not appreciable	Early, large-scale movement away from flare at speeds of several 100 km/sec.	None
Source size	Small (< 5' arc)	Large (~ 10' arc)	Small (a few minutes of arc)
Directivity	Little	Little	Strong toward the center

It is these plasma clouds (c) which draw out into interplanetary space some part of the magnetic field of sunspots, thereby creating radial magnetic fields which expand outward and frequently envelope the earth. When such clouds are ejected from the sunspot region, the ends of the magnetic lines of force remain anchored at the sun, while the loops continue to thread the ejected material. A magnetic bottle is thus formed such that its lines of force are approximately in the plane of the ecliptic, and the solar rotation bends these radial fields convex toward the West. The concept of a magnetic bottle is necessary to provide a working hypothesis for the transmission of high energy ($>$ 1 BeV) protons from flare outbursts to the earth, where they produce cosmic-ray effects at ground level. If the earth is in such a bottle, then:

(a) If a major flare occurs in the active region within the neck of the bottle, there will be already in existence direct trajectories, consisting of lines of force, along which the high-energy particles can spiral from the flare to the region of the earth's field. At the earth the particles will appear to arrive from the west of the sun-earth line, and this has been deduced from the records of some earlier solar cosmic-ray events by McCracken and Palmeira [1960].

(b) Energetic particles do not travel in straight lines but are guided in helical trajectories around the lines of force. Thus there is a much greater probability of high-energy protons reaching the earth from a flare which occurs in the Western Hemisphere of the sun (see Figure 30). In general Class 3 and 4B flares are distributed quite uniformly across the disc in longitude and Bell [1961], who studied the longitude distribution of 580 flares of importance 2B

Figure 30

Heliographic Coordinates of the 14 Flares Which Have Generated High-Energy (> 1 BeV) Protons Recorded on the Earth by Their Secondary Effects at Ground Level (GLE). Note Predominance of Western Positions. These Flares Occurred on I 28 February 1942, II 7 March 1942, III 25 July 1946, IV 19 November 1949, V 23 February 1956, VI 16 July 1959, VII 4 May 1960, VIII 12 November 1960, IX 15 November 1960, X 20 November 1960, XI 18 July 1961, XII 20 July 1961, XIII 31 August 1956, and XIV 3 September 1960.

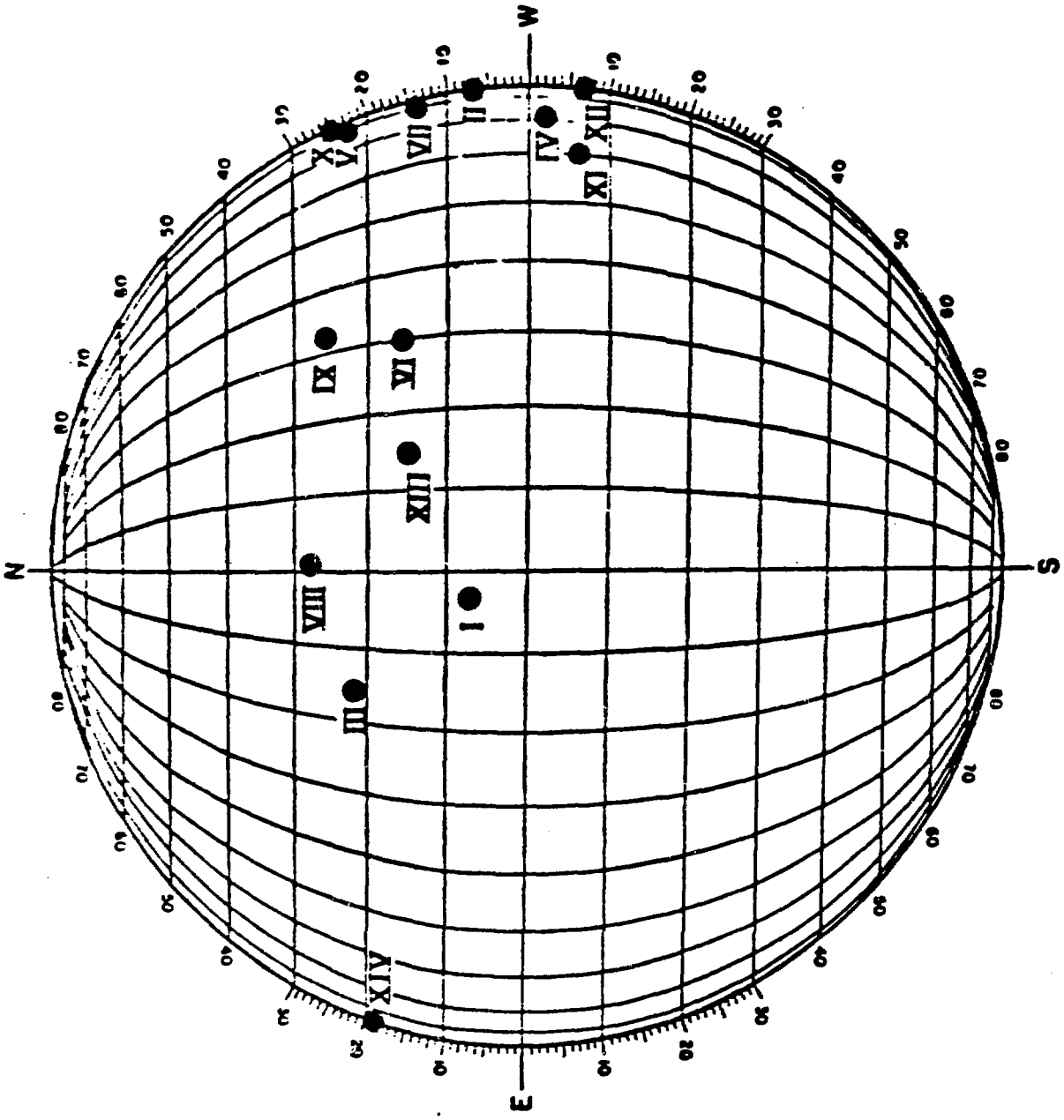
W
E
N
S
I
II
III
IV
V
VI
VII
VIII
IX
X
XI
XII
XIII
XIV

or greater, found that exactly half occurred to the east of the central meridian and half of them to the west.

(c) When the earth is inside a magnetic bottle it will be shielded from the influx of galactic cosmic rays, and there may be a reduction (the Forbush decrease) of as much as 30% in the energy flux (1-10 BeV) of the galactic component. The onset of this decrease coincides with the arrival of the geomagnetic storm particles at the earth.

The recovery period for the galactic component of cosmic rays to its normal level extends over some 5-10 days and this suggests that the life of the magnetic bottle with its guiding lines of force for high-energy solar particles is of the same order.

The July 1961 event, Ellison et al. [1962], is a very good illustration of the formation of a magnetic bottle. A complex magnetic sunspot group developed rapidly after its passage in from the east limb on 7 July. The first major flare (Class 3) occurred on the 11th and a second (Class 4B) on the 12th when the spot group was 22° east of the central median. No high-energy particles from either of these flares reached the earth, but the flare on the 12th ejected a cloud of low-energy particles. These reached the earth 25 hours after the flare, generating a sudden commencement geomagnetic storm, and a simultaneous Forbush decrease of the galactic component of cosmic-ray intensity occurred. The earth was now enveloped in a magnetic bottle and the high-energy protons from the next two major flares in the group, a 4B on the 18th and another 4B on the 20th, found ready-made and easy trajectories to the earth, arriving some 35 minutes and 20 minutes, respectively, after the causative flare.

Biermann et al. [1951] first introduced the idea that high energy flare protons which were accelerated from the chromosphere into the denser photosphere would interact with the constituents of the photosphere producing neutrons which might reach the earth. In Part I, Lingenfelter et al.[1965] calculate the intensity and energy spectrum of neutrons above 1 MeV produced in the solar photosphere by flare-accelerated protons and α particles. The solar neutron yield from accelerated particles on helium is found to exceed the yield from evaporation and spallation in heavier elements for incident energies above about 30 MeV and continues to dominate until about 1 BeV. At higher bombarding energies, the p, π^+n reaction in hydrogen is the main neutron source. More than 90% of the total solar neutron production is from knock-on reactions by protons in hydrogen and helium. Owing to this relatively high ratio of knock-on to evaporation neutrons, the solar neutron spectrum is much higher in energy than the spectrum of secondary neutrons produced in the earth's atmosphere by galactic cosmic rays. A Monte Carlo calculation is performed to estimate the solar neutron flux escaping from the photosphere into space.

Lingenfelter et al. [1965], in Part II, calculate the intensity and energy spectrum of solar neutrons at the earth relative to the flux of solar protons observed during the last solar cycle, using the solar neutron production spectrum obtained in Part I. The time-average solar neutron flux above 10 MeV at 1 AU over the last solar cycle is found to be 3×10^{-3} neutrons/cm^{2}sec, with a peak intensity at 30 to 40 MeV. This solar neutron flux is comparable to the neutron leakage flux above 10 MeV produced by interactions of galactic cosmic rays with the earth's atmosphere, indicating that solar neutrons may

be competitive with leakage neutrons as a source of high-energy decay protons and electrons in the earth's radiation belts. Several anomalous features of the radiation belts are qualitatively consistent with a solar neutron source of the calculated intensity and spectral shape. Following individual major flares, essentially monochromatic bursts of solar neutrons should be observable at high altitudes but no sea level effects are expected.

More recently, Lingenfelter [1969] has examined the interaction of accelerated charged flare particles with the ambient gas which leads to ionization losses and resultant nuclear interactions (with lesser efficiency) which can produce neutrons and gamma rays that can escape directly from the flare region. The ionization losses of accelerated particles in the solar chromosphere can be related to the energy of the optical emission in solar flares, Gordon [1954]. In a detailed study of the ionization loss and optical emission processes, Dubov [1963] has demonstrated both the total energy and time dependence of the flare optical emission, principally in H_α and L_α, can result from energy loss of accelerated particles in the flare region by ionization and excitation.

It is known that many chromospheric flares are accompanied by an increase in the cosmic-ray flux at the earth. For a rough preliminary estimate it has been assumed that 10^{33} particles with an energy of 10^9 eV are formed during the flare, that the density is 5×10^{12} atoms/cm^3, in 1 cm^3 there being 10^7 hydrogen atoms in the second atomic level and 2.3×10^6 hydrogen atoms in the third level, that the area of the flare is 3×10^{19} cm^2, and that it occurs at a height of 10^8 cm, Stepanyan [1962]. The ionization losses

suffered by the fast particles have been calculated from Bethe's formula,

$$K = \frac{4Nz^2(Z/A)\pi r_e^2 m_e c^2}{\beta^2}\left[\ln\frac{2m_e c^2\beta^2}{(1-\beta^2)I(Z)} - \beta^2\right], \qquad (39)$$

where K is the energy loss per gm/cm^2, N is Avogadro's number, $\beta = v/c$ is the ratio of the velocity of the incident particle to that of light; z, Z, and A for fast protons moving in hydrogen are all equal to unity, r_e is the classical radius of the electron, m_e its mass, and I(Z) is the average potential for excitation and ionization, which has been taken equal to 13 eV. It was found that the average energy loss is 0.15 erg/cm^3 sec. Over a period of 10^3 sec and within the above flare volume, this leads to an energy liberation of 4.5×10^{29} ergs which corresponds to the total energy radiated by the flare. The energy liberated in a column of 1 cm^2 in cross section will be 1.5×10^7 ergs/cm^2 sec. On the other hand, the energy radiated by the flare in H_α (Balmer line) is between 7 to 8×10^6 ergs/cm^2 sec sr. In the case of L_α (Lyman line) the corresponding figure is about 4×10^6 ergs/cm^2 sec sr, or less than 10^7 ergs/cm^2 sec sr, according to rocket measurements. It seems that H_α and L_α must remove almost all of the energy liberated in flares (1.5×10^7 erg/cm^2 sec) in about equal amounts.

Sobolev [1956] shows that the energy carried away by radiation which arises directly from excitation and ionization by fast particles and the subsequent recombination is very small and the excess energy remaining in the chromospheric medium must lead to an increase in temperature. This continues until the number of hydrogen atoms in the thrid level reaches the value of $2\text{-}3\times10^6$/cm^3, at which stage radiation

can carry away all of the energy liberated per unit volume. The temperature reached will be approximately 10^4°K. For this, an energy liberated of about 24 ergs/cm^3 is necessary. Thus, the time of initiation of the flare is 24/0.15 = 160 sec. The change in brightness does not begin immediately after the appearance of additional radiation, but only after an interval which is close to the average lifetime of the quanta in the volume under consideration. According to Sobolev [1956] the lifetime is of the order $\bar{t} = \bar{z}t$, where $\bar{z} = \tau_o^2/4$ is the average number of scattering collisions and t is the mean free time of the quantum between successive collisions. With $t \sim 1/A_{ik}$, where A_{ik} is the Einstein coefficient of spontaneous transition; $\tau_o = zn_iK_{ik}$, where τ_o is the optical thickness, n_i is the number of atoms in the i th state, K_{ik} is the mean absorption coefficient of the atom; we get $\bar{t} \simeq 6.7 \times 10^{-5}$ sec for H_α and $t \simeq 1.3 \times 10^{-6}$ sec for L_α. If we take into account the escape of quanta in the line wings, then in view of the high optical thickness, the estimate of the time delay between the production of the additional radiation and the increase in the observed surface brightness in L_α will be changed by no more than a factor of 1000. Thus the time spent by a quantum in the medium will be of the order of 1000 sec. The delay time will also be affected by the diffusion of quanta in the gas above the flare. It can be seen from this that the increase in L_α emission will start at a later time than the onset of the flare in H_α.

In order to test the mechanism as suggested by Gordon [1954], one can for a given class flare, an associated charged particle characteristic rigidity, and an associated measured neutron and gamma-ray

flux generate an experimental number for the optical power. Lingenfelter [1969] has calculated the secondary neutron and gamma-ray fluxes at the earth per unit power dissipated by ionization losses of accelerated particles in a solar flare as a function of the rigidity, P_o, which characterizes the accelerated particle spectrum (see Figure 31).

As an example for solar neutrons, Bame and Asbridge [1966] have monitored neutron fluxes on the Vela satellites for more than three years beginning in late 1963. The largest flare during this period was the class 3 flare of 2 September 1966, for which they set an upper limit to the solar neutron flux of ≤ 2 neutrons/cm^2 sec. The measured charged particle spectrum associated with this flare had a P_o of 60 MV. For this P_o we see from Figure 31 that the neutron flux at the earth would be about 6×10^{-30} neutrons/cm^2 sec per ergs/sec. Thus the neutron flux upper limit implies an ionization loss power $\leq 3\times10^{29}$ erg/sec. As summarized by Kiepenheuer [1965], the optical power of class 4B solar flare is typically $\leq 10^{29}$ erg/sec. This is consistent with the suggestion that the optical power can be derived from ionization losses.

An interesting model, Simnett and Holt [1971], has been presented which shows that large numbers of energetic electrons (0.3 to $>$ 10 MeV) and protons (1-30 MeV) can be stored in the solar corona at altitudes around 3×10^5 km for periods in excess of 5 days. Constraints on the trapping volume are probably not adequate for storage of high energy protons ($>$ 30 MeV) in the corona. However, perhaps other storage volumes can exist towards the photosphere for high energy protons.

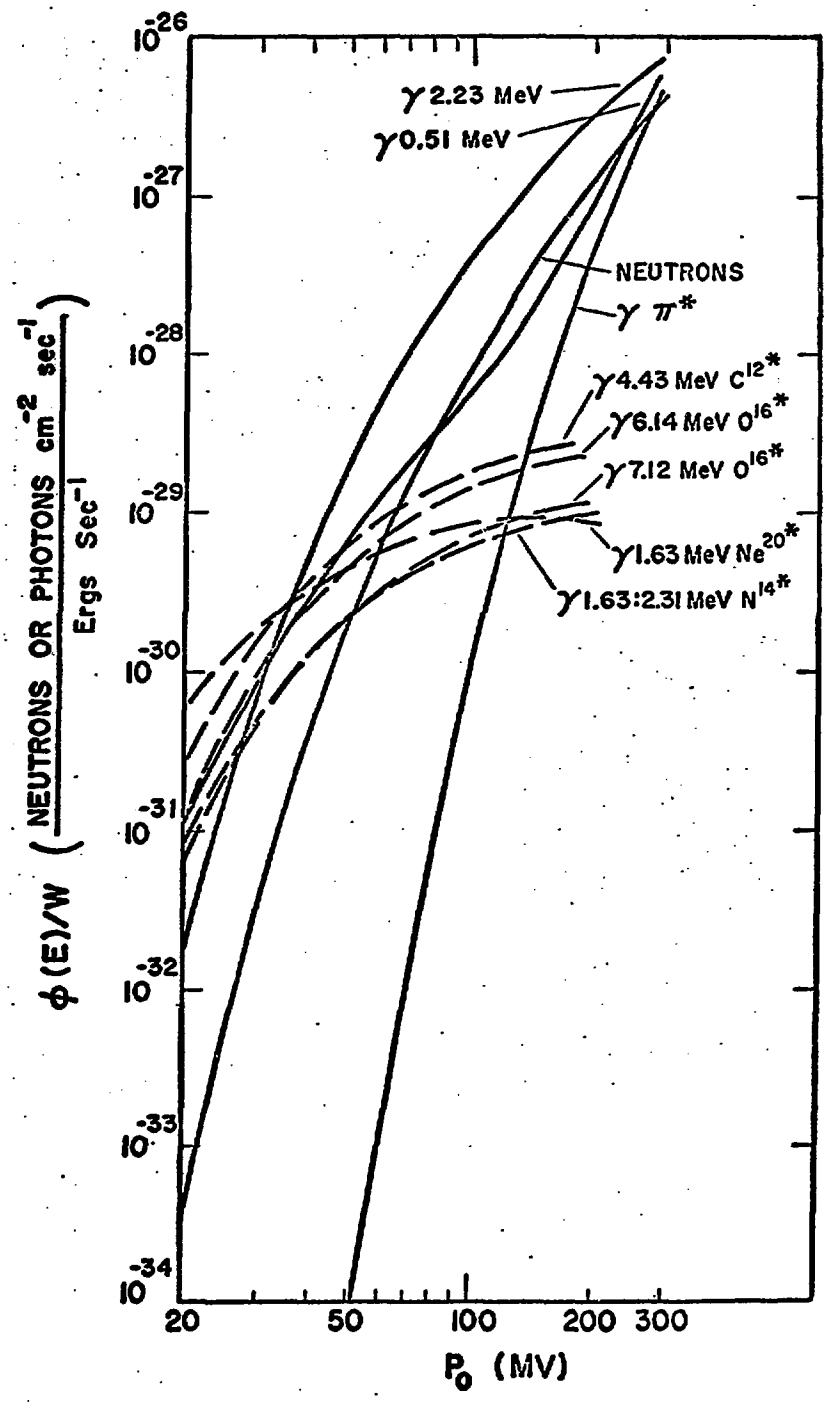

Fig. 31. Secondary Neutron and Gamma-Ray Fluxes at the Earth per Unit Power Dissipated by Ionization Losses of Accelerated Particles in a Solar Flare as a Function of the Rigidity, P_o, Which Characterizes the Accelerated Particle Spectrum.

An interesting problem might be to examine the proton data for neutron-decay protons, Roelof [1966], accompanying primary protons from a pulse-type solar flare. Neutrons decay spontaneously in free flight according to the scheme $n \rightarrow p + e^- + \bar{\nu}$, with a mean lifetime of $\tau = 1010 \pm 25$ seconds, Sosnovskii et al. [1959]. Thus a significant fraction of solar neutrons would decay before traveling 1 AU (97% of 10 MeV neutrons, 59% of 200 MeV neutrons), thereby injecting protons of nearly the same energy into the interplanetary medium. The interplanetary magnetic field will play a key role in the fate of the decay-proton flux (see Figure 32). Correlation of decay-proton fluxes to nonexistence or existence of magnetic bottle which envelopes the earth could be informative.

Another neutron production model involves the analysis of white-light flares. Under the assumption that white-light flares are caused by energetic particles penetrating into the photosphere, Svestka [1971], the known number of protons needed for the white-light emission is used to obtain an estimate of the production of neutrons at the same time.

The flares visible in white light have been observed mostly as a short-lived appearance of the brightest portion of the flare in the integrated photospheric light. Only in a few cases has the spectrum been recorded, but these observations were too incomplete to give any information about the intensity distribution in the continuous spectrum. See Table 9 for a list of observed white flares.

The color of flares visible in the integrated light is usually described as "white" or "bluish white." This indicates that the intensity distribution of the flare continuous emission was either

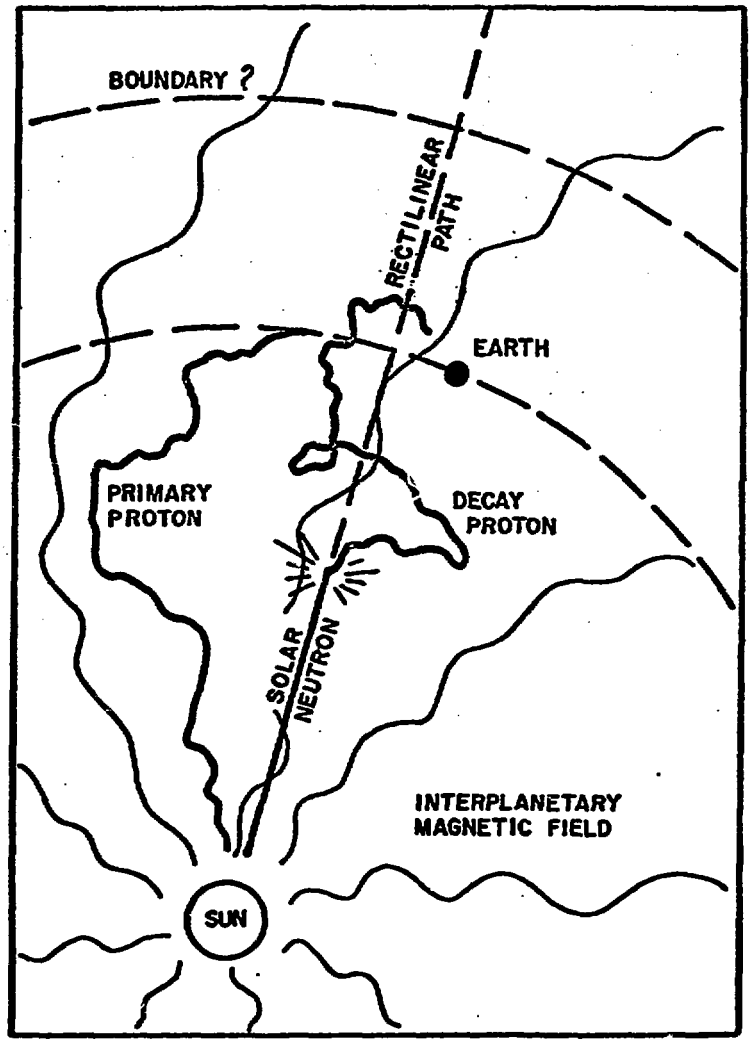

Fig. 32. Schematic of Primary and Neutron-Decay Solar Proton Paths in a Scattering Interplanetary Magnetic Field.

TABLE 9

FLARES VISIBLE IN WHITE LIGHT

Date	Position	Imp.	Duration	Color	Observed in	Observer	Proton Emission*
1 Sep 1859	12 W	3+	7 min	white	total light	Carrington (1859) Hodgson (1859)	
17 Jun 1891	80 W	3	6 min	yellowish	total light	Trouvelot (1891)	
21 Feb 1921	42 W	3+	8 min	magenta	total light, over spot	Martheray (1922)	
21 Sep 1928	?	3	2 min	white	total light	Martheray (D'Azambuja 1947)	
26 Jul 1937	31 E	3	?	equally visible in red, green and blue	total light	Waldmuer (1941)	
31 Mar 1938	82 E	3	6 min	27% of continuun at λ 3220 Å	UV light	Dobbie et al. (1938)	
5 Mar 1946	10 E	3+	3 min	white	total light	Martheray (D'Azambuja 1947)	
25 Jul 1946	16 E	3+	short	10% of continuun at λ 6200 Å	spectrum, over spot	Ellison (1946)	(B)G
19 Nov 1949	72 W	3+	short	8° of continuin the H_α region	spectrum	Ellison and Conway (1950)	BG
18 May 1951	30 W	3	1 min	?	total light	Porret (1952)	
23 Feb 1956	79 W	3+	5 min	white	total light	Unno and Shimizu (Notuki et al. 1956)	BPG
31 Aug 1956	15 E	3+	1 min	?	total light	Greenwich Observatory (Quart.Bull.Sol.Activ.)	BP(G)
30 Aug 1957	20 E	?	20 min	white	total light	McNarry (1960	B
3 Sep 1957	30 W	3	6 min	bluish white	total light	Beckler (1958)	(B)P
23 Mar 1958	74 E	3+	8 min	bluish white	total light	Beckler and Kuenzer (Beckler 1958)	BP

TABLE 9 (cont.)

Date	Position	Imp.	Duration	Color	Observed in	Observer	Proton Emission*
30 Mar 1958	63 E	2	2 min	white	total light	Denloke (Beckler 1958)	
8 Apr 1959	85 E	2+	?	?	total light	German Capri Station (Quart.Bull.Sol.Activ.)	B
3 Sep 1960	88 E	2+	15 min	white	total light	Angle (1962)	BPG
15 Nov 1960	33 W	3	3 min	pearl white	total light	Koyama (Nagasawa et al. 1961)	BPG

*Letters in the last column denote: B - a Type IV burst recorded (svesta and Olmr 1966); P - a PCA event followed (Basler and Owren 1964); G - GLE associated.

similar to that of the normal photospheric light or the intensity increased towards the violet side of the spectrum as compared to the background solar spectrum, red enhancement not being excluded.

There is one case, however, which indicates an intensity increase towards the red in the emitting area. It was observed by Martheray [1922] on 21 February 1921. Martheray describes that the flare area, observed as a bridge over a sunspot, was magenta-red in the maximum phase and during the decrease of intensity it became rosy to yellowish before its final disappearance. It might have been due to some error in observation were it not preceded by a similar observation by Trouvelot [1891], who also described the color of the white-light flare as "yellowish."

Some of the physical processes that have been considered to explain white-light flares are (1) hydrogen free-bound transitions, Ellison and Conway [1950], (2) free-free transitions, scattering by free electrons, and H^- emission, Zanstra [1950], (3) relativistic electrons, Stein and Ney [1963], and (4) flare penetration into the photosphere, Mustel [1955]. The white-light flares might be caused by an increase of temperature in the photosphere beneath the flare. The lack of an excess of the number of white-light flares near the limb, however, does not support this hypothesis. If white-light flares were produced by relativistic electrons, their x-ray production should be much higher than observed. An attractive explanation is that the emission is produced by the formation of negative hydrogen ions, which presupposes very low electron temperature in the flare.

McCracken [1959] has called attention to the close relationship between the flares associated with GLE and white-light flares. We observe in Table 9 that since 1946 when radio astronomy was introduced, all white-light flares were associated with Type IV bursts except for Denloke's observations. Six of the white-light flares were correlated with GLE's while six were followed by PCA events. Although many white-light flares escape detection, these flares can be taken as one of the characteristic properties of proton flares. The majority of the solar flares which were observed to produce increases in the terrestrial cosmic ray intensity were also observed in white light. This is interpreted as evidence that it is only the most energetic flares which produce any appreciable quantity of cosmic radiation, and that the rarity of the cosmic ray flare effect is, at least in part, due to the rarity of very energetic solar flares. The white-light flare location may mark optically the region where the most important part of the hard x-ray burst and the first maximum of the radio microwave flux are produced. Data in Svestka [1970] strongly indicate that the continuous emission of disc type white light flare appears at the same time when the first maximum of the radio microwave flux and the hard, non-thermal and impulsive, x-ray burst are observed. It also precedes the H_α maximum, which contradicts the generally accepted statement that the white-light and H_α maxima coincide in time.

McLean et al. [1971] has recently explored a possible mechanism to accelerate solar electrons and protons in the solar corona. The basic model involves the interaction of a shock or other magnetohydrodynamic (MHD) wave with a discrete arch-shaped magnetic flux tube which is embedded in the solar corona and anchored in the photosphere.

Evidently the upward expansion of the shock wave through the magnetic flux tube sets the stage for Fermi acceleration. This model has been used to explain certain characteristics of the Type IV radiation which result from the acceleration of the electrons and modulation of the synchrotron radiation. This same mechanism may be effective in accelerating protons in the same region. Since this interaction seems to occur at a height between 1 and 2 $R_\odot$, and if the resultant angular distribution of the proton flux was peaked away from the sun, the likelihood for neutron production in the photosphere appears improbable. Table 10 shows the correlation between certain measured Type IV radiation and solar proton events. Four of the seven Type IV events for which proton data were available were associated with proton emission.

In considering the neutron fluxes likely to originate in the corona we may obtain a rough estimate from the calculations of Lingenfelter and Ramaty [1967]. For a very large proton event (e.g. that associated with the flare of September 2, 1966) producing a total of 6×10^{33} protons greater than 30 MeV it is estimated that the peak neutron flux at the earth would be about .06 neutrons/cm^2sec per gm/cm^2 of path length traversed by the accelerated particles. From the abundance of light nuclear fragments in charged particle fluxes observed from other large flares it appears that the material traversed by the accelerated particles lies in the range from 0.2 to 1.0 gm/cm^2. If acceleration times are in the range of 100 to 1000 seconds, mean densities of 10^{10} to 10^{12} particles/cm^3 are implied for the material traversed.

Various density models of coronal features discussed in Billings [1966] suggest local densities in the range from 10^7 particles 1 cm^3 at two solar radii to as high as 10^{10} at lower altitudes in large bright condensations. Thus it is not possible to rule out the

TABLE 10

COMPARISONS WITH SOLAR PROTON OBSERVATIONS

Flare					Cosmic-Ray Increase		
Date	Time of Maximum (UT)	Coordinates		Imp.	Date	UT	Delay (h)
27 Jun 1960	0010	S10	E33	3	No date		
24 Feb 1969	2316	N12	W32	2B	25 Feb	1000-1100	(~ 11)
27 Sep 1969	0412	N09	E02	3B	27 Sep	0900	5
8 Apr 1970	2333	N15	E55	SN	No increase		
30 Jun 1970	0316	N18	E56	SN	No increase		
5 Nov 1970	0320	S12	E37	3B	5 Nov	0200-0800	< 5
11 Dec 1970	2215	N16	W00	2N	12 Dec	0900	7
25 Jan 1971	2309	N19	W49	2B	25 Jan	2366	0.5

corona as a source of appreciable neutron fluxes, at least under conditions of extreme local condensation and energy density. However, the average coronal density above active regions of 10^7 particles/cm^3 would result in path lengths for accelerated particles or at least a factor of 1000 less than those suggested by the considerations of Lingenfelter and Ramaty. Thus significant neutron production might be expected only from extraordinarily dense structures in the corona.

V. PRESENTATION OF THE DATA

A. Selection of Neutron Data and Flare Data

A general survey was first conducted of all the neutron data from August 1969 to January 1971 in an attempt to search for solar neutron bursts. No evidence of solar neutron bursts were found. Ro [1971] examined in detail the 1969 solar neutron data by hand and found possibly no significant neutron fluxes. Ro arrived at an average solar neutron flux of $(.08 \pm .04) \times 10^{-2}$ n/cm^2 sec. He also explored the correlation of the neutron flux to radio bursts (2800 MHZ) and sunspot activity.

A rational approach to the analysis of the 1970 solar neutron data had to be devised. Much theoretical effort has been devoted to the production of solar neutrons in the solar photosphere by Ligenfelter and Ramaty [1967] and Svestka [1971]. These authors associate the production of neutrons with the occurrence of optical and white light flares. For example, Lingenfelter and Ramaty discussed theoretically the production of neutrons by energetic protons impinging into the photosphere, and estimated the peak flux of neutrons at the earth after the major cosmic-ray flare (3B) of 12 November 1960, to 33-70 n/cm^2 sec.

Under the assumption that white-light flares are caused by energetic particles penetrating into the photosphere, Svestka [1971], the known number of protons needed for the white-light emission is used to obtain an estimate of the production of neutrons occurring at the same time. For the white-light flare of 23 May 1967, the peak flux

of neutrons at the earth was estimated to be greater than 3 n/cm^2 sec.

Furthermore, Lingenfelter [1965] has estimated the neutron flux from solar optical flares under the assumption that the energy of optical emission in flares is completely provided by ionization losses of accelerated protons in the flare region. With this energy estimated to be 10^{29} erg/sec (average optical power for 3B flare; see Kiepenheuer [1965]) and assuming an exponential rigidity spectrum of the accelerated protons in the flare region is P_o = 100 MV, the neutron flux at the earth is estimated to be less than 10 n/cm^2 sec.

It seemed reasonable to test these neutron production models of Lingenfelter, Ramaty and Svestka. Does there indeed exist a correspondence between the OSO-G measured neutron fluxes and the optical and white-light flares? Comparison of flux values would also prove informative. To test these models an intelligent method for the selection of optical and white light flares has to be devised. The selection of white-light flares proved to be a simple task; only two white-light flares were noted during the period August 1969-July 1971. No neutron events were observed for the 4 January 1971 white-light flare while a flux of $(3.23 \pm 1.777) \times 10^{-2}$ n/cm^2 sec was estimated for the white-light flare that occurred on 23 November 1969. No white-light flares occurred during 1970.

The following conditions served as a guide to the selection of optical flares. These flares were selected from comprehensive reports compiled by the Aeronomy and Space Data Center [1970-1971].

(1) Importance number $\geq$ 2B

(2) Temporal clustering of flares

(3) Clustering of flares relative to observatories

(4) Duration of flares

(5) Flares were selected at or near occurrence of outstanding solar proton events.

Although the primary aim of this work was to test the solar neutron production models of Lingenfelter, Ramaty, and Svestka, there certainly exists neutron correlation studies with other solar processes such as hard x-ray bursts, Type IV radiation, etc. It has been shown, Boischot and Pick [1962], that there exists a strong relation between solar radio emissions and cosmic ray increases. This is due to the fact that the radio emission, certainly non-thermal on metric wavelength, comes from high energy particles. These particles are mostly electrons, instead of the protons observed with cosmic ray detectors when the sun is active. But it is easy to believe that a mechanism of acceleration of particles in the solar atmosphere, such as Fermi's mechanism, would give acceleration of both positive and negative particles. Five of the 66 solar neutron events selected showed some correlation with either Type II or Type IV radio bursts. These particular Type IV radio bursts were not associated with the major solar proton events noted in Appendix 3. Future solar neutron correlation studies with hard x-rays and radio emission bursts are planned.

A survey of all computer-selected solar neutron events for 1970 revealed no obvious periods of high flux. Since an isotropic background of neutral events had been shown to be present, Place [1972], and since continually shifting counter sensitivities placed the computer selection process somewhat in doubt, it was decided to select likely periods during 1970 and examine the data carefully by hand. Accordingly, complete printouts were obtained for selected periods of about twenty hours

each following the selection criteria outlined above. The philosophy followed was not to look for correlations with various indices of solar activity, but to look in detail at selected periods to see if any evidence for solar neutrons could be found. From the list of 62 acceptable flares, Appendix 2, two of which were white-light flares, 20 hours of neutron data per flare was examined with 10 hours before and after the occurrence of the flare. Forward solar neutron events were selected with low guard count rates ≤ 100. Normally high guard rates are associated with events recorded in or near the South Atlantic anomaly where single count rates are very high. Figure 33 shows the results of a satellite-charged particle measurement made at 320 km during the period 19-20 August 1960, to locate the boundary of the South Atlantic anomaly, Vernov et al. [1967].

To exclude earth albedo neutrons from this study the angles SPA and (112°-ZAP), Figure 34, and an estimated neutron energy for each forward solar neutron event were used to estimate roughly the efficiency for a solar measurement versus that of an earth albedo measurement. Events with the following conditions on the efficiency, ε, were excluded,

(1) $\varepsilon_{solar} = \varepsilon_{albedo} = 0$

(2) $\varepsilon_{solar} \leq \varepsilon_{albedo}$.

Figure 35 summarizes the events selected with corresponding flare numbers and efficiencies. Flares and neutron events are listed in Appendix 2 in chronological order. The 60 optical solar flares consisted of forty 2B, four 3N, twelve 3B, one 4N, and one 4B flares. See Tables A1 and A2 (Appendix 2) for explanation of notation used.

Figure 33

The Lines of the Equal Counting Rate of a Scintillation Counter Aboard a Satellite, Vernov et al. [1967], at 320 km Altitude during the Period 19-20 August 1960. The Numerals Denote Counting Rates cm^{-2} sec^{-1}. Also shown is the Location of the OSO-6 Spacecraft when Solar Neutron Measurements Listed in Figure 36 were made.

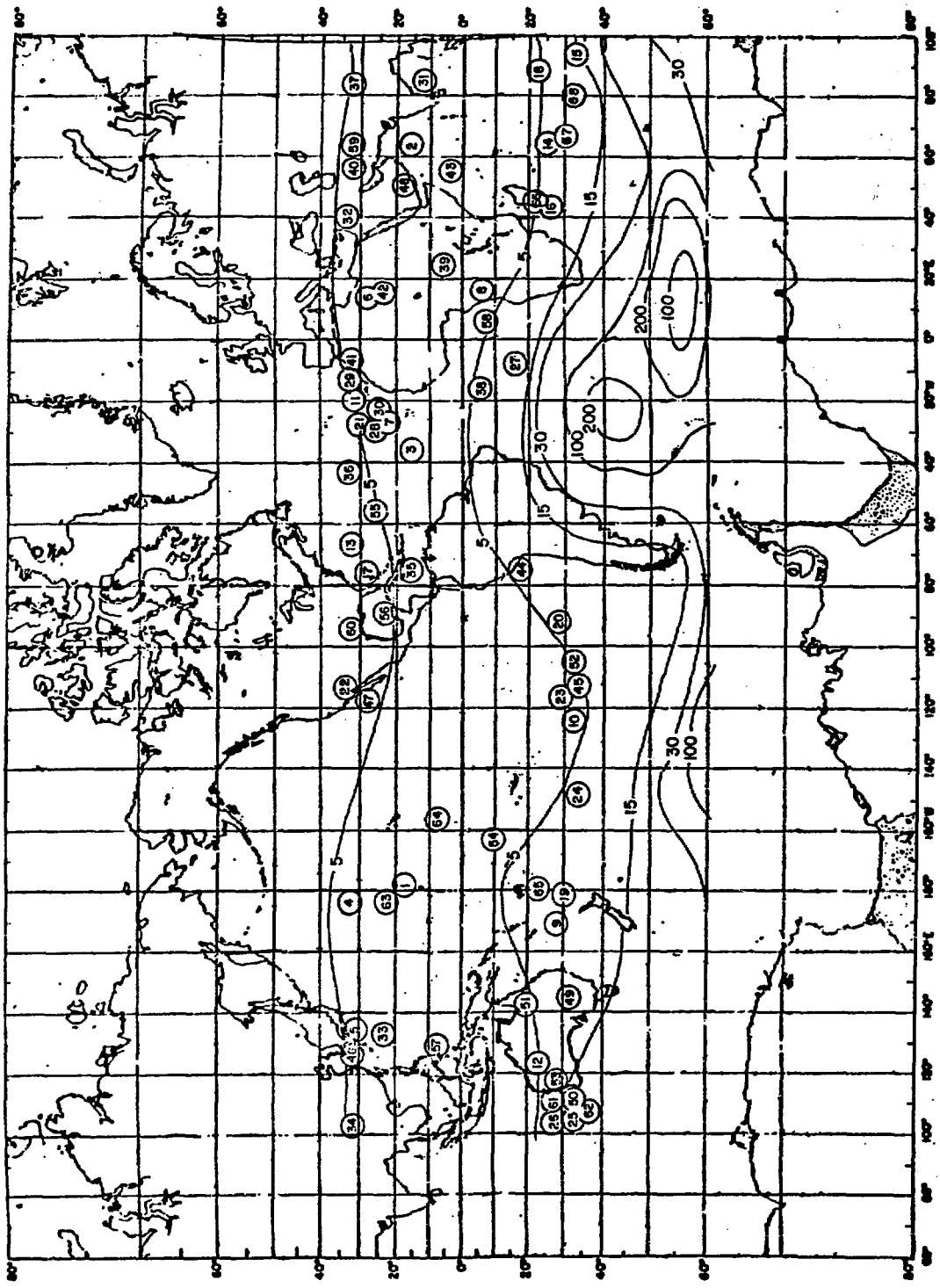
5
15
30
100
200

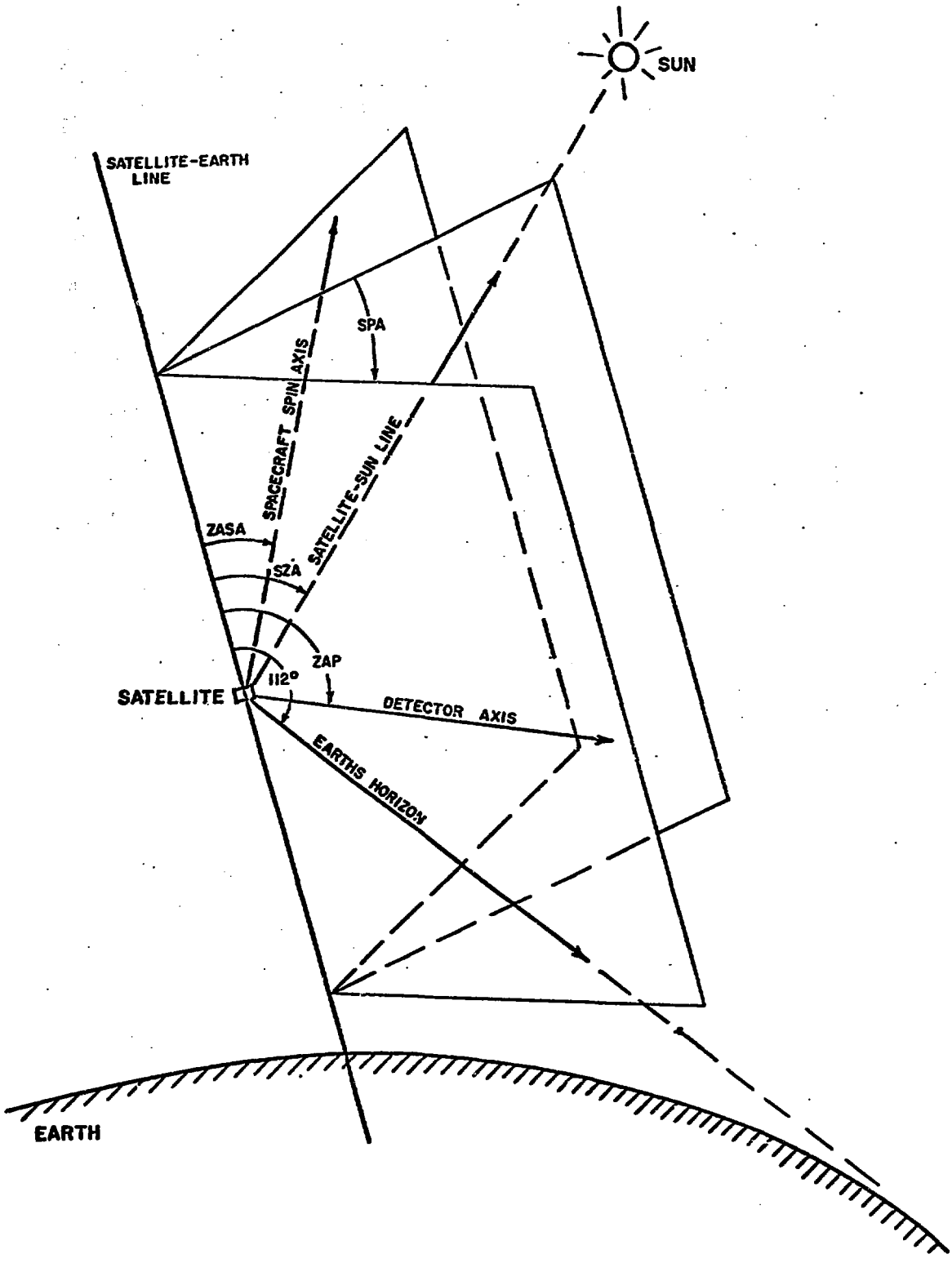

Fig. 34. Definition of Angles Used to Determine OSO-6 Neutron Detector Pointing Direction.

EVENT	TYPE	CODE	DAY	TIME	D/A	ENERGY	LAT	LON	SZA	SPA	ZAP	ZASA	GRD	ID	AZ	C1	C2	DE	E	ORBIT	FLARE	EFF
1	1	0	28	4.138	DA	72.73	17.97	180.60	68.78	6.20	67.04	145.95	32	2	25	3	8	13	13	2607	-	-
2	1	0	28	12.056	DA	67.34	16.74	61.79	68.11	11.95	74.70	146.53	31	2	22	13	20	18	9	2613	2	8.90E-04
3	1	0	28	18.367	DA	62.18	18.31	322.14	64.73	12.15	60.10	141.62	30	2	26	3	8	17	11	2617	2	8.90E-04
4	1	0	29	0.484	DA	42.01	32.71	177.15	50.82	30.12	20.12	92.12	41	2	29	3	5	19	7	2620	3	3.00E-04
5	1	0	29	3.656	DA	112.51	32.52	131.15	50.65	23.92	74.57	93.48	42	2	20	3	18	11	18	2622	3	3.30E-04
6	1	0	31	7.684	DA	43.53	29.01	13.13	70.53	54.11	43.89	46.09	36	2	33	3	8	20	7	2655	-	-
7	1	0	31	15.919	DA	51.12	21.23	331.52	46.78	23.92	67.47	116.62	28	2	20	7	20	20	6	2661	4	5.70E-04
8	1	0	31	16.155	DA	80.01	-6.70	15.15	72.90	24.12	76.96	163.08	32	2	28	3	10	14	14	2661	4	5.80E-04
9	1	0	42	3.794	DA	78.37	-28.26	169.31	41.94	24.14	53.54	131.03	51	2	25	20	24	17	9	2819	5	5.80E-04
10	1	0	43	2.119	DA	57.40	-31.93	237.17	78.90	6.06	78.36	158.79	37	2	23	3	10	16	10	2833	7	9.00E-04
11	1	0	43	7.687	DA	54.61	30.62	339.98	95.53	6.06	96.08	19.06	40	2	23	3	17	24	8	2838	8	9.00E-04
12	1	0	60	3.769	DA	80.83	-22.97	120.46	16.28	30.11	45.85	85.59	30	2	29	3	12	13	14	3093	11	4.90E-04
13	1	0	90	9.942	DA	118.57	32.85	290.84	97.06	1.17	95.95	23.87	73	2	24	3	16	11	17	3553	-	-
14	1	0	90	10.598	DA	59.14	-26.11	65.26	51.55	24.13	66.03	134.50	54	2	28	16	24	21	4	3553	-	-
15	1	0	90	10.714	DA	44.33	-32.45	92.99	77.72	6.01	76.48	153.77	67	2	23	3	5	24	6	3553	-	-
16	1	0	90	12.180	DA	61.73	-26.21	41.33	51.46	12.16	58.74	134.31	45	2	26	3	20	21	8	3554	-	-
17	1	0	96	9.912	DA	53.63	29.27	282.87	103.24	6.13	100.63	22.86	65	2	25	3	17	19	7	3644	-	-
18	1	0	96	12.389	DA	81.03	-20.88	88.75	95.94	11.92	94.96	170.71	50	2	22	3	15	16	12	3645	-	-
19	1	0	104	20.788	DA	77.03	-29.63	178.87	61.49	35.90	35.15	60.37	49	2	18	19	22	16	8	3771	-	-
20	1	0	105	14.152	DA	41.91	-28.27	267.86	69.15	0.62	68.84	53.00	34	2	24	3	3	19	6	3782	24	6.70E-04
21	1	0	128	11.358	DA	67.39	30.36	330.61	37.15	17.92	48.04	59.19	44	2	21	3	20	21	9	4130	25	8.00E-04
22	1	0	128	17.723	DA	79.00	32.15	244.34	30.09	48.11	35.31	67.18	54	2	32	18	24	19	8	4134	25	2.00E-04
23	1	0	149	18.522	DA	52.67	-29.73	242.07	54.64	59.90	12.27	78.75	42	2	14	3	24	22	5	4453	-	-
24	1	0	149	21.754	DA	71.30	-32.61	211.47	54.28	0.73	54.45	94.33	41	2	24	14	24	23	7	4455	-	-
25	1	0	150	5.711	DA	40.79	-32.82	105.07	55.61	59.90	16.87	105.33	69	2	14	3	3	27	5	4461	26	0.20E-04
26	1	0	150	7.381	DA	47.09	-29.39	103.24	61.04	5.94	57.20	125.48	64	2	23	3	23	22	4	4462	26	7.40E-04
27	1	0	164	16.327	DA	75.21	25.49	331.23	32.92	12.13	37.07	122.92	35	2	26	3	23	16	10	4680	29	8.15E-04
28	1	0	164	18.063	DA	42.55	32.93	344.60	66.01	5.96	67.85	154.97	40	2	23	3	8	27	5	4681	29	6.30E-04
29	1	0	164	19.695	DA	46.67	32.44	333.76	77.16	30.11	74.11	163.21	44	2	29	3	16	26	5	4683	29	3.80E-04
30	1	0	165	6.414	DA	43.35	11.74	86.99	11.90	0.88	11.98	89.62	37	2	24	3	3	23	6	4689	30	6.70E-04
31	1	0	165	14.631	DA	50.23	32.85	37.94	67.50	0.88	68.35	156.14	31	2	24	3	26	21	4	4694	32	8.30E-04
32	1	0	166	4.653	DA	40.24	24.44	132.41	20.26	30.11	39.20	110.21	36	2	29	3	20	24	3	4703	33	3.00E-04
33	1	0	166	11.241	DA	50.53	30.60	101.30	78.27	5.96	80.24	164.64	31	2	23	5	25	28	3	4707	34	8.35E-04
34	1	0	166	17.227	DA	49.04	17.95	285.44	6.41	35.91	29.84	92.05	43	2	18	3	25	21	4	4712	36	4.00E-04
35	1	0	166	19.052	DA	41.83	32.96	318.05	56.20	5.96	57.99	145.84	56	2	23	3	22	23	3	4713	36	6.30E-04
36	1	0	167	9.203	DA	66.54	31.70	83.22	37.20	48.11	56.03	127.37	41	2	32	3	24	22	8	4721	38	2.00E-04
37	1	0	167	10.408	DA	58.08	-5.88	343.35	49.29	5.96	47.30	42.81	83	2	23	3	20	24	7	4722	38	9.30E-04
38	1	0	176	4.636	DA	44.02	7.41	25.43	83.07	24.12	75.02	20.51	44	2	28	3	12	26	5	4855	-	-
39	1	0	176	6.473	DA	49.07	31.32	55.53	25.99	6.17	21.87	70.15	39	2	25	3	26	24	5	4856	-	-
40	1	0	176	11.252	DA	53.50	32.59	352.88	19.04	18.12	12.54	77.52	37	2	27	3	20	24	6	4860	40	7.90E-04
41	1	0	176	13.024	DA	51.47	26.13	16.28	28.25	35.91	44.33	118.61	32	2	18	3	27	21	4	4861	40	3.60E-04
42	1	0	176	13.226	DA	78.49	4.21	55.87	73.36	5.98	72.68	156.93	28	2	23	15	22	17	9	4861	40	7.70E-04
43	1	0	201	18.673	DA	53.22	-32.96	245.54	55.72	12.13	67.09	75.98	41	2	26	3	5	21	8	5243	42	8.45E-04
44	1	0	213	7.815	DA	79.04	31.89	126.34	57.11	24.12	58.97	147.11	43	2	28	10	19	17	10	5419	-	-
45	1	0	226	19.756	DA	136.06	30.46	249.04	16.60	42.11	28.39	97.76	56	2	31	3	14	9	19	5624	47	1.85E-04
46	1	0	227	3.327	DA	59.97	19.34	51.01	76.31	30.11	62.20	33.57	29	2	29	14	25	29	3	5629	47	5.55E-04
47	1	0	301	15.846	DA	53.53	-31.76	253.92	44.60	17.91	40.87	48.36	40	2	21	10	22	25	3	6761	49	7.30E-04
48	1	0	297	1.307	DA	41.99	-31.12	141.76	23.83	30.11	49.51	73.62	67	2	29	3	9	21	5	6692	-	-
49	1	0	297	4.522	DA	56.82	-32.75	106.57	21.22	0.60	21.16	84.41	72	2	24	3	3	15	9	6694	-	-
50	1	0	297	6.361	DA	43.99	-19.45	142.82	60.16	18.11	70.16	140.13	37	2	27	3	17	22	4	6695	48	5.60E-04
51	1	0	309	0.873	DA	42.66	-27.46	118.02	43.06	30.11	51.33	47.15	52	2	29	3	4	17	6	6874	50	3.00E-04
52	1	0	319	16.774	DA	51.60	-10.41	197.74	83.67	12.12	81.10	11.79	25	2	26	3	20	22	5	7036	52	7.70E-04
53	1	0	320	13.607	DA	42.28	26.08	304.32	52.29	60.10	12.71	79.96	52	2	34	3	3	17	6	7049	56	0.80E-04
54	1	0	320	21.862	DA	40.48	21.76	270.99	73.54	24.11	71.01	160.15	48	2	28	3	18	22	3	7054	56	3.75E-04
55	1	0	320	22.921	DA	119.44	8.72	126.43	70.59	29.91	88.89	40.39	28	2	19	3	14	12	17	7055	56	2.65E-04
56	1	0	321	5.092	DA	40.47	-7.99	5.80	91.21	11.92	92.70	10.54	47	2	22	3	3	24	5	7059	57	5.40E-04
57	1	0	321	7.073	DA	51.37	31.99	62.37	51.43	6.13	45.58	98.99	38	2	25	3	24	20	4	7060	57	8.35E-04
58	1	0	321	16.498	DA	39.90	29.67	265.20	55.67	17.91	71.43	85.21	59	2	21	3	17	23	3	7066	58	4.55E-04
59	1	0	338	7.038	DA	44.60	-29.85	105.23	30.79	35.91	38.80	119.42	66	2	18	3	18	21	4	7319	-	-
60	1	0	338	8.715	DA	77.84	-32.93	104.48	51.66	24.11	63.82	137.17	72	2	28	9	16	18	10	7320	-	-
61	1	0	338	19.195	DA	39.47	21.77	178.90	81.76	5.95	83.49	25.18	34	2	23	3	17	22	3	7326	59	6.30E-04
62	1	0	338	19.310	DA	42.66	8.68	201.54	54.95	5.95	56.97	42.39	34	2	23	3	20	22	3	7327	59	6.30E-04
63	1	0	346	1.136	DA	42.28	-24.16	179.94	44.19	30.11	58.97	138.42	36	2	29	3	3	17	6	7438	60	3.00E-04
64	1	0	346	5.929	DA	39.38	-23.37	42.75	42.75	18.12	46.64	47.82	45	2	27	3	3	20	4	7440	-	-
65	1	0	346	6.012	DA	68.75	-30.06	62.84	23.70	18.12	33.22	67.88	57	2	27	3	12	19	10	7440	60	8.00E-04
66	1	0	346	7.755	DA	49.05	-31.82	79.90	18.11	41.91	34.01	104.66	71	2	17	3	6	20	7	7441	60	2.50E-04
67	1	0	347	6.031	DA	51.63	15.98	158.89	74.93	53.91	39.80	125.63	33	2	15	3	6	20	9	7607	-	-
68	1	0	347	9.989	DA	78.63	-16.07	272.48	105.89	6.18	100.43	54.06	35	2	25	15	20	16	10	7609	-	-
69	1	0	347	17.165	DA	90.54	22.61	356.24	86.61	0.99	87.30	128.59	30	2	24	3	3	14	16	7614	61	5.30E-04
70	1	0	347	18.064	DA	41.85	-30.65	188.54	69.01	11.94	77.82	54.13	49	2	22	3	21	22	4	7614	61	5.40E-04

Fig. 35. Summary of Total Forward Solar Neutron Events.

Only two white flares occurred during the period August 1969 - December 1970. Furthermore, only three outstanding solar proton flares occurred during the period January 1970 - December 1970. I have noted a fourth proton event from a paper by McLean et al. [1971]. The above white-light flares and solar proton events are listed in Appendix 2 and Appendix 3, respectively. Figure 36 shows the heliographic coordinates of the 60 optical solar flares which are numbered for reference. Note that the flares tend to occur in the sunspot zones parallel to the equator. In Figure 33 is shown the location of the OSO-G spacecraft for the selected solar neutron events. Note that the selected neutron events do lie outside the high count rate boundaries of the South Atlantic anomaly.

From the summary of Figure 35, plots of ZAP versus SZA, ZAP versus proton-recoil energy, SPA versus SZA, and SPA versus ZAP are given in Figure 37. Also plots of dE versus E, dE versus C2, and C2 versus C1 are depicted in Figure 38. Comparing this figure to Figure 17, note gain change in the E counter. In Figure 39 plots for a portion of the quick-look charged particle data of orbit 414 (69-09-05) are shown.

In order to estimate the efficiency, ϵ, for a particular neutron event, we need to know the incident neutron angle, SPA, and the incident neutron energy, E_n. SPA is given in the data while E_n we can get from

$$E_p = E_n \cos^2\psi \quad , \tag{40}$$

which is the nonrelativistic formula relating the proton recoil energy, E_p, and E_n. The relativistic formula is

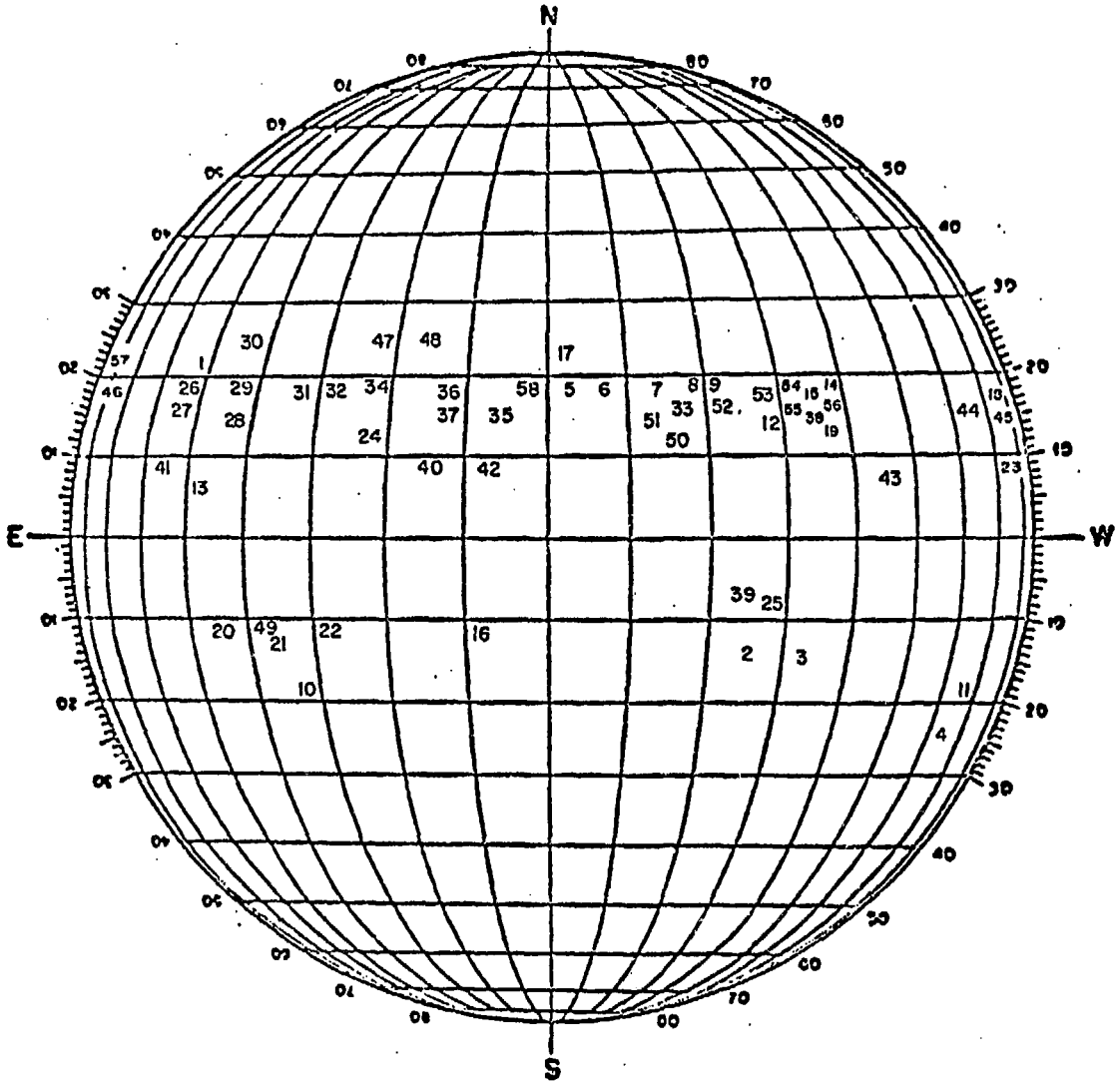

Fig. 36. Heliographic Coordinates of the 60 Optical Solar Flares.

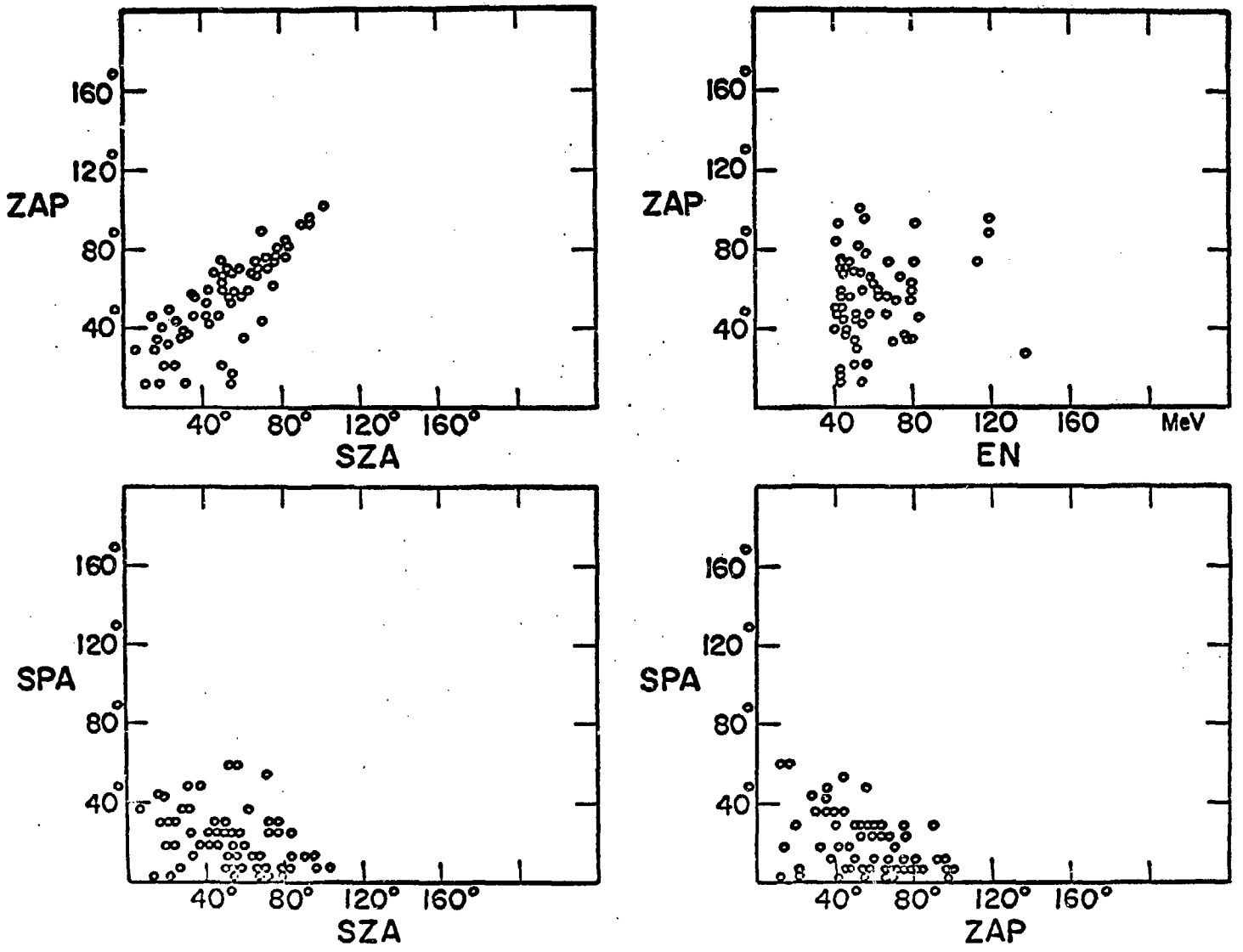

Fig. 37. Plots of ZAP versus SZA, ZAP versus Proton-Recoil Energy, SPA versus SZA, and SPA versus ZAP for Solar Neutrons, January-December 1970.

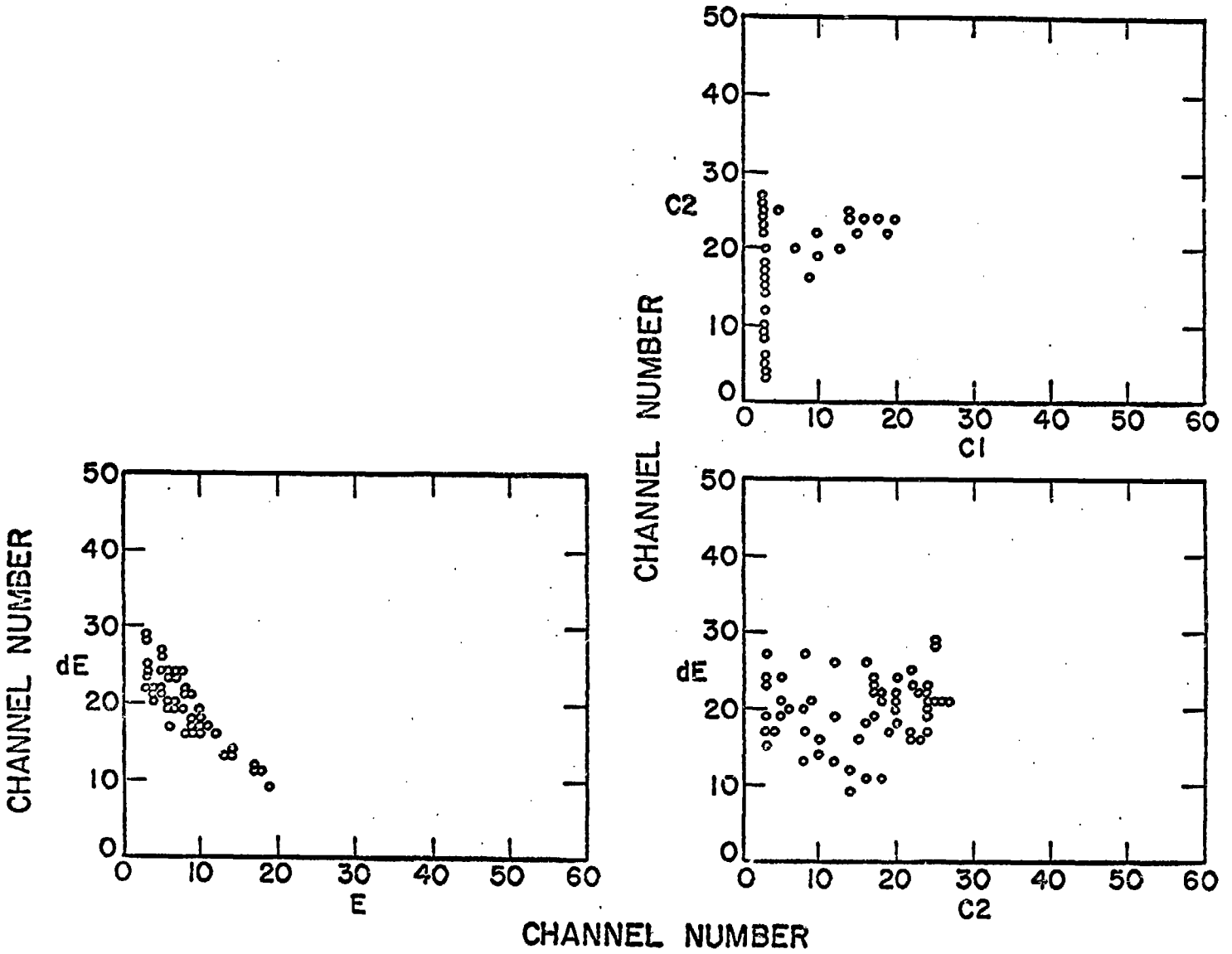

Fig. 38. Plots of dE versus E, dE versus C2, and C2 versus C1 for Solar Neutron Data, January-December 1970.

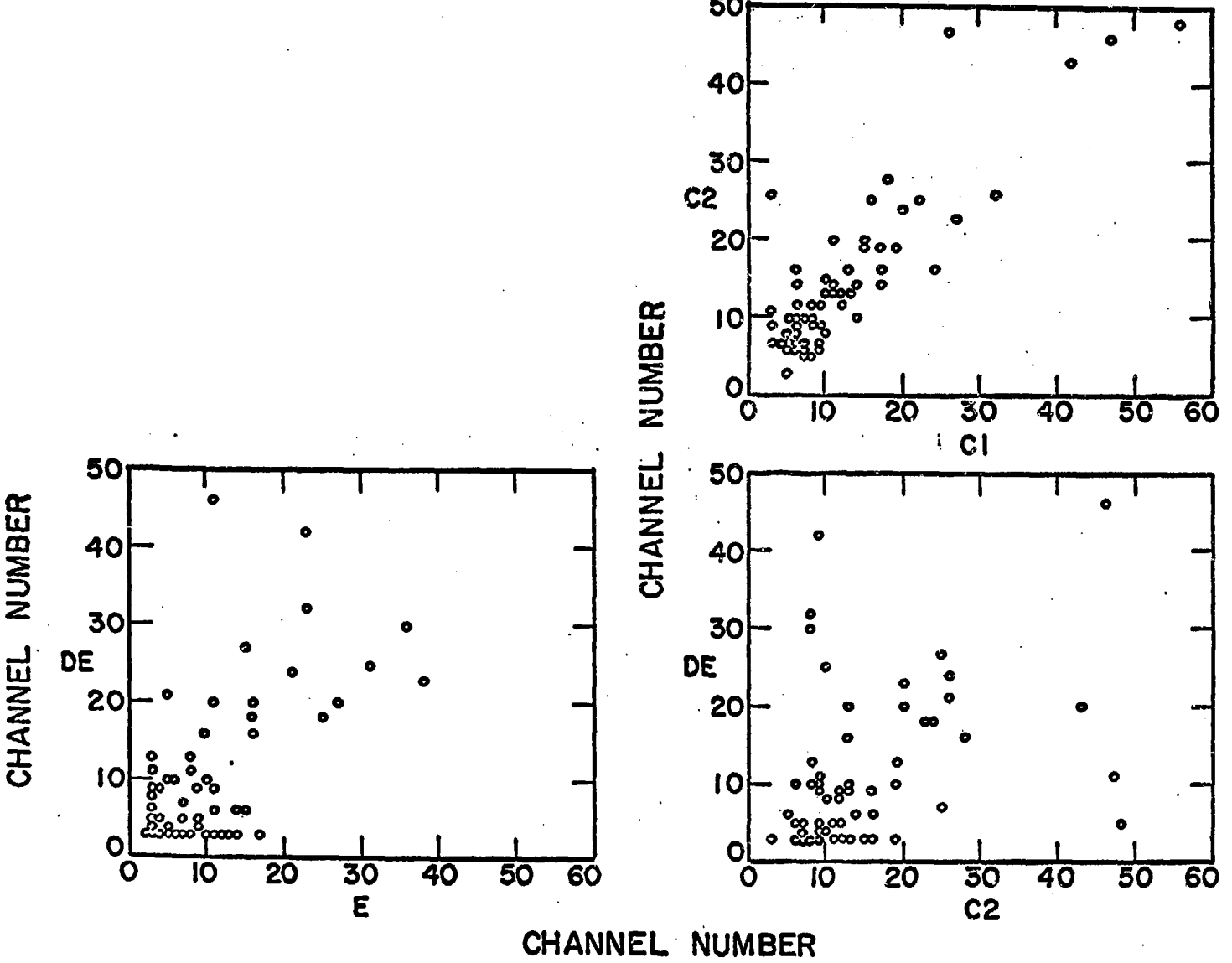

Fig. 39. Plots of dE versus E, dE versus C2, and C2 versus C1 of Portion of Quick-Look Charged Particle Data, Orbit 414 (69/09/05).

$$E_n = \frac{E_p \cos^2\psi}{1 + \frac{E_n \sin^2\psi}{2M_n c^2}} \quad . \tag{41}$$

To estimate the error in using Eq. (40) instead of Eq. (41), assume $\psi = 16°$ and $E_p = 150$ MeV. The error is 0.6% (0.8%) for $E_p = 150$ MeV (200 MeV), respectively. I have used Eq. (40) in calculating ε. Although

$$\cos\theta_p = \cos\theta\cos\psi - \sin\theta\sin\psi\cos\phi \quad ,$$

where ψ is the neutron-proton scattering angle, θ is the incident neutron angle, and ϕ is the proton recoil azimuthal scattering angle (see Figure 40), an average value of $\psi = 16°$ was assumed since an approximate range of ψ was between 0° and 32°. Assuming average value of $\phi = \pi$ and solving for $\cos\psi$, one gets

$$\cos\psi = \cos\theta_p\cos\theta + \sin\theta\sin\theta_p \quad . \tag{42}$$

Figure 41 shows a plot of solar phase angle (SPA versus incident neutron energy. The average energy and SPA for these events was 62.83 MeV and 20.89°, respectively. Note the angular quantization at 6° intervals in Figure 41.

To calculate the neutron flux for each flare the following steps were followed. (1) Efficiency was calculated for each neutron event. (2) An average efficiency per flare was next calculated since a flare may have had more than one neutron event. Then the following expression was used to calculate the neutron flux per flare,

$$\Phi = \frac{N}{A\varepsilon t}\left(\frac{180}{\theta}\right) \pm 55\% \quad , \tag{43}$$

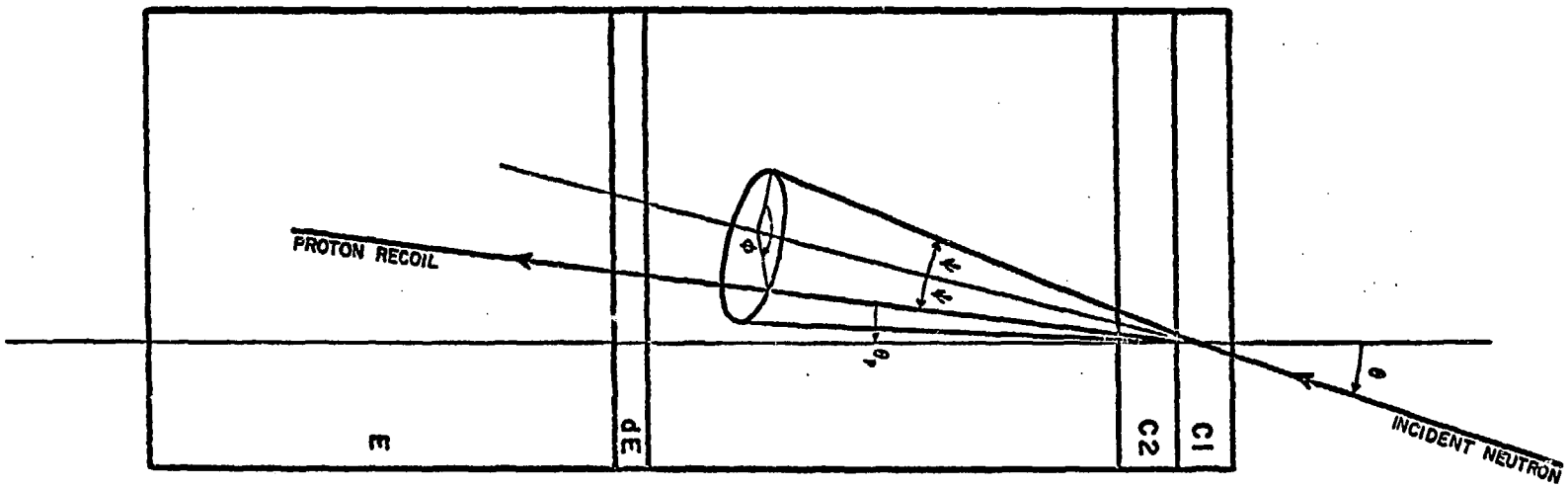

Fig. 40. Definition of Neutron-Proton Scattering Angles.

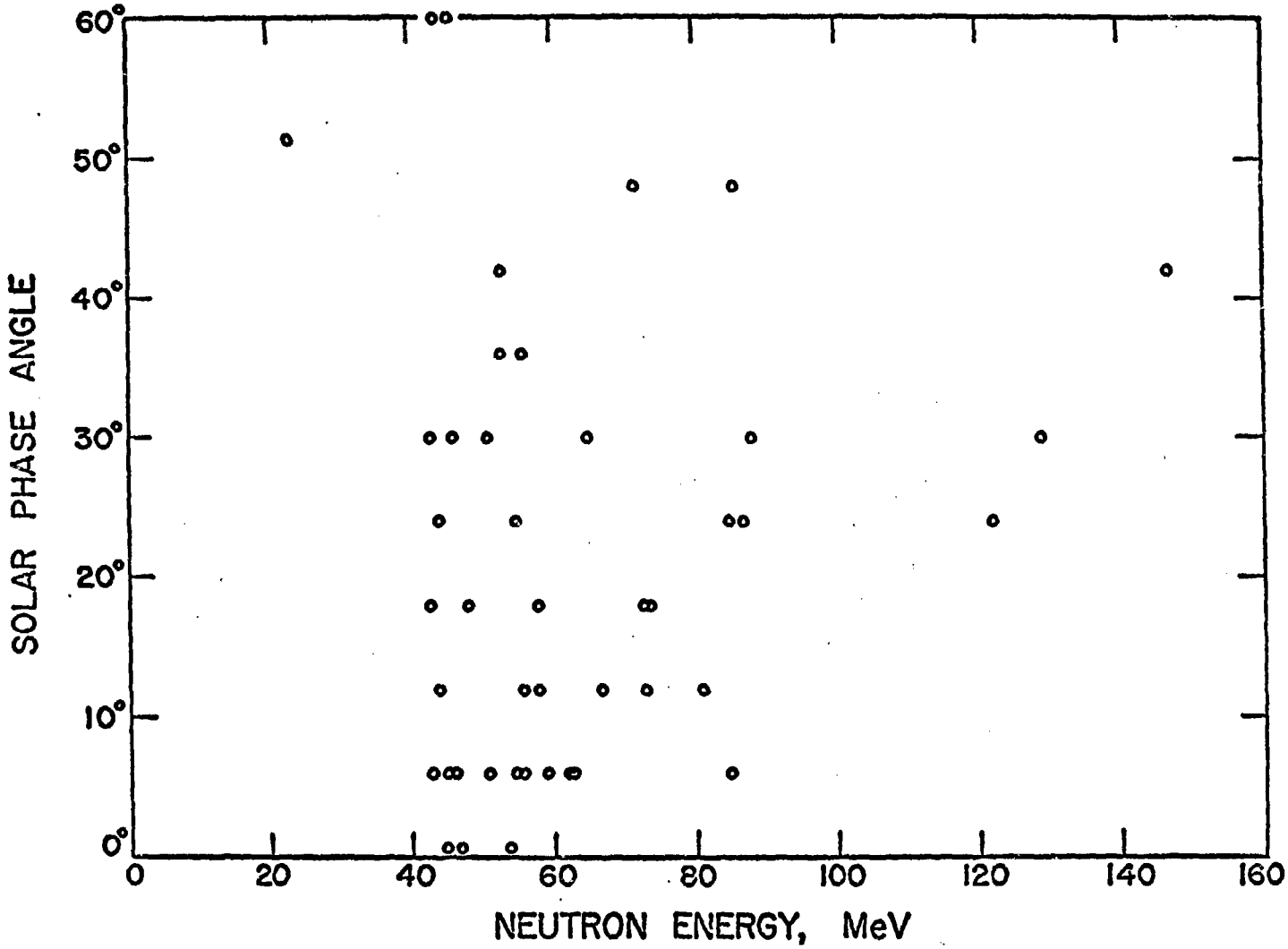

Fig. 41. Solar Phase Angle (SPA) versus Incident Neutron Energy, E_n, for Selected Neutron Events.

where N is the number of events per flare, A is the sensitive area of the detector, $\bar{\varepsilon}$ is the average efficiency per flare, t is the observation time per flare, and the $(\frac{180}{\theta})$, where θ = SPA, is a correction to account for a rotating detector. The error was estimated using average values for the various quantities in Eq. (43) and maximum errors for these average values. A (5±0.5)% correction, Leavitt [1971], was applied to Φ to account for data dropouts. Figure 42 gives the summary of the solar flare computer runs. The occurrence of each neutron count considered in this study is indicated, together with the selected flare. Table 11 lists the neutron fluxes as calculated from Eq. (43). Of the 60 flares 31 produced no neutron events, and the average neutron flux for the 60 flares was 0.461×10^{-2} neutrons/cm^2 sec, with ±55% error.

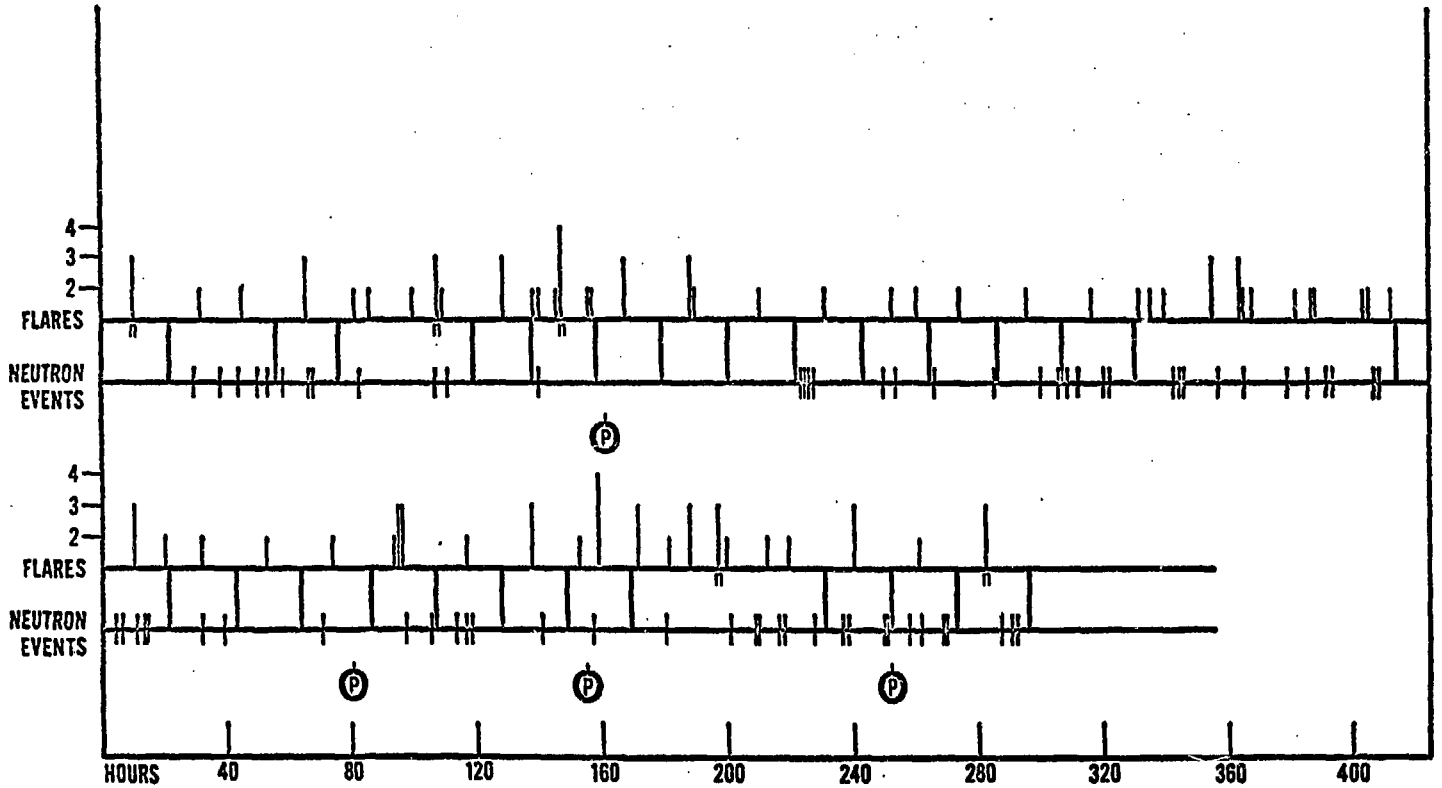

Fig. 42. Summary of Solar Flare Computer Runs (1970). Computer runs are shown in contiguous blocks of time, the lower sequence being a continuation of the upper sequence. The occurrence of each neutron count considered in this study is indicated, together with the selected flares. The importance of each flare is given by the height of the corresponding line. The times of the four proton events are also indicated.

TABLE 11

SOLAR NEUTRON FLUX VALUES

1.	3N	---	31.	3B	---
2.	2B	0.552×10^{-2} n/cm^{2}sec	32.	2B	1.393
3.	2B	0.959	33.	2B	0.715
4.	3B	0.723	34.	2B	0.715
5.	2B	1.113	35.	2B	---
6.	2B	---	36.	2B	0.760
7.	2B	0.407	37.	2B	---
8.	3N	1.566	38.	2B	1.574
9.	2B	---	39.	2B	---
10.	3B	---	40.	3B	1.448
11.	2B	2.832	41.	2B	---
12.	2B	---	42.	2B	0.181
13.	2B	---	43.	2B	---
14.	4N	---	44.	2B	---
15.	2B	---	45.	2B	---proton event
16.	2B	---	46.	3B	---
17.	3B	---proton event	47.	3B	0.814
18.	3B	---	48.	2B	0.272
19.	2B	---	49.	3B	0.280
20.	2B	---	50.	2B	0.184
21.	2B	---	51.	4B	---proton event
22.	2B	---	52.	3B	0.416
23.	2B	---	53.	2B	---
24.	2B	0.235	54.	3B	---
25.	2B	0.595	55.	3N	---
26.	2B	1.168	56.	2B	3.302
27.	2B	---	57.	2B	1.439
28.	2B	---	58.	2B	0.343
29.	2B	1.023	59.	3B	0.461
30.	3B	0.579	60.	3N	1.612 proton event

VI. CONCLUSIONS

A. Summary and Conclusions

A summary of neutron fluxes calculated theoretically by Lingenfelter [1969], Lingenfelter and Ramaty [1967], Svestka [1971], and Hess [1963], and an experimental value from the OSO-6 solar neutron measurement is given in Table 12. As noted in Table 11 and Table 12 the predicted values by the first three authors are 2-3 orders of magnitude higher than the OSO-6 average flux. In Table 11 , neutron events are plotted for each computer run period in sequence to show the time distribution of neutron events for each flare period selected. Each period plotted covers the flare duration plus a ten-hour period after flare termination, except where there is overlap. Flares 4 and 32 contained neutron events that occurred within 60 minutes after the occurrence of the flare. This result is disturbing. Neutron fluxes associated with flares 4 and 32 were compared to Lingenfelter's calculation. Typical neutron arrival times at the earth assumed in Lingenfelter's work are from 10 - 60 minutes. The lack of significant neutron fluxes during the occurrence of the major proton events and the 4B, 4N flares in Table 11 should be noted. Flares 5, 11, 30 and 48 are associated with neutron events that occurred within time intervals of 1 - 2 hours following the occurrence of a flare. The following indicates the temporal distribution between neutron events and optical flares.

TABLE 12

SOLAR NEUTRON FLUXES

Theory				Experiment
Lingenfelter (1969)	Lingenfelter & Ramaty (1967)	Svestka (1971)	Hess (1963)	OSO-G (1971)
$2n/cm^2$ sec	30-70 n/cm^2 sec	$3n/cm^2$ sec	$6x10^{-2} n/cm^2$ sec	$(.723\pm.398)x10^{-2}$ n/cm^2 sec
CLASS 3 FLARE	3B FLARE	3B FLARE	DD REACTION	3B FLARE

Time Interval	Flare Number
0-1 hours	4, 32
1-2	5, 11, 30, 48
2-3	8, 38, 49
3-4	34, 42, 50
4-5	26, 29, 36, 40, 57
5-6	7, 47
6-12	2, 3, 24, 25, 33, 52, 56, 58, 59, 60

Excluding zero fluxes a neutron event occurred on the average 5.55 hours following the occurrence of an optical flare. There is an apparent correlation between the fluxes and the optical flares; this is in part due to the manner in which the flare data was selected. Since there exists a random temporal distribution of both flares and neutron events, the likelihood of a correlation is finite. A test for this hypothesis would be to plot the entire flare data and neutron flux for 1970.

Neutron production models other than that of Lingenfelter, Ramaty, and Svestka would have to be explored to help explain nearly all of the neutron fluxes in Figure 42. Independent evidence, Place [1972], suggests the possibility that the measured fluxes represent mainly a type of background; the firm conclusion is that the expected fluxes were not observed. Interpretation of the low fluxes observed requires a much greater level of effort than that undertaken here and indeed may not be possible given the limitations of the instrument. The experimental results suggest a serious problem in the theoretical solar neutron production models of Lingenfelter, Ramaty, and Svestka.

For most of the flares there probably does not exist a sufficient proton flux that is incident on the photosphere from the chromosphere. Even if proton fluxes sufficient to produce large fluxes of neutrons are incident on the photosphere, it is possible that because of anisotropy in the angular distribution of the neutron flux, only a small fraction of the neutrons produced propagate towards the earth. Since 59% of solar neutrons with energy at 200 MeV decay before reaching the earth, the number of neutrons would be further decreased.

In the white-light flare case, perhaps the anisotropic angular distribution argument applies also.

I have included Hess's flux which is due to thermonuclear neutrons produced in the corona. Although Hess's flux is in agreement with the UNM measurement, a mechanism is required to explain how these thermonuclear neutrons acquire high energies; for example, average solar neutron energy measured is around 60 MeV.

If it is true that solar protons are accelerated to high energies at 1-2 $R_\odot$, McLean et al. [1971], then it does seem unlikely that solar neutrons are produced in the solar photosphere. The UNM neutron measurement supports such a conclusion.

In Table 11 the correlation between solar neutron fluxes and optical solar flares is quite random. Let us show that the distribution of neutron fluxes describes a random process. Table 13 gives the distribution of neutron events in time to calculate χ^2. In interpreting the value of P one can say that if P lies between 0.1 and 0.9, the assumed distribution very probably corresponds to the observed one. If P is less than 0.02 or greater than 0.98, the assumed distribution

TABLE 13

DISTRIBUTION OF NEUTRON EVENTS IN TIME

Classification	t_1(hr)	t_2(hr)	n_{calc}	n_{obsv}	$n_{obs}-n_{calc}$	$\frac{(n_{obs}-n_{calc})^2}{n_{calc}}$
1	0	1	6.12	5	-1.12	0.210
2	1	5	19.38	19	-0.38	0.008
3	5	10	15.79	17	+1.21	0.093
4	10	20	15.84	12	-3.84	0.931
5	20	30	6.08	9	+1.14	0.101
6	30	100	3.78	2		
7	100		0.005			

$\chi^2 = 1.343$ 3 degrees of freedom $0.7 < P < 0.8$

Average interval between events: 9.96 hours.

is extremely unlikely and is to be questioned seriously.

So in our case with $0.7 < P < 0.8$ in 7 to 8 out of 10 similar experiments, the deviations from the interval distribution (which rests on the Poisson distribution) would be greater than here observed. There is therefore strong support for the conclusion that the observed neutron fluxes are consistent with the interval distribution as expressed by

$$n = N \int_{t_1}^{t_2} a\, e^{-at}\, dt \,, \tag{44}$$

$$n = N \left(e^{-at_1} - e^{-at_2}\right) \,, \tag{45}$$

which describes a random process and where N is the total number of intervals and a is the average number of events per unit time.

A similar test was made on the distribution of flares and $0.3 < P < 0.5$ was obtained which implies these phenomena also are consistent with a random process.

In Table 14 is a listing of experimental work that has been done using various experimental methods for measuring solar neutron fluxes. Although all the measurements were at balloon altitudes, except for Ro [1971], this study results in a flux that is consistent with most of the measured fluxes.

B. Future Analysis

In view of the low upper limits to the solar fluxes obtained in this experiment, further measurements at this level of sensitivity would not appear fruitful except possibly for corroboration.

TABLE 14

PREVIOUS EXPERIMENTAL WORK ON HIGH ENERGY SOLAR NEUTRONS

Investigator	Altitude	Detector Type	Energy Range MeV	Solar Neutron Flux
Apparao et al.(1966)	Balloon	Emulsion	20-160	$(4.65\pm1.9)\times10^{-2}$ n/cm^{2}sec
Webber & Ormes (1967)	Balloon	Cerenkov-Scintillator	>100	$\leq 0.24\times10^{-2}$ n/cm^{2}sec
Wolcott (1968)	Balloon	Scintillator	20-200	$(0.28-0.34)\times10^{-2}$ n/cm^{2}sec
Kim (1968)	Balloon	Emulsion	20-100	2.8×10^{-2} n/cm^{2}sec
Zych & Frye (1969)	Balloon	Spark Chamber	18-25	1.7×10^{-2} n/cm^{2}sec
			39-55	1.0×10^{-2} n/cm^{2}sec
Forrest & Chupp (1969)	Balloon	Scintillator	20-120	4.0×10^{-2} n/cm^{2}sec
Daniel et al.(1969)	Balloon	Scintillator	15-150	1.2×10^{-2} n/cm^{2}sec
Cortellessa et al. (1971)	Balloon	Scintillator	10-200	0.55×10^{-2} n/cm^{2}sec
Heidbreder et al. (1970)	Balloon	Spark Chamber	100-400	0.125×10^{-2} n/cm^{2}sec
Ro (1971)	Satellite	Scintillator	20-200	$(0.08\pm0.04)\times10^{-2}$ n/cm^{2}sec
Daniel et al.(1967)	Balloon	Spark Chamber	50-500	10.0×10^{-2} n/cm^{2}sec
Daniel et al.(1971)	Balloon	Scintillator	50-500	1.5×10^{-2} n/cm^{2}sec

Since the low neutron fluxes indicate that nuclear interactions of any flare-accelerated protons produced during the selected events do not play a major role in flare phenomena, it is possible that experiments with greatly increased sensitivity would not shed much light on the flare mechanisms. On the other hand a quantitative estimate of the flux of protons impinging on the solar photosphere could indicate something about the geometry of magnetic fields in particular flare events. In any case it appears that increases in detector sensitivities of many factors of ten would be required along with satellite orbits which approach the sun to pick up low energy neutrons.

APPENDIX 1

Environmental Conditions for Qualification and Acceptance Testing

1.0 SCOPE

This specification defines the qualification and acceptance test requirements and procedures for the University of New Mexico High Energy Neutron Detector Experiment (OSO-6) prototype, flight, and flight spare instruments.

2.0 APPLICABLE DOCUMENTS

The following documents of the issue listed form a part of this specification to the extent specified herein:

Document	Title	Revision
21625	Interface Drawing, Neutron Detector	Basic
X-623-65-73	Experiment OSO Experimenters Manual	June 1965 Oct. 1966
BBRC 29800	Experiment-Spacecraft Interface Specification	Rev. A
BBRC TN65-74	Environmental Test Parameters for Qualification Testing of OSO Experiments	Rev. A

3.0 TEST PREPARATION

3.1 Environmental Conditions - Qualification

The environmental conditions for qualification testing are as follows:

3.1.1 Vibration, sine

Axis	Range (Hertz)	g (0 to peak)	Rate
Thrust	5-10.5	0.35" D.A.	)
z-z	10.5-40	6	)
	40-70	9	)
	70-125	18	) 2 oct/min
	125-250	9	)
	250-2000	7.5	)
Lateral	5-10.5	0.35" D.A.	)
x-x and y-y	10.5-24	3	)
	24-40	9	) 2 oct/min
	40-100	6	)
	100-2000	7.5	)

3.1.2 Vibration, random

Axis	Range (Hertz	PSD Level g^2/cps	Acceleration g (rms)	Duration
All	20-2000	0.07	11.8	4 minutes each axis

3.1.3 Acceleration

Axis	Acceleration	Duration
Thrust z-z	12.9 g	3 minutes
Lateral x-x and y-y	(1.28 r) g	10 minutes each axis
About Thrust Axis	9.8 radians sec^{-2}	1.2 sec

Notes: r = distance from spacecraft center to instrument C.G. in feet (1.19 ft).

3.1.4 Temperature cycle

-3°C to +38°C (±2°C). The instrument shall operate for one hour at each extreme temperature. Three on/off cycles shall be made. The thermal rate of temperature change shall be $\leq 15°C \cdot hour^{-1}$ as measured on the detector package housing. The instrument shall be enclosed in a plastic bag to improve thermal uniformity and prevent water contained in the CO_2 from damaging the instrument.

3.1.5 Thermal vacuum

$-3°C \frac{(+2°C)}{(-4°C)}$ to $+38°C \frac{(+12°C)}{(-2°C)}$. The instrument shall operate for twelve hours at each extreme temperature. One on/off cycle shall be made. The vacuum shall be 1×10^{-5} Torr or less throughout the test. The thermal rate of temperature change shall be $\leq 15°C \cdot hour^{-1}$ as measured on the detector package housing.

3.2 Acceptance Environmental Conditions

The environmental conditions for acceptance testing are as follows:

3.2.1 Vibration, sine

Axis	Range (Hertz)	Acceleration (g,0 to peak)	Rate
Thrust	5-10.5	0.35" D.A.	)
z-z	10.5-40	4	)
	40-70	6	)
	70-125	12	) 4 oct/min
	125-250	6	)
	250-2000	5	)
Lateral	5-10.5	0.35" D.A.	)
x-x and y-y	10.5-24	2	)
	24-40	6	) 4 oct/min
	40-100	4	)
	100-2000	5	)

3.2.2 Vibration, random

Axis	Range (Hertz)	PSD Level g^2/cps	Acceleration g (rms)	Duration
All	20-2000	0.03	7.7	2 minutes each axis

3.2.3 Acceleration

Deleted.

3.2.4 Temperature cycle

Deleted.

3.2.5 Thermal vacuum

$+33°C\ \frac{(+2°C)}{(-0°C)}$ to $+2°C\ \frac{(+0°C)}{(-2°C)}$. The instrument shall operate for seventy-two hours minimum at each of the above temperatures, hot first. An additional hot cycle shall be made sufficient to demonstrate survival of the instrument. Between four to twelve hours in thermal equilibrium will be used. One on/off cycle shall be made. The vacuum shall be 1×10^{-5} Torr or less throughout the test. The thermal rate of change shall be $\leq 15°C \cdot hour^{-1}$ as measured on the detector package housing.

TABLE A1

SOLAR FLARE OBSERVATORIES

Computer Code No.	Obs. Type	I.A.U. Abbrev.	Name, Place and Country
824	C	ABST	Abastumani, Georgian SSR
512	VP	ARCE	Arcetri, Florence, Italy
521	VP	AROS	Arosa, Switzerland
508	VP	ATHN	Natl. Obs., Athens, Greece
832	C	BAKO	Bakou, Pirculi, USSR
647	VC	BOUL	Boulder, Colorado, USA
560	C	BUCA	Natl. Obs., Bucharest, Romania
557	VC	CANR	Gran Canaria, Canary Islands
151	C	CAPE	R.O.Capetown, Cape of Good Hope, South Africa
506	VP	CAPF	Anacapri, Italy (German)
519	V	CAPS	Anacapri, Italy (Swedish)
570	VP	CATA	Catania, Sicily, Italy
826	C	CRIM	Simeis, Crimea, USSR
403	VC	CRON	Carnarvon, Australia
402	VC	CULG	Culgoora, Australia
478	C	HALE	Haleakala, Maui, Hawaii, USA
537	VP	HERS	R.Greenwich Obs., Herstmonceux, England
646	C	HOUT	Houston, Texas, USA
563	C	HTPR	Haute-Provence, France
718	C	HUAN	Geophysical Inst., Huancayo, Peru
517	V	HURB	Hurbanovo, Czechoslovakia
313	V	IKOM	Ikomasan Obs., Kyoto, Japan
358	V	ISTA	Univ. Obs., Istanboul, Turkey
382	VP	KAND	Kandilli Obs., Istanboul, Turkey
547	V	KANZ	Graz Obs., Kanzelhohe, Austria
827	VP	KHAR	Kharkov, Ukranian SSR
828	C	KIEV	Kiev, Gao, Ukranian SSR
309	VP	KODA	Kodaikanal, India
522	VP	LOCA	Locarno, Switzerland
659	C	LOCK	Lockheed, Los Angeles, California, USA
876	VP	LVOV	Lvov, Ukranian SSR
468	VC	MANI	Manila, Philippines
642	C	MCMA	McMath-Hulbert, Pontiac, Michigan, USA
505	C	MEUD	Meudon, France
314	C	MITK	Mitaka, Tokyo, Japan
555	C	MONT	Monte Mario Obs., Rome, Italy
515		NERA	Nederhorst Den Berg, Netherlands
504	V	ONDR	Ondrejov, Prague, Czechoslovakia
476	VC	PALE	Palehua, Hawaii, USA
648	VC	RAMY	Ramey Solar Obs., Ramey AFB, Puerto Rico
645	C	SACP	Sacramento Peak, Sunspot, New Mexico, USA
572	VP	SALO	Salonique (Thessalonika) Greece
520	V	SALT	Saltsjobaden, Stockholm, Sweden
758	C	SANM	San Miguel, Argentina

TABLE A1 (cont.)

Computer Code No.	Obs. Type	I.A.U. Abbrev.	Name, Place and Country
862	VP	SIBE	Siberie (Siberian Ismir), Irkutsk, USSR
833	C	TACH	Tachkent, Uzbeck SSR
341	VP	TEHR	Tehran, Iran
342	C	TELV	Tel-Aviv, Israel
556	C	TORT	Tortosa, Spain
502	C	UCCL	Uccle Royal Obs., Brussels, Belgium
834	C	VORO	Voroshilov, USSR
546	VP	WEND	Wendelstein, GFR
523	VP	ZURI	Fidgenossische Sternwarte, Zurich, Switzerland

TABLE A2

EXPLANATION OF NOTATION USED IN APPENDIX 2.

A = Eruptive prominence, base at $> 90°$.
B = Probably the end of a more important flare.
C = Invisible 10 minutes before.
D = Brilliant point.
E = Two or more brilliant points.
F = Several eruptive centers.
G = No spots visible in the neighborhood.
H = Flare with high velocity dark surge.
I = Very extensive active region.
J = Plage with flare shows marked intensity variations.
K = Several intensity maxima.
L = Filaments show effects of sudden activation.
M = White-light flare.
N = Continuous spectrum shows effects of polarization.
O = Observations have been made in the calcium II lines H or K.
P = Flare shows helium D_3 in emission.
Q = Flare shows the Balmer continuum in emission.
R = Marked asymmetry in H_α line.
S = Brightening follows disappearance of filament (same position).
T = Region active all day.
U = Close and somewhat parallel bright filaments (|| or Y shape).
V = Occurrence of an explosive phase.
W = Great increase in area after time of maximum intensity.
X = Unusually wide H_α emission.
Y = Onset of a system of loop-type prominences.
Z = Major sunspot umbra covered by flare.

The following symbols are used in the table to explain accuracy of the times reported:

D = greater than
E = less than
U = approximate

All times are Universal Time (UT or GCT).

TABLE A2 (cont.)

The no-flare patrol observations matching the solar flare table are given in graphical form. The observatories reporting the patrols are indicated. The dark areas at the bottom half of each day are times of no cinematographic patrol. The dark areas at the top half of the day are times of neither visual nor cinematographic patrol.

The dual importance scheme used which was adopted 1 January 1966 by IAU Commission 10 is summarized in the following table:

"Corrected" area in square degrees	Relative Intensity Evaluation Faint(f)	Normal(n)	Brilliant(b)
< 2.0	Sf	Sn	Sb
2.1- 5.1	1f	1n	1b
5.2-12.4	2f	2n	2b
12.5-24.7	3f	3n	3b
> 24.7	4f	4n	4b

The area to be used in assigning the first figure of the dual importance is the area of the flaring region at the time of maximum brightness. The observatory measures apparent area in millionths of the solar disk. For flares less than 65° from the center of the solar disk, the formula relating apparent and corrected area is:

$$\text{"corrected" area} = \frac{\text{apparent area}}{97} \times \sec\theta$$

where apparent area is in millionths of the disk and corrected area is in heliographic square degrees.

For flares more than 65° from the center, the "sec θ law" becomes unsatisfactory. The first importance figure can be estimated from the table below where areas are given in millionths of the disk.

Angle	0	-----	65°	70°	80°	90°
Limit S-1	200	sec θ law	90	75	50	45
Limit 1-2	500	sec θ law	280	240	180	170
Limit 2-3	1200	sec θ law	600	500	350	300

The intensity scale shown as the second importance figure is only a qualitative one where each observatory uses its experience to decide if a flare is rather faint (f), normal (n), or rather bright (b).

APPENDIX 2

Optical and White-Light Solar Flare Data with Selected Neutron Events in Chronological Order

Computer Run Start	Computer Run End	Flare No.	Observatory	Date	UT Start	UT End	Lat	Mer Dist	Duration Min	Importance	Remarks	Neutron Events
1 20.206-	2 17.992	1	CULG	2 Jan	0606	0820D	N20	E50	134D	3N	UL	None
27 20.341-	29 6.489	2	MITK	28 Jan	0613E	0654D	S14	W25	41D	2B	--	28 4.138
		3	BOUL	28 Jan	1915	2030	S15	W33	75	2B	--	28 12.056
												28 18.367
												29 0.484
												29 3.656
31 5.257-	32 1.583	4	CANR	31 Jan	1515	1615	S24	W63	60	3B	E	31 7.684
												31 15.919
												31 16.155
41 21.260-	43 15.960	5	KODA	11 Feb	0217E	0315	N19	W03	58D	2B	IK	42 3.794
		6	BULA	11 Feb	0714E	0905	N18	W07	111D	2B	--	43 2.119
		7	CULG	11 Feb	2047	2331	N18	W14	164	2B	LT	43 7.687
		8	TACH	12 Feb	0530E	0615	N20	W19	45D	3N	FIJKZ	
		9	TACH	12 Feb	0746	0830	N20	W20	44	2B	FIJZ	
50 23.683-	51 19.161	10	CATA	20 Feb	0945	1120D	S18	E33	95D	3B	I	None
60 1.861-	60 21.863	11	CULG	1 Mar	0201	0315	S20	W80	74	2B	FRS	60 3.769
		12	CULG	1 Mar	0432	0502	N14	W29	30	2B	LT	
		13	CATA	1 Mar	0935E	1005D	N06	E48	30D	2B	--	
		14	ONDR	1 Mar	1140E	1202D	N18	W37	22D	4N	I	None
		15	CULG	1 Mar	2010E	2129	N16	W37	79D	2B	HRBT	
		16	CULG	1 Mar	2023	2136	N07	E43	73	2B	HRT	

Computer Run Start	Computer Run End	Flare No.	Observatory	Date	UT Start	UT End	Lat	Mer Dist	Duration Min	Importance	Remarks	Neutron Events
65 16.081-	66 13.399	17	CULG	7 Mar	0131	0329	S11	E09	118	3B	HLRSU,PE	None
82 22.035-	83 18.743	18	CANR	24 Mar	0756	0902	N22	W02	66	3B		None
		19	MANI	24 Mar	0918	0931D	N17	W72	13D	2B		
87 14.174-	88 11.820	20	CULG	29 Mar	0031	0233	N14	W37	122	2B	R	None
90 7.893-	91 4.981	21	SANM	31 Mar	1749	1901	S12	E46	72	2B	CIL	90 9.942 90 10.598 90 10.714 90 12.180
96 3.205-	97 0.928	22	SANM	6 Apr	1242E	1518	S13	E27	156D	2B	FI	96 9.912
		23	CULG	6 Apr	2034E	2150	S12	E30	76D	2B	--	96 12.389
104 18.222-	105 15.021	24	KODA	15 Apr	0419E	0519D	N11	W85	60D	2B	CIKX	104 20.788 105 14.152
127 21.249-	128 18.648	25	MANI	8 May	0656	0845D	N11	E22	109D	2B	--	128 11.358 128 17.723
149 16.372-	150 15.416	26	CULG	30 May	0218	0605	S08	W30	227	2B	LR	149 18.522 149 21.754 150 5.711 150 7.381
164 3.687-	167 15.912	27	TEHR	13 Jun	0500E	0555D	N19	E52	55D	2B	K	164 16.327
		28	ONDR	13 Jun	0920E	0940	N16	E51	20D	2B	CFHI	164 18.063
		29	CATA	13 Jun	1335	1420	N14	E43	45	2B	A	164 19.695
		30	ONDR	14 Jun	0503	0643	N18	E43	100	3B	CFHIK	164 6.414
		31	ABST	14 Jun	1321	1406	N24	E42	45	3B	EJ	165 14.631

Computer Run Start	Computer Run End	Flare No.	Observatory	Date	Start	End	Lat	Mer Dist	Duration Min	Importance	Remarks	Neutron Events
164	167 15.912	32	SANM	14 Jun	1417E	1437D	N18	E34	20D	2B	E	166 4.653
		33	SANM	14 Jun	1659	1845	N18	E33	106	2B	UK	166 11.241
		34	TEHR	15 Jun	0749	0820D	N17	W18	31D	2B	Z	166 17.227
		35	CATA	15 Jun	1310	1350	N18	E21	40	2B	--	166 19.052
		36	CATA	15 Jun	1320	1450	N14	E07	90	2B	Z	167 9.203
		37	TEHR	16 Jun	0540	0612D	N18	E14	32D	2B	Z	167 10.408
		38	TEHR	16 Jun	0710	0740D	N17	E12	30D	2B	Z	
		39	MONT	16 Jun	1422E	1452	N16	W34	30D	2B	--	
175	22.015-176 20.109	40	MONT	25 Jun	0759E	1025D	S08	W25	146D	3B	--	176 4.636
		41	MCMA	25 Jun	1834	1940	N09	E13	66	2B	FVY	176 6.473
												176 11.252
												176 13.024
												176 13.226
201	1.519-201 22.947	42	CAPS	20 Jul	1125E	1257	N08	E56	92D	2B	C	201 12.109
												201 18.673
204	8.386-205 5.682	43	BOUL	23 Jul	1823	1950	N10	E08	87	2B	--	None
213	0.751-213 22.295	44	CANR	1 Aug	1045E	1221	N06	W45	96D	2B	--	213 7.815
226	8.134-227 4.808	45	SANM	14 Aug	1548E	1710D	N16	W74	82D	2B	FKT,PE	226 19.756
		46	SANM	14 Aug	1602	1710D	N08	E76	68D	3B	IZ	227 3.327
		47	SANM	14 Aug	1736E	1909D	N16	W77	93D	3B	FI	
296	18.8 -297 15.848	48	CULG	24 Oct	0448	0555D	N19	E75	67D	2B	--	297 1.307
												297 4.522
												297 6.361
301	3.015-302 0.201	49	CAPF	28 Oct	1256E	1425D	N23	E21	89D	3B	HI	301 15.846

Computer Run Start	Computer Run End	Flare No.	Observatory	Date	UT Start	UT End	Lat	Mer Dist	Duration Min	Importance	Remarks	Neutron Events
308 17.185	309 13.116	50	PALE	4 Nov	2119	2330	N24	E16	131	2B	US	309 0.873
		51	MITK	5 Nov	0308	0458D	S12	E37	110D	4B	FHU,PE	
319 5.360	321 19.510	52	CAPS	15 Nov	0744E	0855D	N12	W15	71D	3B	--	319 16.774
		53	LOCK	15 Nov	1750	2000	N16	W18	130	2B	--	320 13.607
		54	CULG	16 Nov	0042	0322	N17	W21	160	3B	V	320 21.862
		55	UCCL	16 Nov	0932E	1109	N17	W27	97D	3N	FI	320 22.921
		56	HUAN	16 Nov	1209	1324D	N17	W29	75D	2B	E	321 5.092
		57	CULG	17 Nov	0121	0209	N15	W33	48	2B	---	321 7.073
		58	CANR	17 Nov	0749E	0940V	N15	W39	111D	2B	--	321 16.498
338 1.070	338 21.743	59	KODA	4 Dec	0938	1146D	N23	E90	128D	3B	AKIRXY	338 7.038 338 8.715 338 19.195 338 19.310
345 12.903	346 11.738	60	CULG	11 Dec	2229E	0201D	N19	E01	212D	3N	LRU,PE	346 3.136 346 6.012 346 7.755
1969												
327 0.064	327 21.394	61	UCCL	23 Nov	1002E	1124D	N13	W19	82D	2B	EIM	327 6.031 327 9.989 327 17.165 327 18.064
1970												
4 11.45	5 7.311	62	BOUL	4 Jan	2125	2145	S18	W72	20	1N	M	None

Day of Year, 1970	Month	Day
2	January	2
28		28
31		31
42	February	11
43		12
51		20
60	March	1
66		7
83		24
88		29
90		31
96	April	6
105		15
128	May	8
150		30
165	June	14
176		25
201	July	20
204		23
213	August	1
226		14
297	October	24
301		28
309	November	5
320		16
338	December	4
346		11

Day of Year, 1969		
327	November	23

APPENDIX 3

Solar Proton Events (Provisional) March 1970

A minor PCA was initially detected about 06/1410 UT as a very gradual phase advance on two Anchorage VLF receivers, the 12.3 kHz Aldra, Norway and 16.0 kHz GBR (Rugby, England) paths. About 1.5 hours later the 20-70 MeV channel on ATS-1 began to respond. Before impending solar eclipse experiments shut down this geostationary satellite at 07/0000Z, fluxes recorded were still about an order of magnitude below that required for measureable riometer absorption on the ground. Twenty-four hours later the sensors were turned on again, at which time fluxes were of the following magnitudes: 5-20 MeV, about 2500 particles/cm^2/sec; 20-70 MeV, about 20 particles/cm^2/sec. Not until 07/1040Z was the PCA event detectable on the Thule 30 MHz riometer. A value shortly before twilight the next day (0947Z) indicated attenuation of the order of 1.5 db. The maximum attenuation reported by Thule was 3 db (08/1645Z); however, a literal interpretation of this absorption is cautioned since the reading may be contaminated by the severe magnetic disturbance in progress at the time. For the 3-day period no riometer data were available from the Alaskan chain due to (1) an REP event beginning 06 March and (2) the great magnetic disturbance of the 7th and 8th. ATS-1 records indicated a maximum for the proton event sometime before 08/0020Z, but exactly how much before is not known. Couting rates returned to very nearly background levels by 09/1800Z.

There exists evidence on the low energy solar cosmic ray channels of Pioneer 6 and 8 that enhanced particle counting rates were being recorded 2 to 8 hours prior to the 08/0020Z quoted above, the times at which ATS-1 data returned. From the known positions of these spacecrafts and the assumption that region 595 was the source we can tentatively conclude that a sector of the interplanetary medium more than 180 degrees in extent was affected.

SOLAR PROTON EVENT (PROVISIONAL) AUGUST 1970

The event below is documented not so much for its magnitude as detected by earth-based sensors but for what its size might well have been had the solar wind geometry been more favorable.

Date/Time	Detector	Activity	Remarks
11/2325UT	SOLRAD-9 1-8A ion-chamber photometer	Class M flare about 20° behind east limb	Class M flares are defined in the following manner: Peak 1-8A flux $\geq 10^{-2}$ ergs/cm^2/sec
12/2020	H_α patrol and SOLRAD-9	Class X flare N12E90 (only top of eruption was observed; classification 1b)	Class X flare defined as peak flux $\geq 10^{-1}$ ergs/cm^2/sec in the 1-8A passband. Importance one loops were observed at 2145UT, spanning at least 10° of arc along the limb. The 1-8A detector was saturated at 0.5 ergs/cm^2/sec for 20 minutes.
2256	Pioneer 6* Simpson solar cosmic ray detector	0.6-13 MeV≃322 counts/sec 13-70 14 70-190 18 $>$ 190 18 (Backgrd ≃ 1 c/s) 0.02 0.04 0.3	Pioneer 6 was detecting protons with energies ~ 1 BeV as the data sample differed from flare onset time by approximately 55 minutes.
1755	Pioneer 7*	≃ 293 10 3 1	

Date/Time	Detector	Activity	Remarks
13/0254 0746 1217 2339	Pioneer 8* (Webber's cosmic ray experiment)	> 13.9 MeV 87 c/s (backgrd 83 ≈ 4 c/s) 154 Above saturation	With enhanced particle counting rates on Pioneers 6, 7 and 8 their relative positions implied an interplanetary disturbance at least 86° in width.
14/0047 0121 0155 0251 0348 0441 0800 1212	Pioneer 8	> 13.9 MeV channel saturated Saturated counting rates 488 c/s 551	
1600	H_α patrol	Class X flare N08E75 (optically an importance 1n)	
1600	Pioneer 8	> 13.9 MeV channel again saturated	
15/0230	ATS-1 geostationary satellite (Aerospace proton and electron spectrometer)	5-21 MeV slightly > 300 particles/cm^2/sec 21-70 MeV about 32 particles/cm^2/sec	First time these particle detectors exceeded the threshold for simultaneous ground-based riometer absorption.
0800	Thule 30 Miz riometer	Registered 1.6 db absorption	
1200	ATS-1	5-21 MeV about 1700 particles/cm^2/sec 21-70 MeV about 85 particles/cm^2/sec	Proton fluxes attained maximum value.
0300	Vela satellite	> 25 MeV about 40 particles/cm^2/sec	Threshold for an event. Data sample inside bow shock.
1800	Thule	1.2 db absorption	

Date/Time	Detector	Activity	Remarks
2133	Pioneer 7	1st energy level ≈ 1080 c/s 2nd 7 3rd 2 4th 2	
2300	Deep River Neutron Monitor	Initial decline begins	
16/0400UT	ATS-1	5-21 MeV ≈ 2000 particles/cm^2/sec 21-70 MeV ≈ 40 particles/cm^2/sec From about 15/0230Z to roughly 16/2000Z proton fluxes in vicinity of earth were at levels sufficient to produce ground-based riometer absorption. In this light the PCA lasted approximately 42 hours. During the period particle fluxes between 5 and 70 MeV displayed a moderate degree of variability.	
2025	Pioneer 7	1st energy level ≈ 1044 c/s 2nd 6 3rd 1 4th 1	
2100	Thule	1.0 db of absorption	
2204	Initial sc,	Approximately 56 γ's	
2220	Secondary sharp increase	H-component about 44 γ's	
17/0200	Deep River	Major decline began	
0330-0900		Most disturbed period of geomagnetic storm. Both Boulder and Fredericksburg recorded 3-hour range indices of 7 during the interval. Duration of major storm was ≈ 57 hours. A_{Fr} for 17 Aug. was 65 for 18 Aug. was 32	
1400	Deep River	Minimum reached on hourly average counting rate (≈ 6% depression)	
18/0000-0500	Deep River	Counting rate approached 6% level several times before beginning recovery.	

*The Pioneer series of space probes are in heliocentric orbits differing little from 1 A.U. in radius. On or about 15 Aug 1970 these spacecraft occupied the following positions with respect to earth:

Pioneer 6 70° behind earth => East limb of sun as seen from earth is 20° east of sun's central meridian as seen from spacecraft.

Pioneer 7 143° behind earth => Spacecraft 53° behind east limb of sun as seen from earth.

Pioneer 8 57° behind earth => East limb of sun as seen from earth 33° east of central meridian as seen from spacecraft.

Pioneer 9 133° ahead of earth.

SOLAR PROTON EVENT (PROVISIONAL) NOVEMBER 1970

	ATS-1 Geostationary Satellite Fluxes			Thule 30 MHz Riometer		Other Sensors	
Nov	UT	5-20 MeV	20-70 MeV	UT	Abs.	UT	
05	0700	Initial detection of enhanced proton fluxes				0700	OGO > 20 MeV flux density equal 20 part/cm^2/sec/ster
	1400	152	16	1400	0.5db		
						1431	OGO > 20 MeV same as above
				1545	0.74		
						1830	4.0 db 23 MHz forward scatter circuit from Barrow to Anchorage
	1900	200	16	1900	0.5		
06	0445	1000	20				
	0620	450	10	Fluxes decreasing steadily			
						1300	2.9 db Paxson averaged about 0.5 during the day
	1530	1400	16				
				1600	0.9	Daytime absorption values ranged from 0.3 to 0.7 db	
	2000	300	8	Both channels alowly decreasing			
	2200	600	8	High energy steady, low energy fluctuating			
07	0000	600	8				
						0046	~ 50 γ Sudden Commencement on Boulder's horizontal component traces (represents about 46 hr transit time)
	0230	1000	10	Low energy enhancement corresponds to arrival of energetic storm particles			
						0400	Korbush decrease began on Deep River Neutron Monitor
	0600	1900	16				
	1100	1900	16				
	1700	1000	7	Fluxes declining			

	ATS-1 Geostationary Satellite Fluxes			Thule 30 MHz Riometer		Other Sensors	
Nov	UT	5-20 MeV	20-70 MeV	UT	Abs.	UT	
						1900	Deep River about 7% depressed
08	0000	300	4				
	2330	5	1				

	Pioneer 6 Particle Fluxes*					Pioneer 8 Particle Fluxes+		
Nov	UT	0.6-13 MeV ≈ 2	13-70 0.2	70-190 0.4	> 190 2	UT	> 13.9 MeV ≈ 7	> 64 MeV 5 (Backgrd fluxes)
05	0425	400	62.8	120	53.0 (First data after flare)			
	0800	240	109	174	21.5			
						0842	94.8	35.2 (First indication of flux enhancement)
						1800	742	
						2100	1210	
	2125	215	45.0	119	14.5			
	2341	216	173	157	19.0			
06	0403	577	188	181	22.9			
						0100	1500	
						0432	404	12.1
	0700	335	83.0	106	30.6			
						0757	598	29.0
	1217	300	183	191	46.8			
	2041	314	44.5	6.88	4.20 (Solar wind speed increased from 383 to 647 km/sec. This discontinuity is believed to be the shock from passage as observed by Pioneer 6. The associated sc was detected on earth 4 hrs later.)			

*At the time Pioneer 6 occupied a position approximately 46° behind earth, placing the spacecraft's east limb 46° behind that as seen from earth.

+Pioneer lagged earth by about 62°.

Alaskan Riometer Chain

Nov	Station	L-Value	Absorption (time)	Max Absorption
05	Shepherd Bay		0.5 db (1900Z)	
	Wildwood	3.75	0.4 (1915Z)	
	Anchorage	4.2	0.3 "	
	Sheep Mt.	4.5	0.9 "	Trace characteristic of noise
	Paxson	5.0	0.1 "	0.8 db at 1615Z
	Ft. Yukon	6.5	0.9 "	1.8 db at 1700Z
	Thule	> 50.	0.4-0.5 (1430-1500Z)	

ACKNOWLEDGEMENTS

I express my deepest appreciation to the following agencies and individuals that contributed to the successful completion of this thesis. NASA/Goddard Space Flight Center provided the necessary funding (Contract NAS5-9275) and Ball Brothers Research Corporation, Boulder, Colorado, provided the engineering and environmental testing for this experiment. The solar geophysical data was compiled by the Aeronomy and Space Data Center, Boulder, Colorado. The Department of Physics and Astronomy at the University of New Mexico, Albuquerque, New Mexico, provided the opportunity for me to undertake this interesting study. The Los Alamos Scientific Laboratory, Los Alamos, New Mexico, allowed me to continue and complete my thesis.

The advice, help, and encouragement of the thesis chairman, Professor C. P. Leavitt of the UNM Department of Physics and Astronomy, proved to be invaluable, as were the extensive comments on solar phenomena made by Professor C. Hyder of NASA-GSFC/UNM. Remarks made by Professor V. Regener of the UNM Department of Physics and Astronomy certainly added substance to the thesis. Dr. Don Robb of the UNM Department of Physics and Astronomy played a key role in the data reduction program. The following individuals of LASL should be mentioned: Don Westerfelt, J-14 Group Leader, C. P. Gutierrez and Jean Davis, EEO, DIR OFF; Judy Elder, P-DOR, and Carol Price, J-14, provided excellent assistance in typing and drafting work, respectively, of the thesis. Also, I would like to extend my compliments to Virginia Roy of the UNM Department of Physics and Astronomy who exhibited great skill in typing the final version of the thesis.

LIST OF REFERENCES

Akimov, W. A., Scintillation Counters in High Energy Physics, Academic Press, New York (1965).

Apparao, M. V. K., Daniel, R. R., and Vijayalakshmi, B., J. Geophys. Res. 71, 1781 (1966).

Arnold, W. R., Phillips, J. A., Sawyer, G. A., Stovell, E. J., and Tuck, J. L., Phys. Rev. 93, 483 (1954).

Bame, S. J., Asbridge, J. R., J. Geophys. Res. 71, 4605 (1966).

Bell, B., Smithsonian Contrib., Astrophys. 5, 69 (1961).

Biermann, von, L., Haxel, O., Schluter, A., Z. Naturforsch. 6a, 47 (1951).

Billings, D. E., A Guide to the Solar Corona, Academic Press, N. Y., (1966) Chapter 8.

Birks, J. B., The Theory and Practice of Scintillation Counting, Pergamon Press, New York (1967).

Boischot, A., Ann. Astrophys. 21, 273 (1958).

Boischot, A., Pick, M., J. Phys. Soc. Japan 17, Suppl. A-II, 203 (1962).

Bothe, W., Becker, H., Z. Physik. 66, 289 (1930).

Bowen, E. J., Mikiewicz, E., Smith, F. W., Proc. Phys. Soc. A62, 26 (1949).

Brini, D., Peli, L., Rimondi, O., Veronesi, P., Nuovo Cimento 11, 655 (1954).

Bohr, N., Phil. Mag. 30, 581 (1915).

Chadwick, J., Nature 129, 312 (1932).

Chadwick, J., Proc. Roy. Soc. (London) A136, 692 (1932).

Chalmers, J. S., Phys. Rev. C 3, 968 (1971).

Conklin, J. C., M.S. Thesis, University of New Mexico (1968).

Cortellessa, P., Di Benedetto, P., Paizis, C., Instituto di Fisica dell' Univerita Report, Milano, Italy (May 1971).

Curie, I., Joliot, F., Compt. Rend. 194, 867 (1932).

Daniel, R. R., Gokhale, G. S., Joseph, G., Lavakare, P. J., Sekhon, B. S., Solar Phys. 10, 465 (1969).

Daniel, R. R., Joseph, G., Lavakare, P. J., Sunderrajan, R., Nature 213, 21 (1967).

Daniel, R. R., Gokhale, G. S. Joseph, G., Lavakare, P. J., J. Geophys. Res. 76, 3152 (1971).

Dubov, E. E., Izv. Krgm. Astrofiz, Observ. 29, 86 (1963).

Ellison, M. A., Conway, M., The Observatory 70, 77 (1950).

Ellison, M. A., McKenna, S. M. P., Reid, J. H., Mon. Not. Roy. Astron. Soc. 124, 263 (1962).

Ellison, M. A., Q. J. Roy. Astron. Soc. 4, 62 (1963).

Fano, U., Ann. Rev. Nucl. Sci. 13, 1 (1963).

Farley, T. A., Tomassian, A. O., Phys. Rev. Letters 25, No. 1 (1970).

Fireman, E. L., DeFelice, J., Tilles, D., Phys. Rev. 123(6), 1935 (1961).

Fokker, A. O., Bull. Astron. Inst. Neth. 16, 311 (1962).

Forrest, D. J., Chupp, E. L., Solar Phys. 6, 339 (1969).

Friedman, H., Space Astrophysics, McGraw Hill, New York (1961), p. 107.

Gamow, G., Teller, E., Phys. Rev. 53, 608 (1938).

Garwin, R. L., Rev. Sci. Instr. 23, 755 (1952).

Gibson, W. A., Rev. Sci. Instr. 35, 8 (1964).

Gillette, R. H., Rev. Sci. Instr. 21, 294 (1950).

Goldberg, L., Mohler, D. C., Muller, E. A., Astrophys. J. 127(2), 302 (1958).

Gooding, T. J., Eisberg, R. M., Phys. Rev. 105, 357 (1957).

Gooding, T. J., Pugh, H. G., Nucl. Instr. Meth. 17, 189 (1960).

Gordon, I. M., Dohl. Acad. Nauk. SSSR 94, 813 (1954).

Hackenberg, O., Kruger, A., J. Atmos. Terr. Phys. 17, 20 (1959).

Heidbreder, E., Pinkau, K., Reppin, C., Schonfelder, V., J. Geophys. Res. 75, 6347 (1970).

Hess, W. N., NASA TN D-1696 (1963).

van de Hulst, H. C., The Sun, University of Chicago Press, Chicago (1953) p. 211.

de Jager, C. (Ed), The Solar Spectrum, D. Reidel Publ. Co., Dordrecht (1965).

Janni, J. F., AFWL-TR-65-150, Air Force Weapons Lab., Kirtland AFB, New Mexico (1966).

Kiepenheuer, K. O., The Solar Spectrum (Ed. by C. de Jager), D. Reidel Publ. Co., Dordrecht (1965) p. 240.

Kim, C. Y., Canadian J. Phys. 46, S753 (1968).

Kundu, M. R., Smerd, S. F., Info. Bull. Solar Radio Observ., No. 11 (1962).

Kundu, M. R., J. Phys. Soc. Japan 17, Suppl. A-II, 259 (1962).

Landau, L., J. Phys. USSR 8, 201 (1944).

Lingenfelter, R. E., Flamm, E. J., Canfield, E. H., Kellman, S., J. Geophys. Res. 70, 4077 (1965).

Lingenfelter, R. E., Flamm, E. J., Canfield, E. H., Kellman, S., J. Geophys. Res. 70, 4087 (1965).

Lingenfelter, R. E., Ramaty, R., High Energy Nuclear Reactions in Astrophysics, W. A. Benjamin, Inc., New York (1967).

Lingenfelter, R. E., Solar Phys. 8, 341 (1969).

Leavitt, C. P., private communication.

Martheray, M., L'Astronomie 36, 276 (1922).

Maxwell, A., Thompson, A. R., Astrophys. J. 135, 138 (1962).

McCracken, K. G., Nuovo Cimento X, 13, 1081 (1959).

McCracken, K. G., Palmeira, R. A. R., J. Geophys. Res. 65, 2673 (1960).

McLean, D. J., Sheridan, K. V., Stewart, R. T., Wild, J. P., Nature 234, 140 (1971).

Measday, D. F., Richard-Serre, C., CERN 69-17 (1969).

Mustel, E. R., Isv. Krymsk. Astrofiz. Observ. 15, 54 (1955).

NASA, X-440-66-494, Goddard Space Flight Center, Greenbelt, Md. (1966).

Ortner, J., Maseland, H. (Eds.), Introduction to Solar Terrestrial Relations, D. Reidel Publ. Co., Dordrecht (1965).

Parker, E. N., Phys. Rev. 107, 830 (1957).

Pearson, R. J., Waitz, E. K., High Energy Neutron Detector Experiment Report, Ball Brothers Research Corp., Boulder, Colorado (1969).

Place, James R., Ph.D. Dissertation, University of New Mexico (1972).

Ro, P. S., Ph.D. Dissertation, University of New Mexico (1971).

Roelof, E. C., J. Geophys. Research 71, 1305 (1966).

Rosebury, F., Handbook of Electron Tubes and Vacuum Techniques, Addison-Wesley Publ. Co., Massachusetts (1965).

Rossi, B., High Energy Particles, Prentice-Hall, New Jersey (1965).

Rossi, B., Olbert, S., Introduction to the Physics of Space, McGraw Hill, New York (1970).

Schrcliff, W. A., Jones, R. C., J. Opt. Soc. Am. 39, 912 (1948).

Seltzer, S. M., Berger, M. J., NAS-NRC Publ. No. 1133 (1965) p. 187.

Severny, A. B., Izv. Crimean Astrophys. Observ. 20, 22 (1958).

Severnyi, A. B., Izv. Krymsk. Astrofiz. Observ. 16, 12 (1956).

Siegel, R. T., Handbuch der Physik (Ed. S. Flugge), Vol. 45, J. Springer, Berlin (1958).

Simnett, G. M., Holt, S. S., Solar Phys. 16, 208 (1971).

Skyrme, D. J., Nucl. Instr. Meth. 57, 61 (1967).

Smith, H. J., Smith, E. V. P., Solar Flares, Macmillan Co., New York (1963).

Smith-Rose, R. L. (Ed.), Space Research VI, Spartan Books, Washington, D. C. (1966).

Sobolev, V., Radiative Energy Transport in Planetary and Stellar Atmospheres, Moscow (1956).

Sosnovskii, A. N., Spivak, P. E., Prokopiev, Y. A., Kutkov, I. E., Dobrinin, Y. V., Nucl. Phys. 10, 395 (1959).

Stein, W. A., Ney, E. P., J. Geophys. Res. 68, 1605 (1963).

Stepanyan, A. A., Izv. Krymsk. Astrofiz. Observ. 27, 178 (1962).

Storm, E., Israel, H. I., Nucl. Data Tables A7, 565 (1970).

Svestka, Z., Solar Phys. 13, 471 (1970).

Svestka, Z., Solar Phys. 19, 202 (1971).

Sydor, M., Ph.D. Dissertation, University of New Mexico (1964).

Symon, K. R., Ph.D. Dissertation, Harvard University (1948).

Takakura, T., Kai, K., Publs. Astron. Soc. Japan 13, 94 (1961).

Tanberg-Hansen, E., Solar Activity, Blaisdell Publ. Co., Massachusetts (1967).

Trouvelot, E. L., L'Astronomie 10, 287 (1891).

Uchida, Y., J. Phys. Soc. Japan 17, Suppl. A-II, 234 (1962).

Van Zyl, C. P., Voss, R. G. P., Wilson, R., Phil. Mag. 1, 1003 (1956).

Vavilov, P. W., Sov. Phys. JETP 5, 749 (1957).

Vernov, S. N., Gorchakov, E. V., Shavrin, P. I., Sharvina, K. N., Space Sci. Rev. 7, 490 (1967).

Warwick, C. S. Astrophys. J. 121, 385 (1955).

Webber, W. R., Ormes, J. F., J. Geophys. Res. 72, 3387 (1967).

Wild, J. P., J. Phys. Soc. Japan 17, Suppl. A-II, 249 (1962).

Wolcott, J. H., Ph.D. Dissertation, University of New Mexico (1968).

Wright, G. T., Phys. Rev. 91, 1283 (1953).

Xanthakis, J. N. (Ed.), Solar Physics, Interscience Publ., New York, (1967).

Zanstra, H., Circ. Astron, Inst. Univ. Amsterdam, No. 1 (1950).

Zirin, H., The Solar Atmosphere, Blaisdell Publ. Co., Massachusetts (1966).

Zych, A. D., Frye, G. M., Jr., J. Geophys. Res. 74, 3726 (1969).